UNIVERSITÄT
DUISBURG
ESSEN

Open-Minded

Department of Chemistry

Nonlinear Molecular Spectroscopy on Aromatic Chromophores with Homo- and Heterodyne Detection

Dissertation

to obtain the degree
Dr. rer. nat.

by

Till Reichenauer
born in Duisburg

Essen, April 2024

DOI: 10.17185/duepublico/82107
URN: urn:nbn:de:hbz:465-20240628-074227-3

Eidesstattliche Erklärung

Hiermit versichere ich, dass die vorliegende Arbeit über "Nonlinear Molecular Spectroscopy on Aromatic Chromophores with Homo- and Heterodyne Detection" selbstständig verfasst worden ist, dass keine anderen Quellen und Hilfsmittel als die angegebenen benutzt worden sind und dass die Stellen der Arbeit, die anderen Werken – auch elektronischen Medien – dem Wortlaut oder Sinn nach entnommen wurden, auf jeden Fall unter Angabe der Quelle als Entlehnung kenntlich gemacht worden sind.

Des Weiteren versichere ich, dass die vorliegende Dissertation ausschließlich im Rahmen dieses Promotionsverfahrens eingereicht wurde.

Ich erkläre mich auch mit einem Abgleich der Arbeit mit anderen Texten zwecks Auffindung von Übereinstimmungen sowie mit einer zu diesem Zweck vorzunehmenden Speicherung der Arbeit in einer Datenbank einverstanden.

Essen, April 2024

Till Reichenauer

Gutachter

Prof. Dr. Sebastian Schlücker

Prof. Dr. Eckhardt Hasselbrink

Vorsitzende

Jun.-Prof. Dr. Anzhela Galstyan

Datum der Disputation: 18.06.2024

Abstract

In this thesis, three nonlinear optical techniques are utilized to spectroscopically explore the electronic and vibrational states of aromatic molecules, specifically arylazopyrazole, anthracene, and MOM-BINOL.

In the first section femtosecond transient absorption spectroscopy was employed to investigate the photoisomerization dynamics of planar and non-planar arylazopyrazole (AAP) molecular photoswitches. This revealed that the twisted configuration accelerates photoisomerization due to the pre-existing out-of-plane rotation of the phenyl and pyrazole rings, causing their π-systems to be out of conjugation with the p-orbitals of the azo groups.[1] Moreover, the study underscores the significance of ground state ring vibrations in this flexible system, which influences the range of Franck-Condon states available in an ensemble and consequently affects the observed relaxation process.

Subsequently the electronic-vibrational interactions in the rigid molecule anthracene is studied using resonance Raman spectroscopy over its first excited state ^1L_a using the Kerr-gate fluorescence suppression technique. Although most peaks in the Raman excitation profile align with the absorption maximum of the $^1L_a(0-0)$ resonance at 376 nm, a notable exception is observed for the Raman peak detected at 785 cm^{-1}. This Raman peak exhibits a Raman excitation profile that diverges significantly from the anthracene absorption spectrum, peaking instead at 370 nm, which corresponds to a minor shoulder in the absorption spectrum. This discrepancy suggests a nearly exclusive Raman enhancement by the dark state ^1L_b for the corresponding vibrational mode.

Lastly, a novel nonlinear chirally sensitive method known as CARS-ROA is reproduced and the challenges associated with this highly sensitive experiment are detailed in the final section. Following this, a dissolved chiral substance (MOM-BINOL) is examined.

Kurzzusammenfassung

In dieser Arbeit werden drei nichtlineare optische Techniken verwendet, um die elektronischen und vibrationellen Zustände aromatischer Moleküle spektroskopisch zu untersuchen, insbesondere Arylazopyrazol, Anthracen und MOM-BINOL.

Im ersten Abschnitt wurde die femtosekundenzeitaufgelöste Absorptionsspektroskopie verwendet, um die Photoisomerisierungsdynamik von planaren und nicht-planaren Arylazopyrazol-Molekülschaltern (AAPs) zu analysieren. Dabei wurde festgestellt, dass die verdrehte Konfiguration im elektronischen Grundzustand die Photoisomerisierung beschleunigt. Dies wurde dadurch erklärt, dass in der verdrehten Anfangsgeometrie die π-Systeme nicht mehr mit den p-Orbitalen der Azogruppen konjugiert sind. Darüber wird die Bedeutung der Drehschwingungen im Grundzustand in diesem flexiblen System hervorgehoben, die die möglichen verfügbaren Franck-Condon-Zustände beeinflussen und dadurch folglich den beobachteten Relaxationsprozess beeinflussen.

Anschließend werden die elektronisch-vibrationalen Wechselwirkungen im starren Molekül Anthracen über seinen ersten angeregten Zustand an der Absorptionsbande ^1L_a unter Verwendung der Resonanz-Raman-Spektroskopie untersucht, wobei die Kerr-Schalter-Fluoreszenzunterdrückungstechnik angewendet wird. In diesem Abschnitt wurden interessante Beobachtungen gemacht, wobei eine Raman-Bande bei 785 cm^{-1}, die möglicherweise eine Atemschwingung darstellt, ein stark abweichendes Raman-Anregungs-intensitätsprofil aufweist, das bei 370 nm ein Maximum durchläuft. Dieses Phänomen könnte auf einen Übergang vom Grundzustand zum dunklen elektronischen Zustand ^1L_b zurückzuführen sein.

Zuletzt wird eine neuartige nichtlineare, chiralsensitive Methode namens CARS-ROA reproduziert und die mit diesem sensiblen Experiment verbundenen Herausforderungen werden im abschließenden Abschnitt dargestellt. Anschließend wird hiermit eine chirale Substanz in Lösung (MOM-BINOL) untersucht.

Contents

Motivation

Molecules known as photoswitches possess the capacity to alter their configuration upon exposure to light, leading to changes in chemical characteristics such as molecular size and solubility. As our eyes cannot utilize semiconductor-based optoelectronics to detect light, nature has implemented a molecular photoswitch. In this process, the molecular photoswitch rhodopsin is linked to a protein known as GPCR in the human eye.[2] Upon light absorption, rhodopsin undergoes Z to E isomerization, which initiates events that lead to light perception.

In modern chemistry, synthetic photoswitches can be produced, enabling applications in particular for photopharmacology.[3] In 2014, Fuchter and co-workers introduced a new class of photoswitches, the dimethyl-arylazopyrazoles (AAPs).[4] Unlike the aforementioned rhodopsin, these molecules can switch permanently between two geometries and achieve very high yields in transitioning from one isomer to the other via irradiation. In 2016, Ravoo and colleagues expanded on the work from Fuchter and co-workers by introducing a variety of AAP photoswitches with added TEG substitutions, making these molecules water-soluble which is crucial for biological applications.[5, 6] These molecules have displayed significant promise for host-guest chemistry, which could be significant in the field of photopharmacology.[6]

One type of arylazopyrazole with two additional methyl substitutions exhibited a twisted geometry. Interestingly, such a geometry exists also in an azobenzene (bridged azobenzene) which possesses exceptional ultrafast dynamics.[7] Determining the dynamics of arylazopyrazole photoswitches by the use of ultrafast optical spectroscopic techniques like transient absorption is essential for corroborating results from molecular dynamics simulations. Such simulations have the potential to predict enhanced properties of AAPs by further substitutions.

In contrast to the photoswitch arylazopyrazole, the polycyclic aromatic compound anthracene lacks any ultrafast twisting reaction. Its structure remains completely planar, and the relaxation dynamics from its excited states are primarily governed by slower vibrational relaxation.[8] This molecule exhibits remarkable rigidity and high symmetry

(D_{2h} point group). Anthracene and naphthalene are the simplest polycyclic aromatic hydrocarbons and serve as important benchmark molecular systems for understanding the photophysics of polycyclic aromatic compounds. With 12 π-electrons, anthracene exhibits extensive electron delocalization, resulting in its first excited state being positioned close to the visible spectral range (ca. 375 nm). However, despite the wealth of knowledge on most properties of anthracene, resonance Raman scattering, a process wherein the mixing of electronic and vibrational wavefunctions (vibronic coupling) holds special importance, has only been explored incompletely.

Interestingly, the first excited state of anthracene, known as the ^1L_a (Platt notation) or S_1 state, would be invisible in absorption were it not for vibronic coupling (pseudo-forbidden).[9] Moreover, this pseudo-forbidden state is anticipated to be adjacent to a nearly degenerate additional excited state (^1L_b or S_2) which is considered to have a negligible contribution to the absorption spectrum even when compared to the weakly absorbing ^1L_a state. Since transitions in resonance Raman spectroscopy are not bound by the same selection rules as single-photon absorption, there is a possibility of observing effects from this state through resonance Raman scattering. Despite this possibility, conducting resonance Raman spectroscopy on the first excited state of anthracene, ^1L_a (or S_1) hasn't been pursued yet, likely due to the significant co-propagating fluorescence background coupled with a very low transition strength. However, modern pulsed laser techniques offer a solution to isolate the Raman signal from a substantial fluorescence background through the implementation of a Kerr-gate. In this thesis, this methodology is employed to uncover the resonance Raman excitation profiles at the ^1L_a state on the first vibronic transition (0-0).

Contrary to the highly symmetric anthracene, many molecules in biology are asymmetric through a property known as chirality.[10] For chiral molecules two isomers known as enantiomers exist which cannot be superimposed onto their mirror images. The primary reason for researching and identifying chiral structures is the field of biology. Biologically relevant molecules, such as amino acids, proteins, carbohydrates, and nucleic acids, exist in one entianomer and the biological activity of molecules often also strongly depends on their chirality. Therefore, understanding the chiral properties of molecules is valuable for synthesizing new drugs and comprehending biochemical processes.

Two of the earliest and simplest methods used to study chirality are electronic circular dichroism (ECD) and optical rotational dispersion (ORD). These phenomena can be linked to non-chiral absorption and refraction, as they probe electronic properties, resulting in relatively strong signals. ECD can even be conducted in ultrafast time-resolved experiments.[11] However, these methods yield signals that are not very unique to each

chiral molecule since the electronic resonances are generally broad in part due to vibronic fine structure.[12]

Raman spectroscopy, which probes vibrational properties, also has a chiral equivalent known as Raman Optical Activity (ROA). This method provides both the vibrational structure of a material and its chirality, allowing, for example, the spectroscopic analysis of a mixture of chiral compounds.

In ROA, the inherent low intensity of the Raman signal is further diminished by the naturally faint circular dichroism signal, which is typically $10^{-3} - 10^{-4}$ of the achiral Raman intensity.[13] This usually requires extended acquisition periods (hours to days). In consequence, conducting time-resolved ROA measurements, such as studying structural changes during rapid chiral chemical reactions, are challenging.[14, 15] One way to enhance spontaneous Raman signals by up to three orders of magnitude is through nonlinear Raman techniques with a Stokes excitation field such as CARS, making these methods particularly appealing for ROA detection.

In the early 1980s, Bjanarson *et al.* and Oudar *et al.* laid the theoretical groundwork for two potential nonlinear ROA methods: Chiral coherent anti-Stokes Raman spectroscopy (CARS-ROA) and chiral Raman-induced Kerr effect spectroscopy (RIKE-ROA).[16, 17]

One of the key advantages of CARS-ROA and RIKE-ROA is the requirement for only linearly polarized light to capture a signal similar to conventional ROA. Moreover, measuring ROA using CARS offers resistance to fluorescence interference, thereby potentially enabling the exploitation of the resonance Raman effect to further bolster the signal and target particular sample components. However, despite the anticipated higher absolute CARS-ROA signal compared to conventional ROA, the contrast between chiral and achiral signals is expected to be lower at 10^{-6} compared to 10^{-3} for normal ROA unless heterodyne detection is employed.[17]

Thirty years later, in 2012, Hamaguchi *et al.* were the first to successfully implement the heterodyne CARS-ROA technique suggested by Oudar *et al.*. However, until now, only a few such measurements have been done. On the other hand, CARS-ROA for diluted or dissolved samples has not been tested. For this reason, in addition to replications of Hamaguchi *et al.*'s measurements of β-pinene, some measurements of diluted chiral samples are shown in this thesis.

Chapter 1

Theoretical Background

1.1 Transient Absorption Spectroscopy

Transient absorption (TA) spectroscopy or pump-probe spectroscopy is used to monitor excited state population relaxation using two short and time-delayed photoexcitation pulses. The basic scheme is shown in Fig. 1.1. The measurement is initiated with a resonant pump pulse which elevates some molecules in the sample from the ground state to an excited electronic state via absorption. Following a time delay of Δt, a probe pulse—be it a spectrally narrow pulse, such as used in narrowband transient absorption, or a broadband white light pulse for broadband transient absorption—interrogates the photoexcited sample. The transient absorption signal is detected along the probe pulse direction. The resulting signal change by scanning the time delay Δt can be used to observe the relaxation dynamics of a variety of photophysical and photochemical processes induced by the pump.[18]

From the perspective of classical electrodynamics, the transient absorption signal in isotropic samples is derived from the third-order susceptibility. Despite being a third-order nonlinear experiment, TA can be understood intuitively as time-dependent linear

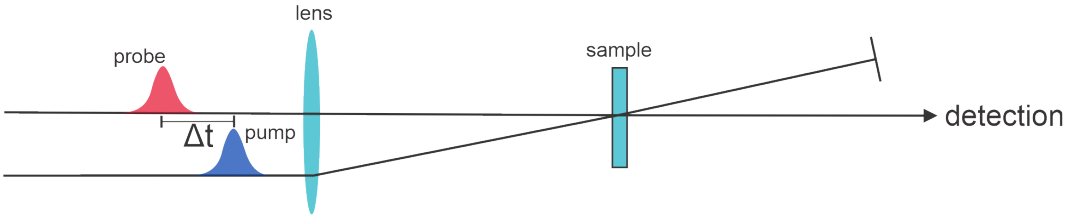

Figure 1.1: Experimental scheme of transient absorption. The pump and probe pulses are synchronized and directed onto a sample with a temporal delay Δt. The signal of the probe pulse is then detected.

absorption, the explanation for this will be outlined in the following.

With the assumption that the sample is isotropic, the generated third-order signal measured at the detector must satisfy the following combination of wave vectors:

$$\overrightarrow{k_{signal}} = \overrightarrow{k_{pump}} - \overrightarrow{k_{pump}} + \overrightarrow{k_{probe}} \Rightarrow \overrightarrow{k_{signal}} = \overrightarrow{k_{probe}}. \tag{1.1}$$

The pump pulse therefore acts on the sample twice at time-zero ($\Delta t = 0$) with opposite momentum and the signal is collinear with the probe. The fact that the measured signal follows the direction of the probe pulse appears disadvantageous at first since the probe field can overwhelm the signal field during detection. This problem could in principle be avoided by providing the two pump interactions from different directions (for example using a folded-boxcars geometry) which would impart a unique direction to the signal, enabling background-free detection. The latter experiment is called transient grating and has some unique advantages over TA.[19] However, the TA experiment actually provides a stronger signal. This is because the strong probe field also acts as an amplifying local oscillator (LO). This measurement approach is referred to as homodyne detection and arises because detectors measure intensity rather than individual electric field components.[20] The electric fields along the probe direction in TA result from three main contributions: the probe field E_{pr}, the linear absorption signal $E^{(1)}$ and the pump-probe signal $E^{(3)}$. Consequently, the intensity measured by the detector can be described as:[21]

$$\begin{aligned} I_{probe} &\sim \left|E_{pr} + E^{(1)} + E^{(3)}(\omega_{pr}, \omega_{pu}, \Delta t)\right|^2 \\ &= \left|E_{pr} + E^{(1)}\right|^2 + \left|E^{(3)}(\omega_{pr}, \omega_{pu}, \Delta t)\right|^2 + 2Re(E^*_{pr} + E^{*(1)})E^{(3)}(\omega_{pr}, \omega_{pu}, \Delta t) \\ &\approx I_0 + 2Re(i\omega N E^*_{pr}\chi^{(3)}(\omega_{pr}, \omega_{pu}, \Delta t)E^2_{pu}E_{pr} = I_0 + 2Re(i\omega N\chi^{(3)}(\omega_{pr}, \omega_{pu}, \Delta t)I_{pu}I_{pr}) \\ &= I_0 + 2\omega N I_{pu}I_{pr}Im(\chi^{(3)}(\omega_{pr}, \omega_{pu}, \Delta t)). \end{aligned} \tag{1.2}$$

Here the term $\left|E^{(3)}\right|^2$ is neglected since $(\chi^{(3)})^2$ is small. I_0 is the signal without the pump pulse affected by linear absorption ($I_0 \sim \left|E_{pr} + E^{(1)}\right|^2$). From the above relation, some key aspects of pump-probe spectroscopy are revealed. Firstly, in the TA detection scheme, the time-dependent signal is directly proportional to the imaginary part of $\chi^{(3)}$ which is analogous to linear absorption. Additionally, the measured signal is linearized to the pump intensity. Furthermore, similar to linear absorption, the signal exhibits a linearized dependence on the density of molecules N (instead of N^2). Theoretically deriving $Im(\chi^{(3)})$ for a single molecule or an ensemble of molecules can be done quantum mechanically.[20]

To obtain the time-dependent pump-probe signal, I_0 must be subtracted (or divided) which can be done by a second reference measurement where the pump beam is blocked. Since I_0 is significantly larger than the actual pump-probe signal, typically a modulation transfer scheme is employed to improve the signal-to-noise ratio. In this scheme modulation from the pump beam transfers to the probe by placing a chopper in the pump beam path. In this manner, in combination with lock-in detection, the modulated TA signal $\Delta I = I - I_0$ can be directly measured. By dividing this signal with I_0 the pump-probe signal is made independent of the probe intensity.

To account for the Beer-Lambert law of absorption whereby transmission decreases exponentially with increased concentration, the transient absorption signal is usually given as the differential absorbance signal $\frac{\Delta A}{A_0}$ in OD by taking the decadic logarithm.

$$\frac{\Delta I}{I_0} \sim Im(\chi^{(3)}(\omega_{pr}, \omega_{pu}, \Delta t)) \tag{1.3}$$

$$\rightarrow \frac{\Delta A}{A_0} = -log_{10}\left(\frac{\Delta I}{I_0}\right). \tag{1.4}$$

Alternatively, for broadband pump-probe spectroscopy, a fast detector array, can simultaneously measure the transient signal over many probe frequencies yielding a pump-probe spectrum. For a detector array, the two probe spectra one where the pump is unblocked by the chopper and the other where the pump is blocked are divided and subtracted by unity.

$$\frac{\Delta I}{I_0} = \frac{I}{I_0} - 1. \tag{1.5}$$

In the majority of pump-probe experiments, when Δt is scanned, relaxation observed is from population relaxation (longitudinal relaxation) from the excited state to the ground state.[20] The most rapid form of relaxation processes occurs via non-radiative pathways. An important intra-molecular non-radiative process occurs when a molecule transitions from a higher vibronic level to a lower energy vibrational mode. Conformational changes represent another type of intra-molecular relaxation process that can occur rapidly and will be the main mechanism observed in this thesis. Lastly, the molecule can relax by transferring energy to the surrounding solvent.[20]

Another source of decay in transient absorption, apart from population relaxation, can originate from dephasing (transverse relaxation) due to collisions with solvent molecules. Oftentimes dephasing happens rapidly in comparison to the pump pulse length, the tran-

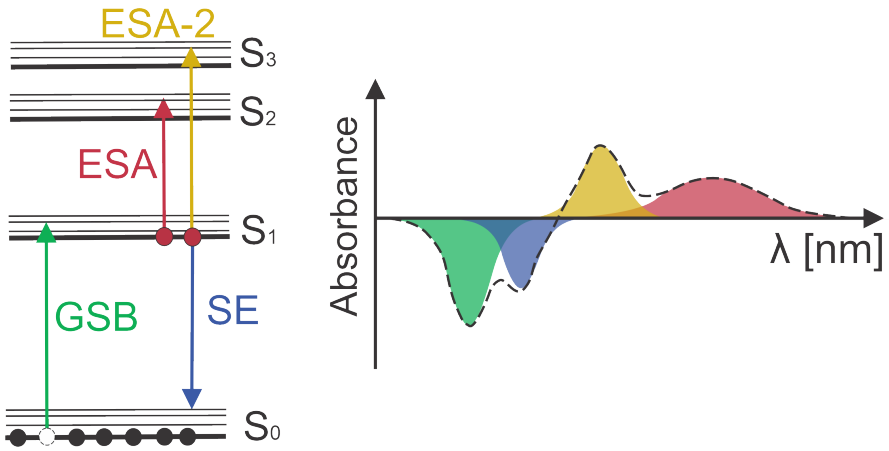

Figure 1.2: Left: Ladder diagram illustrating the three classes of signals in pump-probe spectroscopy. Each bold line corresponds to the lowest vibronic state of the molecule, while the smaller lines depict higher vibrational states. Right: Illustration of a transient absorption (TA) spectrum, with each component represented by a Lorentzian curve, with the same color coding as seen on the left. The dashed line shows the resulting TA spectrum. The order of each component in wavelength is molecule-specific.

sient absorption experiment can then be considered incoherent, and the relaxation measured is mainly due to population relaxation.

In a molecular system, there are three main processes by which the excited state population relaxation can be measured. These are shown for a system with four electronic levels, including their vibrational levels, in the left part of Fig. 1.2. Ground state bleach (GSB) and stimulated emission (SE) are processes that involve only two states, whereas excited state absorption (ESA) requires a third energy level.

Ground state bleach manifests as an increase in transmission (or a decrease in absorbance) and occurs at the same frequencies as ground state absorption. GSB arises from a lower ground state density due to some molecules being raised into a higher excited state by the pump. Stimulated emission between the excited and ground states also produces a negative absorbance signal due to the newly generated photons. Stimulated emission is often seen at lower photon energies compared to GSB since the transition can occur into the higher vibronic states of the ground state.

The last process, excited state absorption, occurs due to a second absorption event from the excited state population to an even higher state. This process represents a positive signal in absorbance since the probe light is absorbed. On the right side of Fig. 1.2, an example of a transient absorption spectrum is displayed. It's notable that the three TA components typically overlap, leading to sharp turning points in the pump-probe spectrum.

The following section will explore a specific use of transient absorption in the context of photophysical reactions found in molecular photoswitches.

1.1.1 Molecular Photoswitches and Arylazopyrazoles

Molecular photoswitches are molecules which possess at least two ground states as potential well minima on their ground state potential energy surface corresponding to distinct isomers. These isomers can be distinct geometrical arrangements and/or atomic redistributions within the molecule.[22] In the ground state, these minima are separated by a substantial energy barrier, rendering one state stable and the other meta-stable. The stability of the meta-stable state is typically given as a half life time $t_{1/2}$ at room temperature.

Light irradiation can initiate a transition between these states (photoisomerization). Upon absorption of light, photochromic molecules transition instantly from the ground to an excited electronic state in what is known as the Franck-Condon state where the geometry of atoms remains unchanged since an electronic transition is much faster than any rearrangement of atoms. Subsequently the molecule relaxes by conformational changes along a primary reaction coordinate leading to a decrease in energy. It's worth noting that an alternative direct relaxation pathway from the excited state back to the ground state is through spontaneous fluorescence, although its significance becomes less important if the relaxation proceeds on the order of femto to picoseconds.[23]

As the molecule relaxes on the excited state potential energy surface, it typically reaches an intermediate configuration where the electronic excited state and the ground state become closest. Two fundamental scenarios can occur, which are depicted in Figure 1.3.[24]

One scenario involves an avoided crossing, where there is no intersection between the two electronic potential surfaces. Here, the molecule can bridge this energy gap through internal conversion facilitated by vibronic coupling. The larger the energy gap, the longer this relaxation process will take, often spanning from picoseconds to microseconds.[24, 25]

A different fundamental scenario occurs when the two electronic state surfaces intersect: this is called a conical intersection (or crossing seam if additional reaction coordinates are considered). Here the transition rate back to the ground state is typically ultrafast, often occurring within a few picoseconds or less. Azobenzene (AB) is a prime example for a simple photochromic molecular switch with two ground states and a conical intersection. It remains the most applied photoswitch used to date in photopharmacology and consists of two phenyl rings connected by an azo-bridge.[3] The two isomers of AB are depicted in

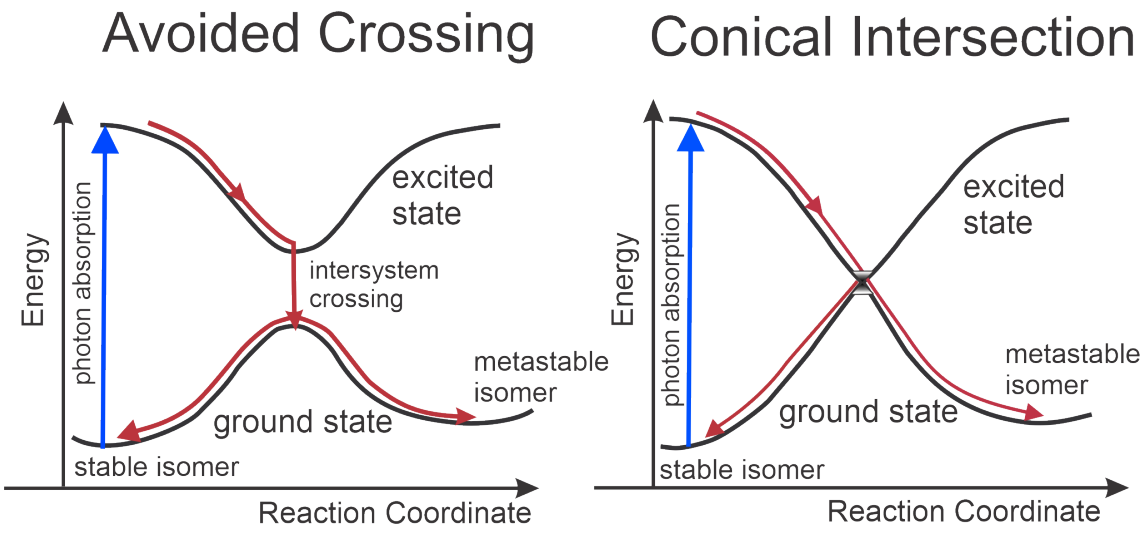

Figure 1.3: Two basic scenarios in which the ground and excited state potential energy surfaces meet in a photoswitch molecule. On the left, an avoided crossing scenario is depicted, where the potential surfaces approach closely but do not touch. On the right is shown a conical intersection, here the two surfaces intersect. The blue arrow indicates the transition of the molecule from the ground state to the excited state upon photon absorption. The red line illustrates the subsequent reaction paths of the molecule leading to either the stable or metastable isomer geometry.

the top part of Fig. 1.4. The stable isomer of azobenzene is the E isomer for which the two phenyl rings are planar with the azo bridge. In contrast the metastable Z-isomer is rotated by 180° for the dihedral angle of the azobridge (CNNC).

In the UV-visible range AB experiences photoisomerization via two distinct transitions.[27] One involves the excitation of electrons in the π-orbital of the azo group, resulting in a π to π^* transition ($\pi\pi^*$) (see bottom part of Fig. 1.4). The other entails the excitation of non-bonding, lone pair electrons in the nitrogen atoms, leading to a $n\pi^*$ transition. These transitions generate an excited state with an anti-bonding character in the azo group, thus freeing the nitrogen double bond and enabling rotation of the molecule and allowing photoisomerization to the other isomer. The E-isomer has a larger $\pi\pi^*$ transition oscillator strength whereas the Z-isomer has a larger $n\pi^*$ transition oscillator strength. The larger E-isomer $\pi\pi^*$ transition is caused by the conjugation of the phenyl rings with the azo bridge. The weak $n\pi^*$ transition of the E-isomer is due to a mirror plane at the azo bridge making the transition symmetry forbidden for the E-isomer.

In contrast the Z-isomer does allow the $n\pi^*$ transition because the phenyl ring dihedral angles to the azo-bridge (CCNN and NNCC) are rotated by ∼56°.[28]

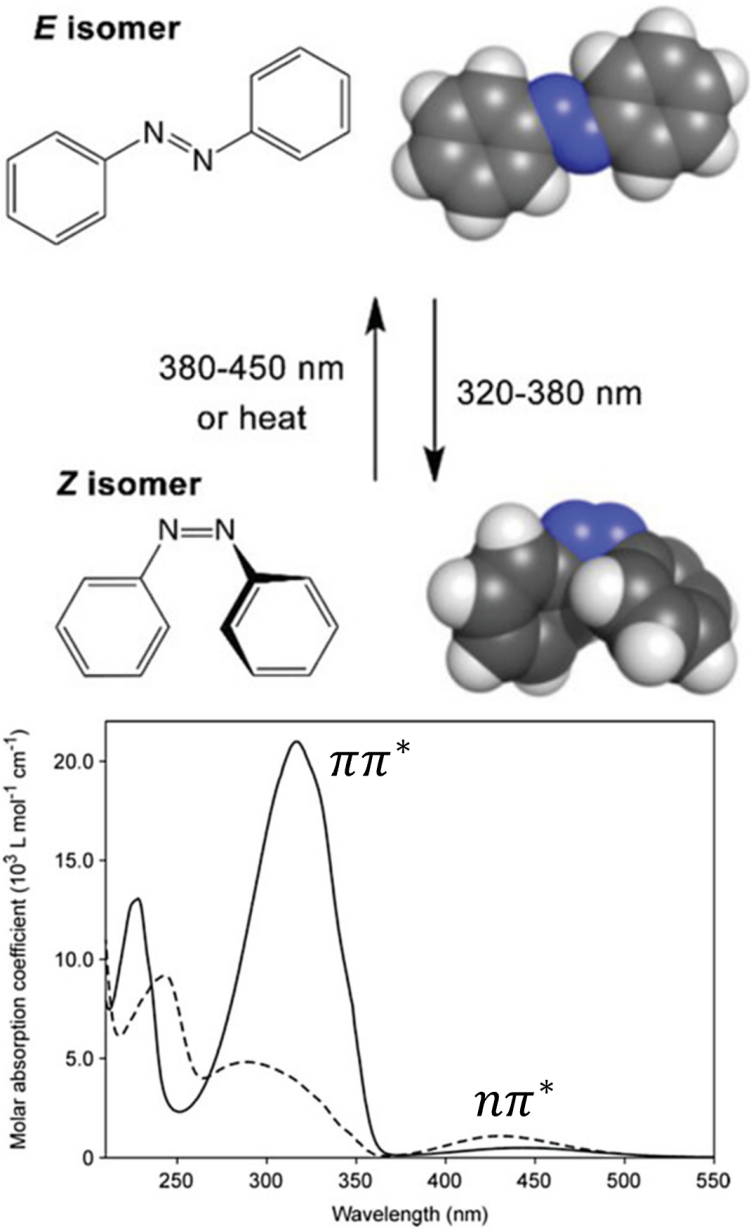

Figure 1.4: The two isomers of the azobenzene molecular photoswitch are represented by their skeletal and space-filling models in the top. The absorption spectrum of AB is depicted at the bottom (modified and reprinted with permission from [26]).

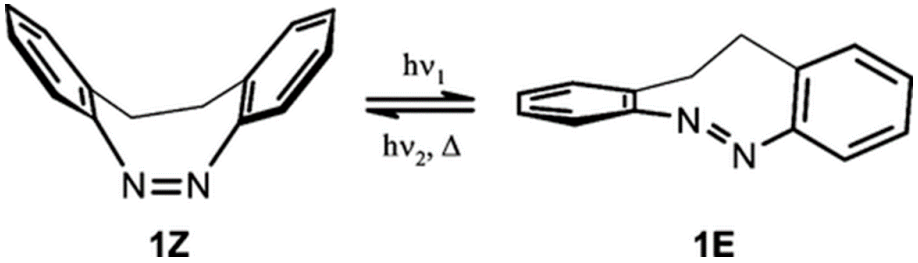

Figure 1.5: The two isomers of bridged azobenzene. This photoswitch displays a nearly 100% quantum yield in $E \rightarrow Z$ direction. In bridged AB, thermal relaxation is directed towards the Z-isomer, rather than the E-isomer (reprinted with permission from [7]).

The contrast in transition strengths and resulting differences in absorption spectra between the two AB isomers enable reversible photoswitching for this molecule. This crucial characteristic which to a great extent determines the usefulness of a two-way molecular photoswitch, is quantitatively characterized by its photostationary state (PSS). The PSS is defined at two wavelengths: one for forward switching and one for backswitching. The ideal PSS will be 100% in both directions (binary switching): in this case it is possible to completely switch from one molecular structure into the other by exhaustive irradiation (typically provided by LEDs). The PSS can be determined from the ratio of the (ground state) absorption spectra of both molecular structures and the quantum yield ratio. The quantum yield (Φ) ratio measures the likelihood of molecules returning from the excited state potential to one or the other (a or b) structure and is typically wavelength-independent.[29]

$$PSS(\lambda) = \frac{c_a(\lambda)}{c_b(\lambda)} = \frac{\Phi_b}{\Phi_a}\frac{A_b(\lambda)}{A_a(\lambda)}. \tag{1.6}$$

Achieving PSS also requires sufficient absorption oscillator strength, which along with the quantum yield determines the speed of the photoreaction. For unaltered AB, the PSS is only moderate.[30] Therefore for actual applications AB requires further substitutions to improve its PSS. One state-of-the-art AB photoswitch adds a carbon-carbon linker at the ortho-positions of the phenyl rings (bridged azobenzene).[7] Remarkably this results in the Z-isomer to become the global energy minimum. For this AB, $E \rightarrow Z$ isomerization was determined to be nearly 100%, however, the backswitching $Z \rightarrow E$ PSS was 'only' ca. 90%. Interestingly, this photoswitch was discovered to exhibit very rapid photoisomerization dynamics in its E-isomer, approaching that of the Z-isomer.[31] Notably, the quantum yield of the E-isomer also increased allowing for faster photoswitching. The swift relaxation of the excited E-isomer stands in contrast to the typical behavior observed in ABs, where its dynamics are significantly slower compared to the Z-isomer.[32, 33]

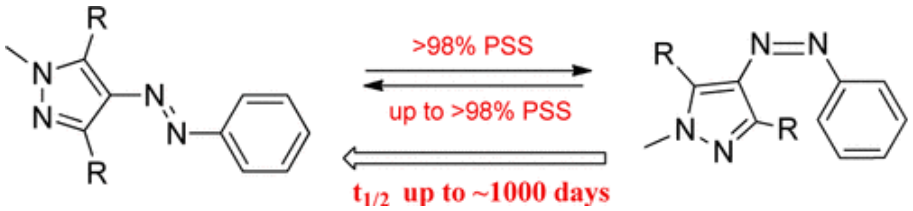

Figure 1.6: Arylazopyrazole isomers, known as AAPs, with dimethyl groups in the ortho-position of the pyrazole ring, exhibit nearly 100% bi-directional photoswitching capability. The thermal half-life time of AAPs can be as high as multiple years (reprinted with permission from [4]).

The fundamental drawback of limited $Z \rightarrow E$ backswitching in ABs was addressed in 2014 when Fuchter and colleagues introduced a novel class of azo-based photoswitches known as arylazopyrazoles (AAPs). Moreover, within this class, many substituted molecules exhibited a notably high Z-isomer thermal stability which can be as high as years.[4, 6] The enhanced backswitching behavior was attributed to the substitution of the phenyl ring with a less bulky five-membered pyrazole ring. This substitution decreases the steric clash between the Z-isomer phenyl ring and the azo group. This enables two additional dimethyl groups in the ortho-position of this pyrazole ring to optimize the Z-isomer geometry and enhance the $n\pi^*$ absorption.[4] The enhanced back-switching compared to AB enables certain members of the AAP class to achieve photoconversion yields exceeding 98% in both directions, thus obtaining a nearly perfect binary molecular photoswitch.

For these reasons, the potential applications of AAPs are currently being rapidly examined.[34, 35, 36] [37, 38, 39] However, unlike ABs, these molecules have not been extensively studied in terms of their ultrafast photoisomerization dynamics. One question that arises is whether the presence of dimethyl groups could alter the rotational reaction dynamics by interactions with the central azo moiety.

Wang *et al.* carried out nonadiabatic dynamics simulations to predict that AAPs are likely to exhibit similar excitation energies, conical intersections, and S_1 potential energy surface in comparison to ABs.[40] Consequently, it can be inferred that AAPs would also undergo a slower E-isomer photoisomerization, akin to ABs, possibly leading to the lower quantum yields reported for most E-isomers compared to the Z-isomers.[31, 6]

Interestingly this problem could be resolved for ABs by the aforementioned bridged AB which gives the E-isomer a twisted preorientation of the between the phenyl rings.[31] It was proposed that the significance of such preorientation in photoisomerization dynamics arises from metastability at the Franck-Condon state on the excited state potential surface of planar ABs, which significantly slows the initial phase of isomerization.[41, 42]

A similar preorientation was also attained for a member of the AAP class by introducing additional steric hindrance through ortho-substitutions on the benzene rings (AAP-4).

This allows the hypothesis that this type of AAP should display uniquely faster photoswitching dynamics in comparison to regular planar *E*-AAP derivatives. To test this, an experimental investigation using transient absorption was carried out on the four water-soluble AAPs, as depicted in Fig. 1.7.

The first pair of AAPs are AAP-1, featuring a hydrogen atom, and AAP-2, which contains an electron-donating methoxy group at the para-position of the phenyl ring. Both AAP-1 and AAP-2 are expected to have a planar *E*-isomer ground state minimum. AAP-2 stands out in comparison to AAP-1 as it functions as an almost molecular binary photoswitch ($>$ 98% PSS in both directions), which is useful as it simplifies the extraction of $E \rightarrow Z$ and $Z \rightarrow E$ photoswitching dynamics.

For comparison, we examine two twisted AAPs, AAP-3, featuring a single methyl group, and AAP-4, containing two methyl groups positioned ortho to the phenyl ring. However, it is anticipated that *E*-AAP-3 will exhibit only minimal twisting and remain nearly planar in its ground state. Conversely, *E*-AAP-4 is expected to display significant twisting (ca.27°).[6]

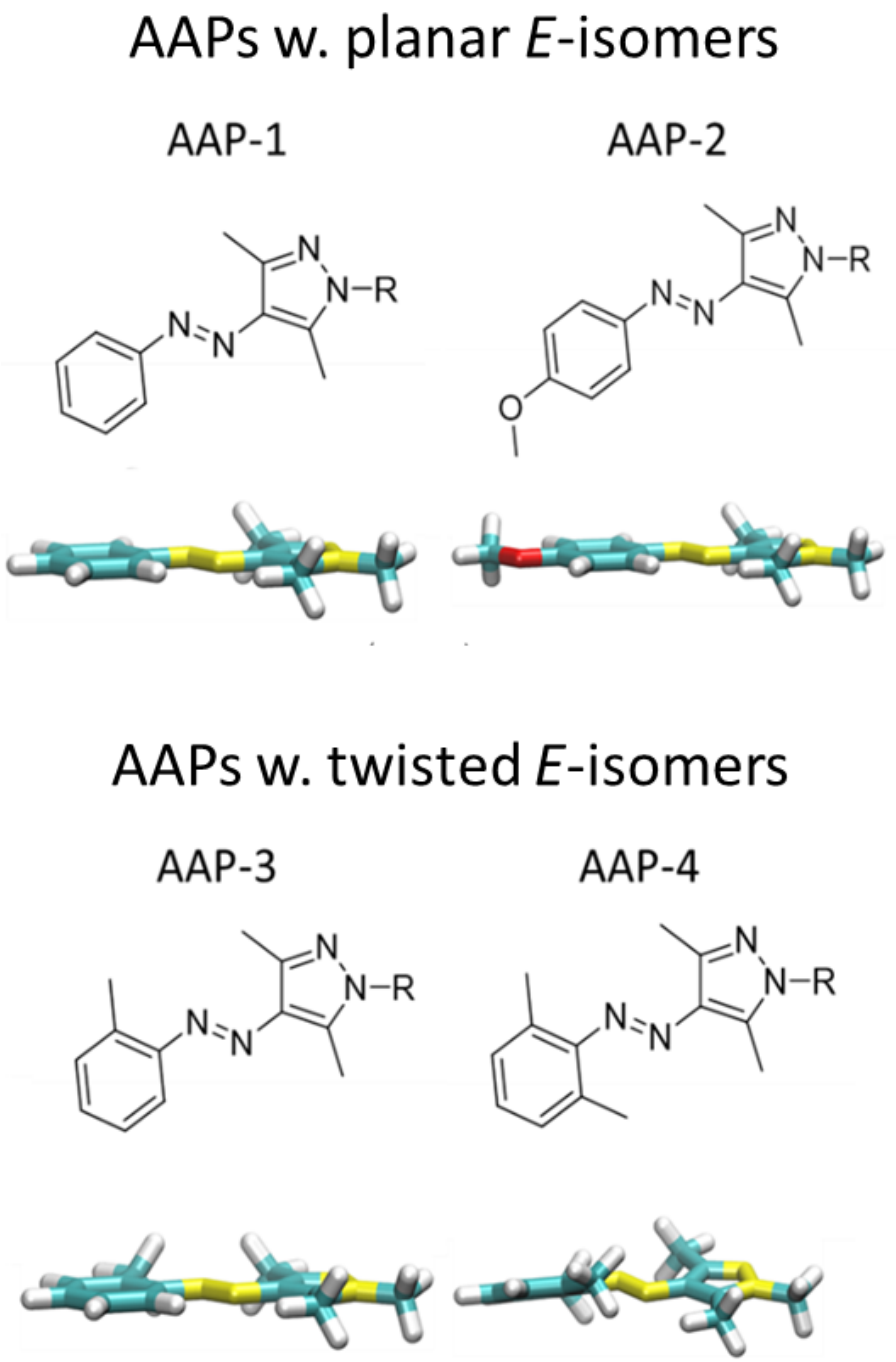

Figure 1.7: The ultrafast photoisomerization dynamics of four AAPs were examined, two of which possess planar (top) and two twisted (bottom) *E*-isomers. The skeletal structure of each molecule is depicted with a side-view illustration below. A TEG group at the pyrazole ring (denoted as R) renders all AAPs water-soluble (reprinted and modified from [1]).

1.2 Kerr-gated UV Resonance Raman Spectroscopy

Traditionally, Raman spectroscopy of fluorescent compounds is conducted at near-infrared (NIR) frequencies, where only a few but large and greatly conjugated molecules have electronic resonances. This approach helps to avoid the co-generation of interfering fluorescence. However, UV-resonant Raman excitation offers several potential benefits. Firstly, when the Raman excitation aligns with an electronic transition, the probabilities of Raman transitions are enormously enhanced, by factors up to 10^7.[43] Secondly, the Raman scattering intensity is intrinsically proportional to the fourth power of the excitation light frequency. Thus, employing higher frequency UV excitation leads to an overall larger scattering cross-section. A third advantage is that by adjusting the frequency, specific regions of the molecule can be selectively targeted, this factor can be exploited in large protein molecules in which many Raman bands in non-resonant spectra overlap.[44] Finally, a fourth advantage is that the resonant signal has the potential to also reveal electronic information.

However, resonance Raman typically does not exhibit the same relative magnitudes of Raman peaks as in non-resonant Raman. To understand this qualitatively but also be able to simulate such spectra, the Raman signal is decomposed into A, B, C, and D terms.[45] A brief theory of the resonance Raman effect will be given in the first subsection.

In the typical approach to resonance Raman spectroscopy, excitation on the first electronic excited state is avoided, and excitation is conducted on higher excited states. In these instances, the Stokes shift shifts the fluorescence away from the Raman signal via non-radiative relaxation.[46] The phenomenon where the fluorescence spectrum is independent of wavelength, beginning its emission at the lowest electronic and vibrational state, is called Kasha's rule, which most molecules, with few exceptions, obey.[47]

In some cases, conducting Resonance Raman at peak fluorescence frequencies cannot be avoided. For example, if multiple molecules in a single sample are investigated, a broad excitation tuning range is required or alternatively, as is the case in this thesis, if excitation on the first electronic state is intentionally performed to investigate its resonance Raman excitation profiles. In such cases, fluorescence can be further suppressed by using a Kerr gate.[48] This need arises because, despite the substantial Raman enhancement factor for resonant excitation, (single photon) absorption which produces fluorescence still has cross sections typically $10^7 - 10^9$ greater than even that of resonance Raman scattering.[49]

The detected signal in Kerr-gated (resonance) Raman is a combination of the spontaneous Raman effect with the nonlinear optical Kerr effect (OKE), which necessitates pulses. At first glance, using a nonlinear effect to modify a linear signal typically not requiring a

pulsed laser source might seem overly complex when considering that techniques like SRS or CARS can achieve additional signal enhancement and are less susceptible to the effects of fluorescence. However, as previously mentioned, the resonance enhancement of spontaneous Raman, coupled with augmented scattering from UV excitation, often results in a notably strong spontaneous Raman signal on its own. Moreover, the spontaneous Raman signal does not necessitate an additional broadband Stokes field, simplifying the experiment's complexity and analysis. Furthermore, the pulsed source enables the use of the OPA process, providing an easily adjustable Raman excitation source for measuring Raman excitation profiles. Fluorescence suppression using a Kerr gate for resonance Raman spectroscopy is detailed in the second subsection.

The Resonance Raman effect

Predicting the strength of Raman modes of molecules is only possible using a quantum mechanical description. Since the Raman technique is an indirect method of probing nuclear bond resonances within a molecule, the observed Raman magnitudes are in principle intertwined with both electronic properties and the characteristics of bond vibrations.

It can be shown that for light scattering by a molecule much smaller than the incident wavelength of light (with an incident frequency ν_0) and an incident intensity (I_0), one can derive the spontaneous Raman signal for a vibrational transition k over all orientations of the molecule using the following relation [45]:

$$I_k = \frac{2^7\pi^5}{3^2c^4} I_0(\nu_0 + \nu_k)^4 \sum_{\rho,\sigma} \left|(\alpha_{\rho,\sigma})_k\right|^2 . \tag{1.7}$$

The term $(\alpha_{\rho,\sigma})_{fi}$ represents the transition polarizability tensor, ρ and σ denote orthogonal Cartesian coordinates. From second-order perturbation theory, a general description of the Raman scattering process is obtained for each vibrational transition k (Kramers-Heisenberg-Dirac equation):[50, 51, 52]

$$(\alpha_{\rho,\sigma})_k = \frac{1}{\hbar} \sum_{e \neq i,f} \left\{ \frac{\langle f | M_\rho | e \rangle \langle e | M_\sigma | i \rangle}{\omega_{ei} - \omega_0 - i\Gamma_e} + \frac{\langle f | M_\sigma | e \rangle \langle e | M_\rho | i \rangle}{\omega_{ei} + \omega_0 + i\Gamma_e} \right\} . \tag{1.8}$$

Here, Γ is the dampening constant, i represents the initial vibronic state, e an excited vibronic state and f the final vibronic state. The two wavefunction overlap integrals in the numerators for each fraction correspond to the dipole transition moments, here M is the electron position operator.

In the scenario of non-resonant Raman scattering, the denominators become large, and not only a single excited state is responsible for the Raman scattering.[51] In this in-

stance, Raman scattering can be viewed purely as a property of the electronic ground state.[52] However, if the excitation frequency ω_0 is approximately equal to that of an excited vibronic transition ω_{ei}, the denominator becomes small causing the first term to predominate. Subsequently, the Born-Oppenheimer approximation is applied to represent the vibronic states as a product of electronic and vibrational wavefunctions. By excluding the non-resonant second term in Eq. 1.8 the transition polarizability tensor can be simplified to:

$$(\alpha_{\rho,\sigma})_k = \frac{1}{\hbar} \sum_{e \neq i,f} \frac{\left\langle v^f \left| (\mu_\rho)_e \right| v^e \right\rangle \left\langle v^e \left| (\mu_\sigma)_e \right| v^i \right\rangle}{\omega_{vi} - \omega_0 - i\Gamma_v}. \tag{1.9}$$

Here v^i ,v^e and v^f are the vibrational wavefunctions of the initial, excited and final states, respectively. The terms $(\mu_\rho)_e$ and $(\mu_\sigma)_e$ are the electronic transition dipole moments. The (crude) Born-Oppenheimer approximation, in which the excited electronic state is defined by nuclear equilibrium positions, is then corrected by expanding the electronic dipole transition moment in a Taylor series to the first order for every vibration with a normal coordinate Q_k:

$$\mu_e = \mu_e^0 + \sum_k \mu_e^1 Q_k + \dots . \tag{1.10}$$

The first term μ_e^1 can be expressed using the electronic Hamiltonian and allows for vibronic mixing of the the electronic excited state $|e\rangle$ with a second excited state $|s\rangle$.

$$\mu_e^1 = (\partial \mu_e / \partial Q_k)_0 = \mu_s^0 \frac{\langle v^s \left| (\partial H_e / \partial Q_k)_0 \right| v^e \rangle}{\omega_s - \omega_e}. \tag{1.11}$$

After the insertion of Eq. 1.11 and Eq. 1.10 into 1.9 the polarizability tensor in the resonance case can be expressed as a sum of contributions:

$$(\alpha_{\rho\sigma})_k = A + B + C + D + \dots . \tag{1.12}$$

Here only the A, B and C terms will be written out in the following since the D term usually is negligible (often also the C term can be neglected).[51]

$$A = \frac{1}{\hbar}(\mu_e^0)^2 \sum_{v^e} \frac{\langle v^f | v^e \rangle \langle v^e | v^i \rangle}{\omega_{ei} - \omega_0 - i\Gamma_v} \tag{1.13}$$

$$B = \frac{1}{\hbar^2}\mu_e^0 \mu_e^1 \sum_{v^e} \frac{\langle v^f | Q_k | v^e \rangle \langle v^e | v^i \rangle + \langle v^f | v^e \rangle \langle v^e | Q_k | v^i \rangle}{\omega_{ei} - \omega_0 - \mathrm{i}\Gamma_e} \tag{1.14}$$

$$C = \frac{1}{\hbar^2}(\mu_e^1)^2 \sum_{v^e} \frac{\langle v^f | Q_k | v^e \rangle \langle v^e | Q_k | v^i \rangle}{\omega_{ei} - \omega_0 - \mathrm{i}\Gamma_e}. \tag{1.15}$$

These equations were simplified and do not account for potential differences in electronic transition dipole moments between the transition from the electronic ground state to the excited state and the return transition from the excited state to the ground state. A less simplified version of these equations can be found in [52]. The contributions from A, B and C terms, will be qualitatively discussed below. It is assumed that the ground state serves as both the initial and final state, as this is the most probable case.

A-Term The A-term, also known as the Franck-Condon term, involves only a single excited electronic state. As indicated in Eq. 1.13 this contribution occurs if there is an electronic transition dipole moment μ_e^0 from the ground to the excited state, without perturbation by vibronic coupling. As μ_e^0 is directly related to the absorption oscillator strength, the A-term scattering is particularly dominant if ω_0 is tuned to a strong absorption band. However, for A-term scattering the vibrational wavefunction overlap integrals $\langle v^g | v^e \rangle \langle v^e | v^g \rangle$ must be nonzero. This requires that the vibrational energies of v^g and v^e are altered.[52] This is true if the excited state potential is more shallow or steeper compared to the ground state. Another scenario is when the nuclear equilibrium positions are altered. In the case that the nuclear equilibrium positions (a typical situation) change from the ground to an excited state only totally symmetric Raman modes are selectively enhanced in resonance Raman spectra by A-term scattering. If the change in nuclear equilibrium positions is particularly large, overtones may become very intense in the spectrum.

B-Term The B-term (Eq. 1.14) depends on the energy difference of the two excited states e and s, which are coupled as depicted in Eq. 1.11. Since $\mu_e^1 \sim \mu_s^0$, this term will be particularly significant for example if the absorption oscillator strength of a nearby state s is much larger than that of e. B-term contribution for totally symmetric modes requires that the vibronically coupled excited states e and s have the same symmetry.[53] This scenario is atypical since neighboring excited states usually have different symmetry.

Therefore the B-term is usually only important for symmetry-changing modes (non-totally symmetric modes). Furthermore, unlike A-term scattering, the B-term integrals are zero for vibrational level changes of more than one quantum between the ground and excited states. For this reason, the B-term does not yield any overtones.

C-Term The C-term couples vibrational states differing by two quanta and is therefore a potentially important contribution to the first overtones and combination modes. Notably, the C-term is solely proportional to $(\mu_e^1)^2$ and does not incorporate μ_e^0. Consequently, the C-term may be non-negligible when Raman excitation originates from a forbidden or weakly allowed excited state.[51]

Optical Kerr Effect and Principle of a Kerr Gate

The Optical Kerr Effect (OKE) is a third-order optical response, giving rise to important phenomena like self-focusing and self-phase modulation.[54, 55] This effect involves the interaction of a strong light field with itself, leading to nonlinear optical effects even when only a single frequency is present. One notable application of self-focusing is passive mode-locking, a technique utilized to generate ultrafast pulses, as implemented by the Pharos pulsed laser system from Light Conversion.

OKE emerges from the real part of the susceptibility $\chi^{(3)}$. This effect therefore manifests also off-resonance and, similar to the normal linear refractive index, influences the speed of the light propagation within a medium. It has the following energy and momentum conservation relations for a strong pulse interacting ω_{kerr} with a weak pulse ω_{probe}:

$$\overrightarrow{k_{probe}} = \overrightarrow{k_{probe}} + \overrightarrow{k_{Kerr}} - \overrightarrow{k_{Kerr}} \tag{1.16}$$

$$\omega_{probe} = \omega_{probe} + \omega_{Kerr} - \omega_{Kerr}. \tag{1.17}$$

In this four-wave-mixing process, there is no energy exchange, and the process is intrinsically phase-matched, meaning that the signal follows the probe direction. Conversely, the speed of light propagation, and more significantly for the Kerr Gate, polarization, can be altered. In an isotropic medium, three distinct third-order susceptibilities suffice to describe all types of OKE four-wave-mixing responses from the medium: χ_{1122}, χ_{1212} and χ_{1221}, which induce a temporary birefringence in the medium. It's important to note that the polarizability, which does not induce a change in polarization (as in the case of self-phase modulation), is determined by these independent components:[56]

$$\chi_{1111} = \chi_{1122} + \chi_{1212} + \chi_{1221}. \tag{1.18}$$

If the Kerr pulse is polarized at a 45° angle to the probe pulse, the polarization of the probe pulse can experience polarization rotation through the orthogonal tensor elements. This rotation is due to the Kerr pulse-induced phase delay between the parallel and orthogonal polarization components of the probe light field. This "rotation" due to phase delay means that the linearly polarized light converts from elliptical to circular and finally to orthogonal linear polarization. In essence, depending on the strength of induced birefringence, the Kerr medium can behave similarly to both a quarter-wave or half-wave plate for the probe. The Kerr pulse-induced phase retardation $\Delta\phi$ in relation to the susceptibility tensor elements is as follows:[57]

$$\Delta n = n_{\parallel} - n_{\perp} = \frac{2\pi}{n}(\chi^{(3)}_{1111} - \chi^{(3)}_{1122})I_{Kerr}(t) \tag{1.19}$$

$$\Delta\phi = \frac{\omega}{c}\Delta n L. \tag{1.20}$$

Here, n represents the linear refractive index, and L signifies the interaction length between the pulses in the medium. In this description of the refractive index change, it was assumed that polarization follows the Kerr field instantaneously, which is an accurate depiction of the induced electronic polarization due to its swift response time, typically on the order of 0.1 fs.[57] However, in liquids, the field can affect the motion of entire molecules. For instance, light excitations can induce molecular shaking (libration). Moreover, in anisotropic molecules, a dipole is generated by the field along its symmetry axis, leading to molecular reorientation as the molecules experience an aligning torque. Additionally, collisions between molecules also contribute to the nonlinear susceptibility. These collective effects are referred to as nuclear contributions; since molecules are orders of magnitude heavier than electrons, nuclear response times are approximately four orders of magnitude slower, typically in the picosecond regime.[57] Consequently, the response time of nuclear contributions is often slower than the pulse lengths in modern laboratories. For long pulses, the nonlinear susceptibility tends to build up, causing a delay in the response and generating orders of magnitude greater refractive index changes than in the case of pure electronic polarization. The combined contributions of the nuclear refractive index can in most cases be expressed as:[58]

$$\Delta n(t) \sim n_{2,el} I_e(t) + \sum_m n_{2,m} \int_{-\infty}^{\infty} r_m(t - t') I_{kerr}(t') dt'. \tag{1.21}$$

Here $r_m(t)$ represents the normalized response function, $n_{2,el}$ denotes the induced electronic refractive index change, and n_{2m} signifies the nonlinear refractive index, with m indicating the corresponding nuclear mechanism. The typical, slow nuclear responses can be modeled by the product of an exponential decay combined with a delayed rise time to describe the delayed response: [59, 60]

$$r_{slow}(t) \sim e^{-t/t_{slow}}(1 - e^{(-t/t_{rise,1})}). \tag{1.22}$$

A Kerr gate utilizes the polarization rotation caused by the Kerr field by passing the probe light through a crossed polarizer configuration with the Kerr medium positioned between these polarizers. The elliptical polarization induced by the Kerr pulse enables the generated vertical probe polarization component to be transmitted. Consequently, the transmitted signal has the following relation to the previously mentioned phase shift:[61]

$$I_{transmitted} \sim sin^2\left(\frac{\Delta\phi(I_{kerr}, n_2, L)}{2}\right) = sin^2\left(\frac{\pi L \Delta n(\lambda_{kerr})}{\lambda_{probe}} I_{kerr}(t)\right). \tag{1.23}$$

As an example, for a 90° phase shift (resulting in a circularly polarized probe field), an observed transmission of 70% through the Kerr gate can be expected. The achievable phase retardation depends on the nonlinear refractive index of the Kerr medium and the power of the Kerr gate pulse. Consequently, a substantial amount of Kerr gate power (multiple Watts) is typically necessary. Additionally, the Kerr medium must be transmissive for the probe frequency employed. For instance, when using a UV probe, the commonly used Kerr gate medium carbon disulfide, with its extremely high nonlinear refractive index absorbs the probe and cannot be used.

The principle of the Kerr Gate can be used to suppress fluorescence in resonance Raman spectroscopy by using the scattered light as a probe thereby filtering the Raman signal in the time-domain.[62, 63, 64] In spontaneous Raman there are three incoherent signal contributions: Rayleigh scattering at incident frequency, the Raman scattering with a fs-ps response time and fluorescence which decays slowly typically with a ns relaxation time based on an excited state population.[62] Rayleigh scattering can simply be suppressed by using a longpass spectral filter. Additionally, fluorescence can be suppressed through the use of a Kerr gate which involves synchronizing the Kerr pulse with the initial scattered light containing the entire Raman signal but only a small portion of the fluorescence.

Ideally, to suppress fluorescence, it would be optimal to utilize a Raman probe and Kerr pulses that are as short as possible, paired with a Kerr medium possessing a response time shorter than these pulse durations. Unfortunately, the Fourier transform limit poses a constraint, since spontaneous Raman measurements require spectrally narrow pulses. As a result, Raman probe pulses inherently span multiple picoseconds, which in practice limits the potential for fluorescence suppression.[62] The achievable fluorescence suppression, represented by the contrast between the two signals, is as detailed by Everall *et al.*: [65, 62]

$$f_{R/B} \approx \frac{1}{(1 - e^{-\frac{\tau_g}{\tau_f}}) + \frac{\gamma}{\beta} + \frac{2b}{B\alpha\beta}}. \tag{1.24}$$

Here, τ_F represents the fluorescence lifetime, τ_g the time duration during which the Kerr gate is opened by the pulse, β signifies the percentage of Kerr-gated light attributed to the achieved phase retardation in the Kerr gate, γ refers to the extinction ratio of the polarizers, and b denotes the noise introduced by the Kerr gate pulse. B represents the absolute fluorescence measured without the Kerr gate, while α accounts for the transmittance losses in the Kerr gate (signal when both polarizers are parallel). Fluorescence rejection is reduced by the fluorescence gated alongside the Raman signal, which is incorporated by the term $1 - e^{-\frac{\tau_g}{\tau_f}}$. The equation above underscores the significant influence of the sample being analyzed on the Kerr-gated Raman technique's ability to suppress fluorescence. This influence encompasses the absolute fluorescence generation, which depends on the fluorescence quantum yield and fluorescence lifetime.

Another significant consideration, which may vary in importance depending on how dispersion is introduced from collection to the Kerr gate medium, is group velocity dispersion (GVD). Group velocity dispersion leads to a spreading of the frequency components in the time domain, i.e higher wavenumber Raman light will reach the Kerr medium faster than those of lower wavenumbers. The same effect also occurs for the broad fluorescence spectrum. A summary of the impact of GVD on the various signals is depicted in Fig. 1.8. The influence of group velocity dispersion (GVD) can be lessened by opting for smaller diameter, that is, thinner lenses or even solely using parabolic mirrors.[48]

Another significant distinction between the signals of "normal" spontaneous Raman measurements and Kerr-gated Raman measurements is that the latter must be intrinsically polarization-sensitive. In Kerr-gated Raman measurements, only the parallel Raman light passes the first polarizer. This can be exploited by the simple addition of a half-wave plate, with which the Raman probe laser polarization can be rotated by 90° to solely measure the perpendicular contribution in order to obtain the depolarization ratio of Raman modes.

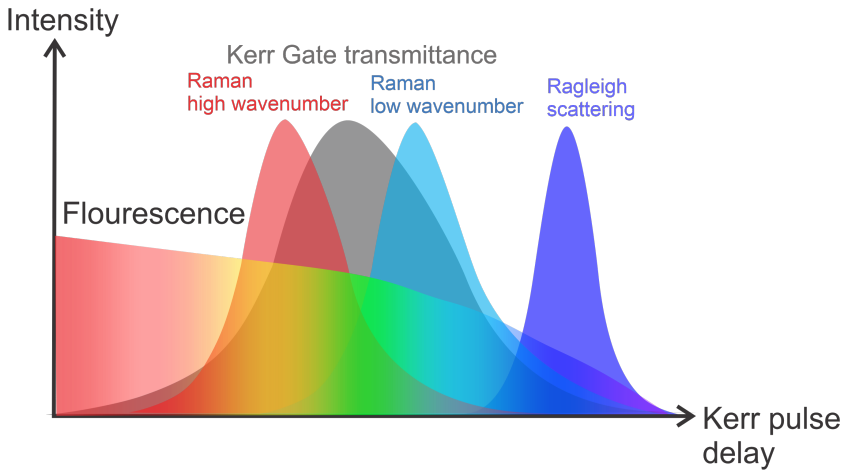

Figure 1.8: Impact of group velocity dispersion in a Kerr gated Raman experiment. The figure illustrates the scenario where the Kerr pulse is synchronized with the Raman light (red and blue curves), along with the slower blue-shifted Rayleigh-scattered light shown in purple and the Kerr gate response (gray).

In the case of resonance Raman, this can lead to useful additional information. For instance, for totally symmetric modes, A-term scattering is the dominant Raman scattering process, occurring only along the specific axes of the transition moment of the electronic state. If the transition moment of the excited electronic state is associated with a single axis only, the depolarization ratio should, in an ideal case be 1/3.[52]

Anthracene

The resonance Raman study in this thesis will center on the exploration of anthracene, a rigid polycyclic aromatic hydrocarbon comprised of three fused benzene rings, characterized by extensive π-electron delocalization. Moreover, the molecule belongs to the high-symmetry point group D_{2h}. A foundational understanding of polycyclic aromatic hydrocarbons stems from Platt's ring perimeter model, a refinement of Hückel's molecular orbital theory, which is only accurate for monocyclic molecules.[9] In this model, the polycyclic molecule is characterized by a perimeter orbital, allowing an electron to move freely within this loop and an inner core. Through this approximation, the fundamental electronic state structure and absorption features of these molecules were first established.

In Fig. 1.9, the two distinct resonances present in the absorption spectrum of this molecule are shown. These transitions come in two types: Firstly, a transition with significantly higher oscillator strength occurs near 250 nm. This transition along the in-plane axis is strongly dipole-allowed and is identified as ^1B_b (irreducible representation B_{1b}, $x \rightarrow 1$) in Platt notation. The transition dipole from the ground state to this excited state aligns along the long axis of the anthracene molecule. Moreover, there exist two nearly degenerate electronic L states (Platt notation) of the same symmetry at lower excitation energy, ^1L_a (B_{2b}) and ^1L_b (B_{3b}), which have dipole transition moments along the short and the long axis of the molecule, respectively.[66] However, the absorption is predominantly determined by the ^1L_a state. The state ^1L_b has a negligible absorption magnitude and is predicted to reside at higher energy compared to that of the ^1L_a state in anthracene.[67] Transitions from the anthracene ground state to the L states are pseudo-parity forbidden, as such transitions necessitate a significant change in angular momentum.[9] Nevertheless, the ^1L_a state becomes somewhat allowed and thus visible in an absorption spectrum due to vibronic coupling with anti-symmetric b_{1u} and b_{2u} vibrations.[9, 68] Compared to the ^1B_b state within the ^1L_a band, the absorption spectrum also reveals some vibronic fine structure, largely this visible fine structure can be attributed to the molecule's high D_{2h} symmetry. This means that only 66 normal modes can exist, 33 are Raman and 28 are IR-active.[69] Specifically, for vibronic transitions in absorption, only the 23 a_g and b_{1g} are expected to contribute.[70]

Finally, it's crucial to note an important property of anthracene for conducting resonance Raman at the ^1L_a state, which is the reversible dimerization reaction of anthracene which occurs by UV exposure (illustrated in Fig. 1.10). Anthracene dimerization occurs for wavelengths above 300 nm, while below 300 nm, anthracene dimers photodissociate back into anthracene.[72] Importantly, the π conjugation in the photodimer is disrupted, forming a structure akin to four linked benzene rings. This causes its absorption spectrum to shift to below 300 nm.[73]

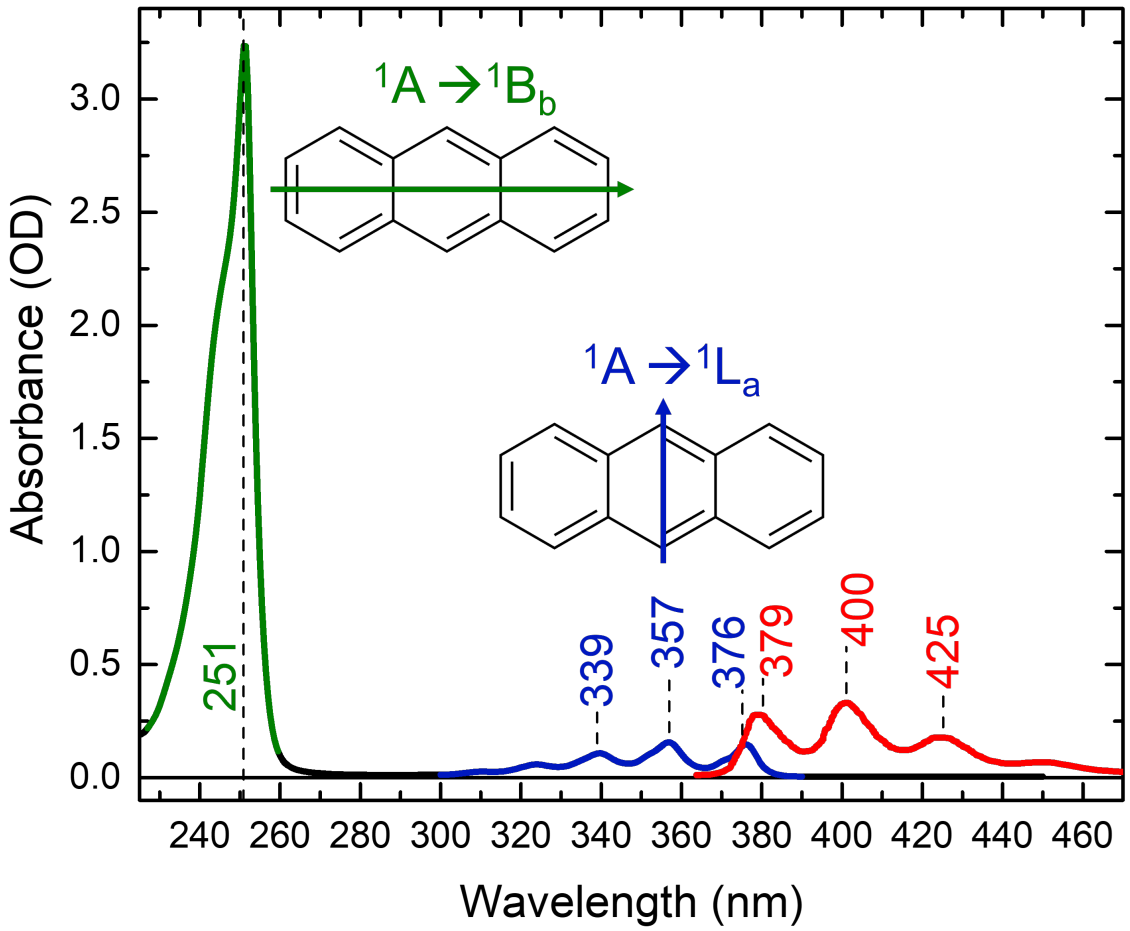

Figure 1.9: Absorption spectra of the two excited states, ^1B_b (green) and ^1L_a (blue) of anthracene in acetonitrile (c=0.1 mM). The transition dipole axes associated with each transition are displayed, indicated with arrows on the anthracene skeletal structures. Additionally, the fluorescence spectrum in arbitrary intensity (red, data from [71]) highlights the necessity for fluorescence suppression for Raman measurements in resonance with the ^1L_a state.

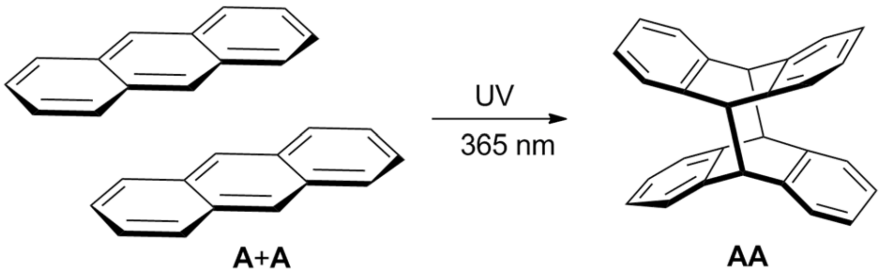

Figure 1.10: On the left are a pair of anthracene molecules, which, upon photoexcitation, combine to form the dimer shown on the right (reprinted with permission from [74]).

1.3 Heterodyne Detected CARS-ROA

In this section, coherent anti-Stokes Raman scattering (CARS) is briefly introduced which is followed by an explanation of a type of CARS measurement technique (heterodyne CARS-ROA) with which Raman optical activity (ROA) can be investigated.

CARS is a nonlinear four-wave-mixing process that can be used to measure vibrational modes. In comparison to stimulated Raman spectroscopy (SRS) or spontaneous Raman (arises from zero-point energy), in which case the Stokes field interacts with the sample twice, CARS involves the pump field interaction two times, leading to a signal, blue-shifted from the input fields, at the anti-Stokes Raman frequency (ω_{as}).[75] However unlike spontaneous anti-Stokes Raman scattering, CARS is initiated from the vibrational ground state rather than the less populated excited vibrational states.[76] Therefore CARS produces a strong Raman signal at the anti-Stokes frequency. Due to the blue shift, CARS is an excellent Raman technique with which to avoid interfering fluorescence. Unfortunately, however, CARS suffers from the interference of another four-wave-mixing process that does not involve any vibrational modes called non-resonant background (NRB). As its name suggests NRB is always present regardless if Raman excitation occurs in the vicinity of an electronic state or not. Normal Raman and CARS, along with their primary competing interfering processes, fluorescence and four-wave-mixing, respectively, are illustrated in ladder diagrams in Fig. 1.11.

For degenerate CARS in which case both pump interactions originate from the same pulse, the phase-matching and energy conservation conditions are:

$$\vec{k_{as}} = 2\vec{k_{pu}} - \vec{k_s} \tag{1.25}$$

$$\omega_{as} = 2\omega_{pu} - \omega_s. \tag{1.26}$$

From this relation, it becomes evident that if both Stokes and pump fields are completely collinear and interact with a dispersive medium, there will be a phase mismatch.[77]

However, for two collinear pump and Stokes beams, phase matching will typically still be achieved if the beams are focused by a lens on a medium, as the fields interact over a range of $\vec{k}$-vectors.[78] In the collinear geometry the input pump and Stokes fields are subsequently removed by a spectrometer in combination with a short pass filter. In comparison to the homodyne detection in TA and SRS, the CARS signal behaves like a "normal" four-wave-mixing experiment and its intensity includes an electric field factor for each interaction. This leads to a square dependence of the pump beam intensity to the CARS signal:[79]

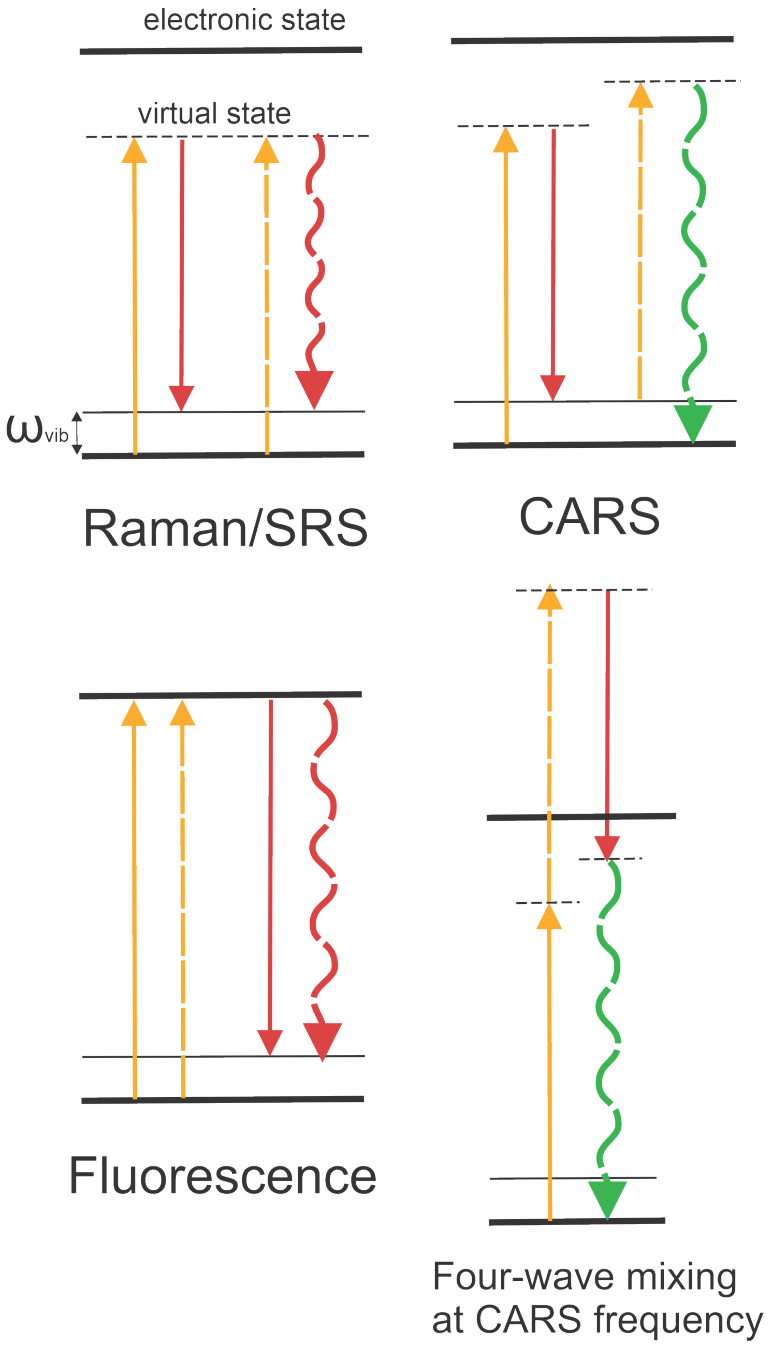

Figure 1.11: Illustration of two Raman processes: Linear Raman and SRS (top-left) and CARS (top-right). In the diagrams, bold lines represent the electronic states, while thin lines depict the electronic-vibrational states with an additional vibrational quantum. Virtual levels are shown as dashed lines. Below each, the two primary competing interfering processes for each Raman technique are depicted. The upward arrows represent individual absorption interactions, while the downward arrows signify stimulated emission interactions. The emitted signal is depicted as a wavy line.

$$I_{as}^{CARS}(z,t) \sim \omega_{as}^2 N^2 \left|\chi^{(3)}\right|^2 I_{pu}^2 I_s L^2 sinc^2\left(\frac{\Delta kL}{2}\right). \tag{1.27}$$

Here N represents the number of excited molecules in the interaction volume, L is the interaction length and Δk is the phase mismatch. The third-order nonlinear susceptibility tensor can, in the electronically non-resonant case, be decomposed into three components: the imaginary (out of phase) Raman vibrationally resonant susceptibility, the real (in-phase) Raman susceptibility, and the electronic third-order dispersion denoted as $\chi_{Re}^{(3)NR}$.[77]

$$\left|\chi^{(3)}\right|^2 = \left|\chi_{Re}^{(3)R} + i\chi_{Im}^{(3)R} + \chi_{Re}^{(3)NR}\right|^2 \tag{1.28}$$

$$= \left|\chi_{Re}^{(3)R}\right|^2 + \left|\chi_{Im}^{(3)R}\right|^2 + \left|\chi_{Re}^{(3)NR}\right|^2 + 2\left|\chi_{Re}^{(3)NR}\right|\left|\chi_{Re}^{(3)R}\right|. \tag{1.29}$$

Notably, the electronic third-order dispersion $\left|\chi_{Re}^{(3)NR}\right|^2$ can be approximated as frequency-independent. Due to the relatively large electronic third-order dispersion $\chi_{Re}^{(3)NR}$ compared to the Raman terms, CARS typically exhibits a significant background, with a shape resulting largely from the convolution of the Stokes and pump field spectra. In general, CARS Raman lineshapes, without employing advanced techniques like polarization-sensitive or dephased detection, also deviate considerably from ideal Lorentzians due to the mixed term $\left|\chi_{Re}^{(3)NR}\right|\left|\chi_{Re}^{(3)R}\right|$.[77] This is in contrast to the homodyne Raman signal measured in SRS, which is sensitive to only the imaginary component of $\chi^{(3)}$. Unfortunately, most advanced CARS techniques which defeat non-resonant background signal also significantly reduce the overall signal.[77]

The signal from the susceptibility tensor $\chi^{(3)}$ of CARS is influenced by the polarization of the input fields. In isotropic media and under the electric dipole approximation, there are only two distinct third-order susceptibilities that can be measured in degenerate CARS $\chi_{1111}^{(3)}$ and $\chi_{1221}^{(3)}$. The subscripts here indicate the orthogonal polarization directions of the involved electric fields. Therefore in collinear CARS with two linearly polarized beams, the signal originating from these susceptibilities is influenced by the orientation between the Stokes and pump beam polarizations (ϕ). If the Stokes beam is linearly polarized orthogonal to the pump beam, the output CARS field will also be orthogonal and the signal will be dependent on the tensor element $\chi_{2112}^{(3)}$. On the other hand, as for a more common CARS experiment when the two input beams are parallel, the output field is also polarized parallel and proportional to $\chi_{1111}^{(3)}$.

However, this becomes more complex when the typically neglected induced electric quadrupole polarization ($\chi^{(3)}\nabla\overrightarrow{E}\,\overrightarrow{E}\,\overrightarrow{E}$) and magnetic dipole polarization ($\chi^{(3)}\overrightarrow{B}\,\overrightarrow{E}\,\overrightarrow{E}$) are included in CARS description:

$$P^{(3)} = \chi^{(3)}\overrightarrow{E}\,\overrightarrow{E}\,\overrightarrow{E} + \chi^{(3)}\nabla\overrightarrow{E}\,\overrightarrow{E}\,\overrightarrow{E} + \chi^{(3)}\overrightarrow{B}\,\overrightarrow{E}\,\overrightarrow{E}. \tag{1.30}$$

It was shown in the early 1980's when these additional multipoles are included, a new tensor element becomes non-zero $\chi^{(3)}_{1112}$.[17, 16] This element, while extremely small, is interesting since it contains information on chirality. The actual derivation of this tensor element is quite lengthy and only the main results will be summarized in the following. An in-depth derivation and discussion of the CARS-ROA theory is laid out by V. Kumar and S. Schlücker in a book chapter.[14]

It can be derived using Maxwell's equations that $\chi^{(3)}_{1112}$ is related to the forwards scattering circular intensity difference measured in spontaneous ROA $\triangle(0°)$:[17]

$$\chi^{(3),R}_{1112} = \frac{-i}{2}\triangle(0°)\chi^{(3),R}_{1111}. \tag{1.31}$$

The presence of a non-zero $\chi^{(3)}_{1112}$ tensor element implies that when both pump and Stokes fields are polarized in parallel, a perpendicularly polarized field is generated. In principle, in order to filter out this component, one only needs to place two crossed polarizers with extremely high extinction ratios before and after the chiral sample. The first polarizer should purify the polarization of the incoming laser pulses, while the second polarizer serves as the analyzer to select the signal from $\chi^{(3)}_{1112}$. Directly measuring this chiral field would necessitate nearly perfect polarizers because the achiral field from $\chi^{(3)}_{1111}$ is estimated to be approximately one million times greater than the chiral field $\chi^{(3)}_{1112}$. However, Oudar *et al.* have already proposed a better method to measure this field component by employing the achiral field ($\sim \chi^{(3)}_{1111}$) as a local oscillator.[17, 80]

Similar to transient absorption when a small coherent signal mixes with a larger coherent field (local oscillator) and is detected by a square law detector, this creates a new mixed signal which then makes linear signals that would typically be quadratic functions of χ. Allowing a fraction of the large achiral signal for mixing to pass implies that the polarizers discussed earlier are not completely crossed. Defining $\theta = 0$ as the crossed polarizer position the CARS signal transmitting through the polarizers $I^{Transmitted}_{CARS}$ is:

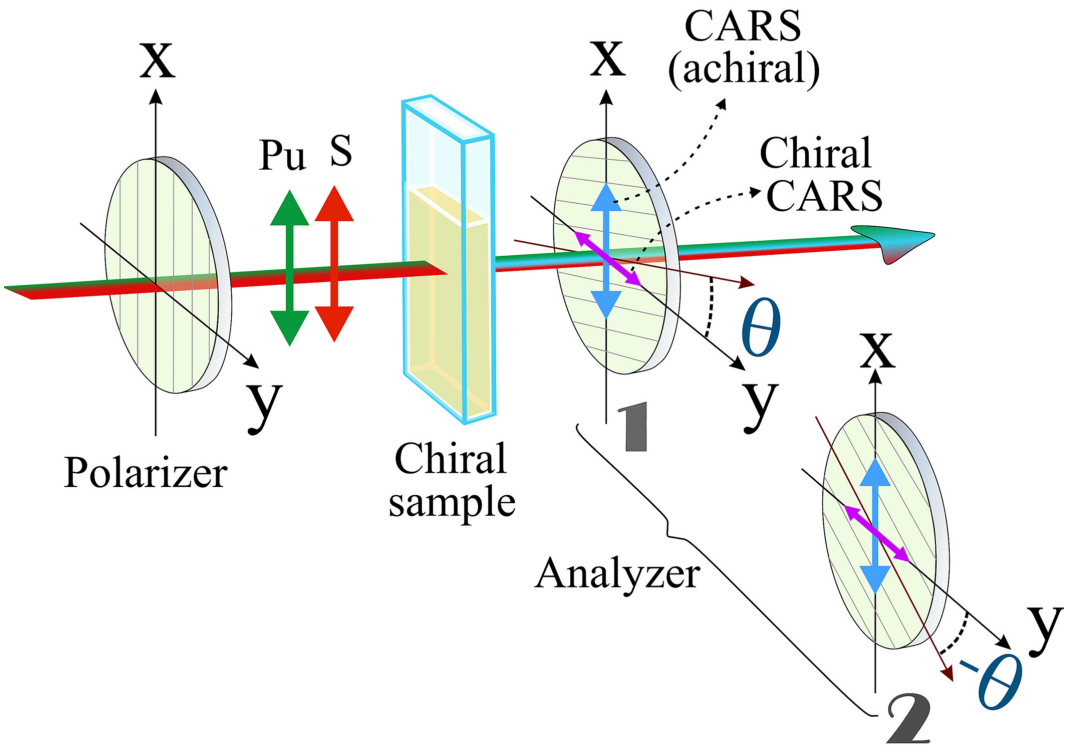

Figure 1.12: Detection scheme of heterodyne CARS-ROA. The green and red double arrows indicate the parallel polarization of the pump and Stokes pulse. The generated achiral and chiral CARS signal is shown by blue and pink double arrows, respectively. At the sample, both achiral and chiral CARS signals are generated. To the right of the sample, the two analyzer positions (θ_1 and $(-\theta_1)$) needed to obtain the chiral CARS spectrum are shown (reprinted with permission from [15]).

$$I_{CARS}^{transmitted}(\theta) = \left|E_{achiral}^{CARS} cos(\theta) + E_{chiral}^{CARS} sin(\theta)\right|^2 \sim \left|\chi_{1112}^{(3)} cos(\theta) + \chi_{1111}^{(3)} sin(\theta)\right|^2 \quad (1.32)$$

$$= \left|\chi_{1112}^{(3)}\right|^2 cos^2(\theta) + \left|\chi_{1111}^{(3)}\right|^2 sin^2(\theta) \quad (1.33)$$

$$+2Re(\chi_{1112}^{(3)*}\chi_{1111}^{(3)}) cos(\theta) sin(\theta).$$

Therefore, if the polarizer is turned slightly off perpendicular ($\theta = \theta_1$), a mix signal $2Re(\chi_{1112}^{(3)*}\chi_{1111}^{(3)})$ is detected, in contrast $\left|\chi_{1112}^{(3)}\right|^2 cos^2(\theta)$ can be neglected. In this context, the signal is termed heterodyne rather than homodyne because the local oscillator $E_{achiral}^{CARS}$ is not directly the source of E_{chiral}^{CARS}. Subsequently in Eq. 1.33 the achiral local oscillator signal $\left|\chi_{1111}^{(3)}\right|^2 sin^2(\theta)$ must be subtracted. This is done by taking a second measurement at the exact mirror angle $(-\theta_1)$ (the two analyzer positions are illustrated in Fig. 1.12).

By subtracting the two CARS spectra, the achiral signal is removed and only the heterodyne term which is related to the spontaneous ROA CID remains:

$$\begin{aligned}\triangle I_{CARS}^{transmitted}(\theta_1) \sim & \left|\chi_{1112}^{(3)}\right|^2 cos^2(\theta_1) + \left|\chi_{1111}^{(3)}\right|^2 sin^2(\theta_1) + 2Re(\chi_{1112}^{(3)*}\chi_{1111}^{(3)})cos(\theta_1)sin(\theta_1) \\ & - \left(\left|\chi_{1112}^{(3)}\right|^2 cos^2(-\theta_1) + \left|\chi_{1111}^{(3)}\right|^2 sin^2(-\theta_1) + 2Re(\chi_{1112}^{(3)*}\chi_{1111}^{(3)})cos(-\theta_1)sin(-\theta_1)\right) \quad (1.34)\end{aligned}$$

$$= 2Re(\chi_{1112}^{(3)*}\chi_{1111}^{(3)})cos(\theta_1)sin(\theta_1) + 2Re(\chi_{1112}^{(3)*}\chi_{1111}^{(3)})cos(-\theta_1)sin(-\theta_1) \quad (1.35)$$

$$= 2Re(\chi_{1112}^{(3)*}\chi_{1111}^{(3)})sin(2\theta_1). \quad (1.36)$$

From Eq. 1.36 it is apparent that the CARS-ROA signal in the difference spectrum becomes larger as the offset angle θ_1 is increased and in theory, maximizes at 45°. However such large angles likely overwhelm the ROA signal due to the much larger achiral signal passing the polarizer, Hamaguchi and co-workers showed that angles of ca. 0.5° offer a good compromise.[81]

After evaluation of $Re(\chi_{1112}^{(3)*}\chi_{1111}^{(3)})$ the relationship of the heterodyne CARS signal with the CID of spontaneous ROA can be derived:

$$\triangle I_{CARS}^{transmitted}(\theta_1) = I_{CARS-ROA}(\theta_1) \sim sin(2\theta_1)A \cdot \Gamma \frac{\triangle(0°)\chi_{1111}^{(3),NR}}{2\hbar\left\{(\Omega - \omega_p + \omega_s)^2 + \Gamma^2\right\}} \quad (1.37)$$

$$A = 2a^2 + \frac{8\gamma^2}{45}. \quad (1.38)$$

Here Γ is the damping constant, a and γ are the linear isotropic and anisotropic rotational invariants and Ω is the resonance frequency. As $\chi_{1111}^{(3),NR}$ can be regarded as frequency-independent, this implies that heterodyne-detected CARS-ROA spectra acquired in the manner described should be NRB-free and exhibit the same spectral profile as those observed in spontaneous forward-scattering ROA.

Hamaguchi *et al.*, in their 2012 study on the chiral liquid β-pinene, demonstrated that the signal-to-noise ratio (SNR) could be enhanced by two orders of magnitude using the aforementioned technique compared to conventional ROA.[80] Their subsequent work in 2015 emphasized the significance of employing higher frequencies to improve the signal-to-noise ratio and contrast since $I_{CARS-ROA}(\theta) \sim \omega^5$.[81] The enhanced frequency sensitivity, compared to normal Raman signals (ω^4) is due to the additional linear relationship between the electric quadrupole and magnetic dipole moments and the ratio of the molecular structure size to the wavelength.[14] In addition, Hamaguchi *et al.* identified the presence of a systematic error in CARS-ROA from optical rotation dispersion. Optical rotation is a chiral linear effect in which polarized light rotates within a chiral medium, with the direction of rotation being opposite for each enantiomer. Different frequencies of light experience different degrees of rotation as they pass through a chiral medium, resulting in Optical Rotation Dispersion (ORD).

The dispersion of the optical rotation therefore leads to the divergence of the polarizations of all fields within the sample.[81, 15] This phenomenon can reintroduce the achiral signal $\chi^{(3)}_{1111}$ because the extinction angle of the analyzer is slightly altered for each wavenumber in the spectrum.

In the simple scenario of linear GVD in frequency, valid only for a small wavenumber range, and considering solely the GVD effect on the anti-Stokes field, the achiral signal would leak more towards the spectrum's edges with opposite signs in the CARS-ROA spectrum $\triangle I^{Transmitted}_{CARS}$. Ultimately, ORD produces a background to the CARS-ROA spectrum, which should become increasingly apparent when observing a wider range of wavenumbers. Since the Optical Rotatory Dispersion (ORD) is a linear effect, this artifact scales linearly with the thickness of samples. Thus, CARS-ROA samples should not exceed the maximum CARS interaction length in thickness.

Chapter 2

Experimental Setups and Methods

In the following section, the tunable fs-laser system employed to generate ultrashort pulses for both transient absorption and heterodyne CARS-ROA will be discussed. Subsequently, detailed descriptions of the setups, encompassing the optics for mani-pulating the ultrashort pulses, as well as the detection methods for both experiments are explained. Finally, in the last section, another tunable laser system exclusively utilized for generating tunable narrowband pulses in the UV resonance Raman Kerr gate experiments is outlined in conjunction with the Kerr gate Raman setup.

2.1 Tunable Femtosecond Laser System

For ultrafast time-resolved experiments such as transient absorption, the prerequisite is a minimum of two short laser pulses, typically below 100 femtoseconds, that are ideally also wavelength-tunable. This is here achieved through the utilization of optical parametric amplifiers (Orpheus-F, Light Conversion) with a noncollinear optical parametric amplifier (NOPA) stage. Efficient pumping of these OPAs is done using ca. 200 fs transform-limited pulses at 1030 nm from a Kerr-lens mode-locked YB:KGW laser (Pharos, Light Conversion). For an efficient OPA process first, a fraction of the pump laser light is focused into a sapphire crystal, thereby generating a white light pulse acting as the OPA seed. Additionally, through the second harmonic generation of the 1030 nm light, a more energetic 515 nm light is produced this conversion is necessary given that energy conservation dictates that the pump in an OPA must possess greater photon energy than the desired generated signal wavelength.

Subsequently, the slightly negative white light dispersion is compensated using a thin piece of glass thereby keeping the white light pulse as compressed as possible. This

white light pulse is then non-collinearly overlapped with the 515 nm pump pulse at a small angle ($\sim 8°$) in a thin BBO crystal. These details collectively contribute to the maximum spectral broadening of the OPA signal, a crucial aspect as spectral width and maximum achievable compression are interlinked by the Fourier transform limit.[82] The wavelength of the OPA signal is tunable from 650-900 nm by tilting the BBO crystal, thereby modifying the phase-matched frequencies.

Notably, the OPA idler in the first stage remains unused. The OPA signal pulse then proceeds to the second amplification stage, to which the majority of the pump light is directed. This stage operates collinearly, therefore the idler travels in the same direction as the signal and can be utilized if necessary (not used in this thesis). Post-OPA, the amplified signal pulse undergoes temporal compression by a prism compressor, achieving a pulse duration of approximately 50 fs. Lastly, one of these OPAs also features a second harmonic generation unit in order to generate pulses with wavelengths from 325-460 nm.

In the context of Coherent Anti-Stokes Raman Scattering, another OPA (OPA 3) optimized for a narrowband spectrum is needed whereas pulse compressibility is less important. In contrast to the other OPAs, spectral-broadening is minimized in this OPA by only making two small changes. Firstly, the white light seed undergoes temporal stretching by transmission through a 5 mm thick highly dispersive ZnSe crystal. Consequently, in the NOPA interaction, only specific frequencies of the white light synchronized with the pump are amplified. Moreover, the second amplification stage also employs a thicker OPA crystal, enhancing conversion efficiency and further avoiding spectral broadening. The output of this OPA will be roughly twice as narrow (see Fig. 2.2) as compared to the other two OPAs at a similar average power of 150 mW at 670 nm. This pulse will still need to be further spectrally filtered to achieve the spectral width typically needed for Raman spectroscopy. This is done by using a subsequent grating filter or an interference filter as utilized in this thesis (Alluxa: Ultra Narrow Bandpass Filter 667.7-0.5 OD6). The three OPAs are depicted in Figure 2.1, however, for clarity certain elements were omitted such as the delay stages for synchronization for each OPA stage, lenses used for optimizing fluences as well as optical filters for light separation.

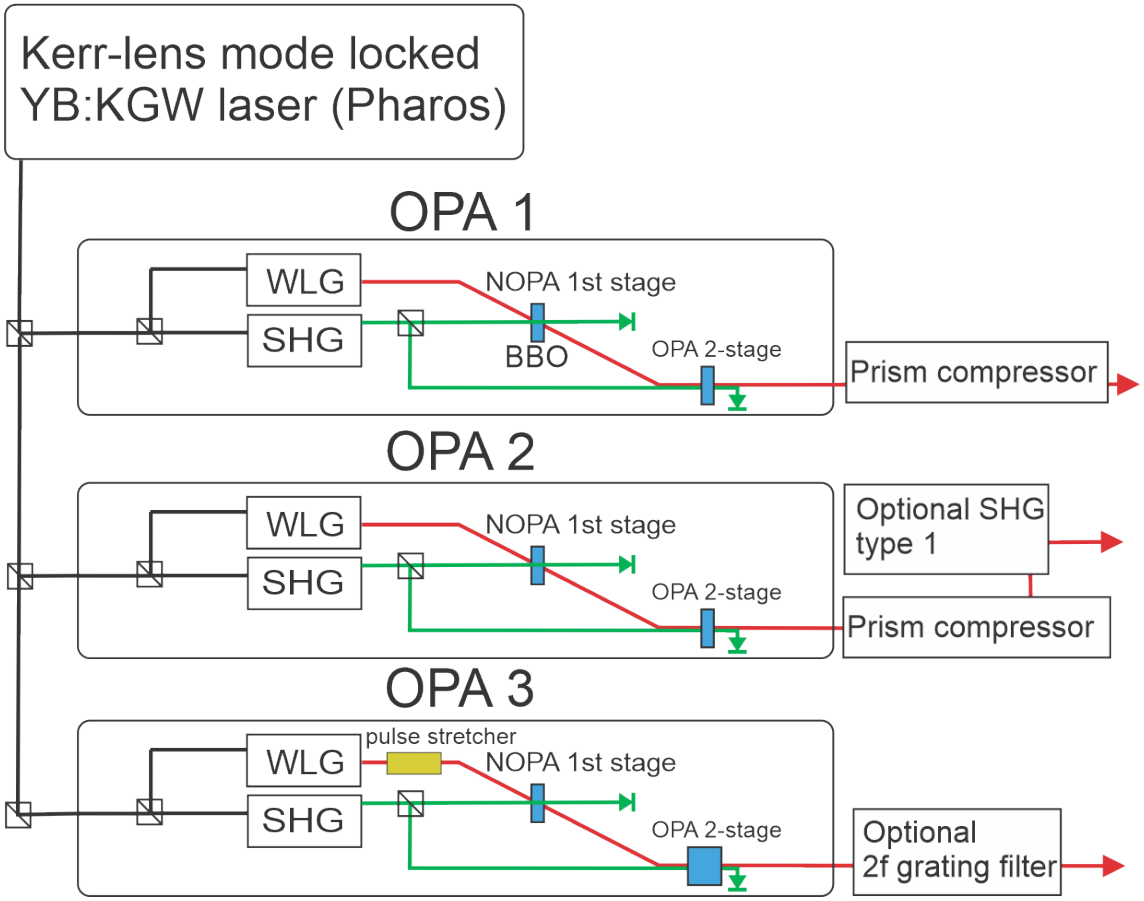

Figure 2.1: Simplified schematic of the short pulse setup with three tunable OPA laser sources. The upper pair of OPAs, in combination with prism compressors, is employed for short pulse generation (50-80 fs). Conversely, the lower OPA, used for CARS experiments, generates spectrally more narrow pulses.

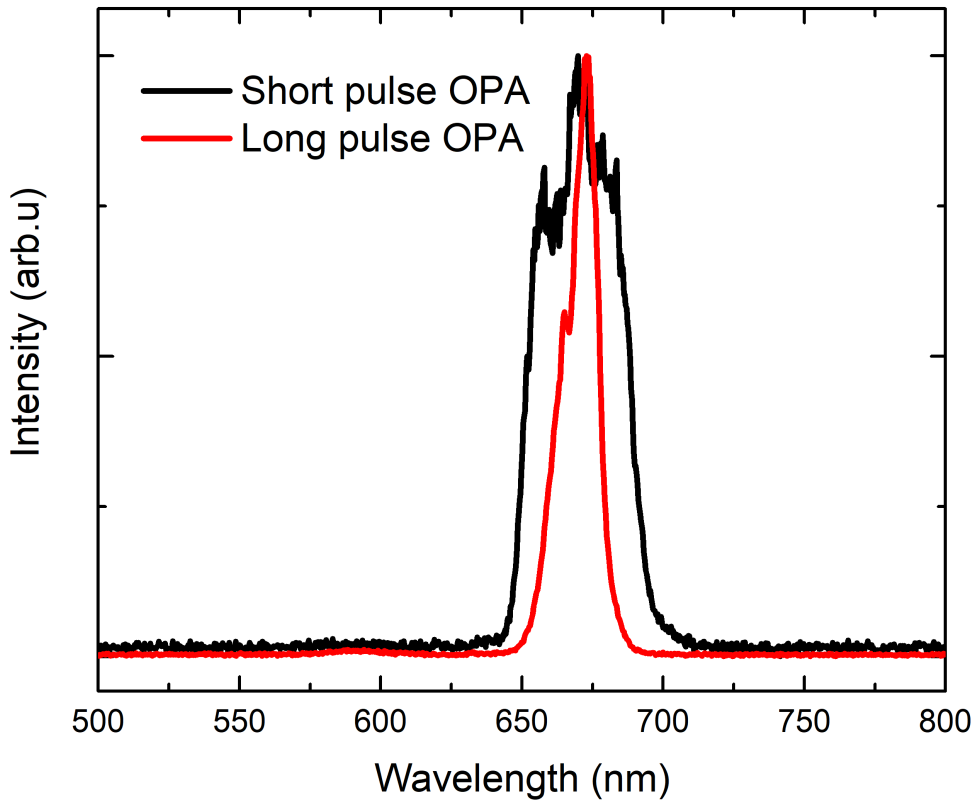

Figure 2.2: The two types of pulses which can be generated using the Orpheus-F NOPAs. The black curve represents the broadened spectrum at approximately 670 nm of the OPAs (OPA1 and OPA2) configured for a short pulse mode. In contrast, the red curve illustrates the narrower spectrum of OPA3 set to a wavelength of 670 nm.

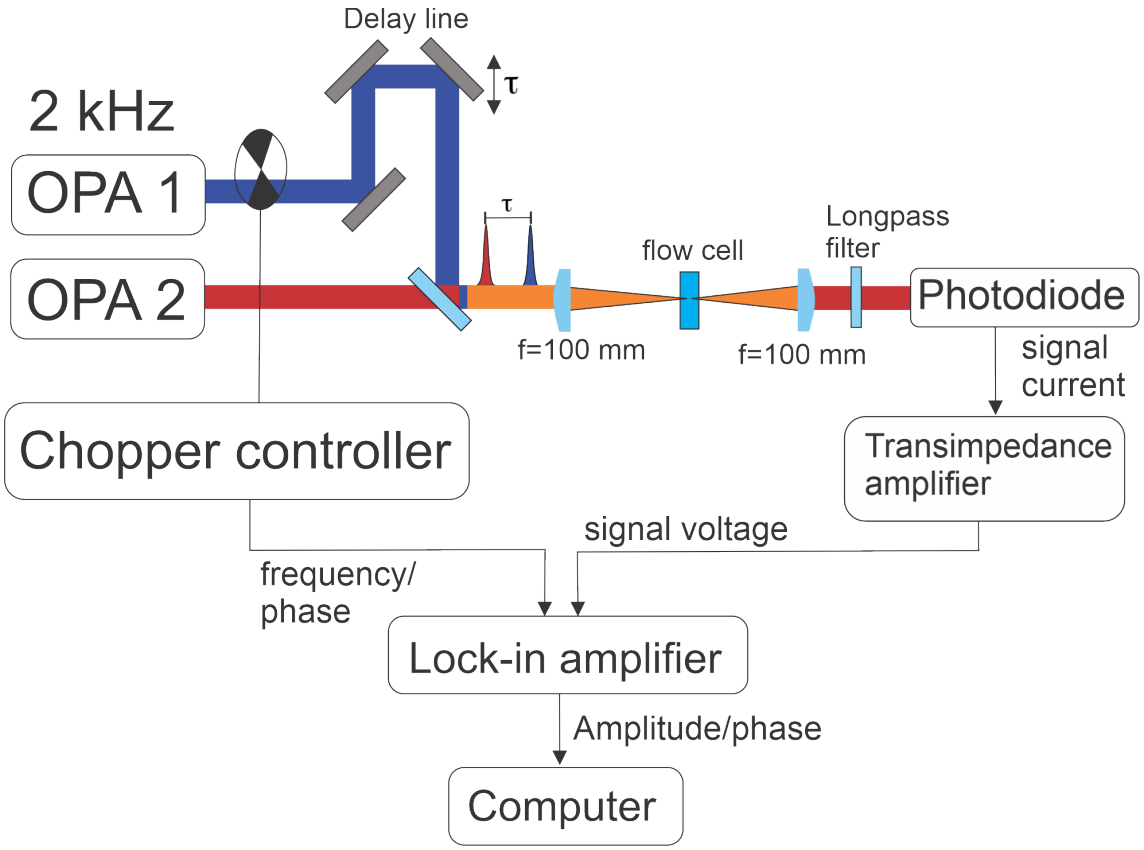

Figure 2.3: The optical setup for detecting narrowband transient absorption along with the electronic components for detecting the TA signal.

2.2 Transient Absorption of Arylazopyrazoles

Narrowband Transient Absorption

The transient absorption measurements employ pump and probe pulses generated by the two OPAs, OPA1 and OPA2, utilizing the tunable fs laser system described above. For the pump pulses the output of OPA1 is set to 860 nm and undergoes subsequent frequency doubling to 430 nm with a FWHM of approximately 10 nm and a pulse duration of ca. 70 femtoseconds. OPA2 for probe pulses is set to 650 nm with a FWHM of approximately 20 nm and a pulse duration ca. 60 fs. In a collinear configuration, both pump pulses (∼1 mW) and probe pulses (∼300 µW) are focused (focal length of 100 mm) and synchronized temporally and spatially into a flow cell with a 2 mm pathlength (see Figure 2.3). Following recollimation, the pump pulses are removed from the probe pulses using a long-pass filter. Finally, the probe pulses are detected by a silicon photodiode (Thorlabs PDA100A2).

The transient signal captured by the silicon photodiode is extracted using the modulation transfer technique. To accomplish this, the pump beam is modulated at 250 Hz

before reaching the sample, while the signal from the photodiode is amplified via a trans-impedance amplifier, and is passed onto a lock-in amplifier (Zürich Instruments UHFLI 600 MHz). The phase origin of the lock-in amplifier is set to maximize the modulated signal which has an approximately 180° phase difference to the pump modulation. The lock-in amplifier outputs both the modulated signal and total signal which are divided according to Eq. 1.3 to yield the TA signal.

Two different light sources were employed for the experiments on the photoisomerization dynamics of AAPs. Every AAP was dissolved in water to produce a 5 mM solution. Three 365 nm UV LEDs facilitate the conversion from $E \rightarrow Z$, while green LEDs emitting at 530 nm enable $Z \rightarrow E$ photoswitching. Each LED set has a total output power of 3 W. During the TA measurements, the sample is continuously circulated through the flow cuvette with a peristaltic pump. In order to obtain the photostationary state composition either rich in E or Z-isomers, the UV or green LEDs irradiate the reservoir (approximately 200 ml) from the flow system for one hour prior to and continuously for the duration of the measurement. Following every measurement, the sample is exchanged to minimize the potential impact of photodegradation.

Data processing for transient absorption data is done using the "lsqcurvefit" toolbox in MATLAB. In the case of E-isomers, fitting is conducted over a pump-probe delay range that corresponds to -0.7 to 10 ps employing a fit function with two exponentials convolved with a Gaussian function. For Z-isomers, fitting is conducted within the range of -0.7 to 5 ps utilizing a single exponential function convolved with a Gaussian function. Additionally, for each isomer, a rising exponential function (step function) is incorporated to model photoproduct formation.

Broadband Transient Absorption

To implement the TA broadband detection method, the OPA probe pulse needs only to be exchanged with a white light pulse. To produce such a pulse the 1030 nm Pharos output was focused into a 5 mm thick sapphire crystal. Subsequently, the white light probe was directed into a spectrometer, where it underwent spectral dispersion and arrived on a specialized detector.

In broadband TA choosing the optimal detector is a challenge. In narrowband TA, lock-in detection provides an elegant solution to obtain a very high SNR and is particularly useful for high-frequency modulation. However, implementing an array of photodiodes connected to separate lock-in amplifiers is costly and technically challenging.[83] In contrast, array detectors such as CCDs are composed of pixels with potential wells. They integrate electrons produced at the photodiode (integrating photodiodes), to increase photocurrents

during readout. These signals, like in lock-in detection, must be amplified. The active pixel sensor directly amplifies the pixel photocurrent at each pixel using transistor circuits. Common amplification circuits in photodiode arrays are Complementary Metal-Oxide-Semiconductor (CMOS) and N-type Metal-Oxide-Semiconductor (NMOS), both utilizing MOSFET transistors.

Due to the large signal of the probe pulses the signal-to-noise ratio will in part be determined by shot noise as opposed to readout and dark noise. Shot noise is proportional to the square root of photon events in a single measurement.[84] Hence, the saturation well-capacity, or the amount of charges each pixel can store, should be large. For the photodiode component, a large well capacity is expressed in its pixel area as it will be approximately proportional to charge storage capacity. Consequently, shot noise is reduced for large single-line detectors.

Another crucial consideration is how quickly the read-out frequency for an entire row of pixels is. Ideally, this readout frequency should be at the laser's repetition rate which allows for shot-to-shot detection.[85] This, in turn, enhances the signal-to-noise ratio significantly because the large laser fluctuations of white light can be effectively removed.

For the broad-spectrum Transient Absorption (TA) experiments, the already available NMOS S8380-512Q was used. This particular model boasts a huge well capacity of 312 million electrons and a readout frequency per-line of up to 4 kHz. Via the driver from KHS instruments, the detector records the average signal from four successive readouts, which are synchronized with the optical chopper by feeding the integration timing signal into the chopper controller. The driver was initially intended for FSRS, which requires four readouts using two optical choppers rather than only two, therefore two readouts were averaged for the division. One notable drawback of this detector lies in its rolling shutter, where pixels are read sequentially, as opposed to a parallel (global) shutter. Consequently, the pulse signal of the laser pulses exceeds the readout per line duration, resulting in not all pixels capturing the probe laser pulse for each measurement.

2.3 Heterodyne CARS-ROA

For CARS-ROA, the tunable fs laser setup is sketched in Fig. 2.4 and was configured to the maximum repetition rate of 20 kHz, since no flow system was required for the experiment. OPA 3 was employed to generate the necessary narrowband Raman pump pulse for CARS, in combination with one of the short-pulse optimized OPAs (OPA 2) to generate the Stokes pulse. The output of OPA 3 was further spectrally filtered, from an initial full width at half maximum (FWHM) of 17.8 nm to approximately 0.5 nm, utilizing

a 667.7 nm single-cavity filter (Alluxa). This results in a maximum spectral resolution of ca. 12 cm^{-1}. Afterward, the pump and Stokes pulses were merged and collimated using a dichroic mirror. Subsequently, the pulses passed through two achromatic lenses (f=10 mm), with two glan Taylor polarizers (GTP1 and GTP2: B. Halle Nachfl. GmbH, extinction ratio $<10^8$, angular acceptance range <5 arcmin) placed in between. The first polarizer orientation is fixed at a roughly parallel position to the pulse polarizations (vertical), the second polarizer (analyzer) GTP2 is roughly oriented horizontally and its rotation can be fine-tuned using a motorized rotation stage (Standa Ltd. 8MPR16-1, step resolution $\sim 0.01°$). Upon the pulses reaching the focal point between the polarizers, the sample placed inside a cuvette (Hellma 1 mm and 2 mm) is positioned, here the pulses are spatially and temporally synchronized. After the newly generated CARS pulse is recollimated by lens L2 the pump and Stokes pulses are spectrally filtered out using an interference filter. Subsequently the remaining CARS pulse is focused on the slit of a spectrometer (HORIBA Scientific; iHR320) using a lens. The CARS signal is finally detected on a liquid nitrogen-cooled CCD (HORIBA Symphony II). In the next paragraph the measurement procedure for obtaining a CARS-ROA spectrum is detailed.

The first step of the measurement procedure involves determining the analyzer orientation that minimizes the CARS signal passing through the polarizers (extinction angle). This position, roughly perpendicular to the input beam polarizer, includes the optical rotation (OR) from passing the chiral sample between the polarizers. For a 2 mm thick cuvette filled with β-pinene(-) and β-pinene(+) , the OR was $\pm 0.32°$ from the perpendicular position of the analyzer. Due to the low signal transmission through the polarizers, the extinction angle is difficult to determine with precision below 0.1°. Therefore, the initial best guess for the extinction angle is defined as zero ($\theta = 0$).

Once the extinction angle is roughly located, the polarizer is turned back a few degrees and then turned clockwise to the desired $-\theta_1$ position. It is crucial to rotate the polarizer only in the clockwise direction to avoid backlash introduced by the gear system of the polarizer stage when the rotation is reversed. At the desired $-\theta_1$ position, a spectrum of the signal with a short integration time of ca. one second is saved in the software. The polarizer is then moved unidirectionally with 0.01° steps towards $+\theta_1$ while viewing the live CARS difference-spectrum from $-\theta_1$ and the current position. As soon as the spectra largely cancel out (often CARS-ROA peaks can already be seen at this point), the precisely determined effective mirror position $+\theta_1^{eff} \approx +\theta_1$) is noted. The measurements with both noted angles $-\theta_1$ and $+\theta_1^{eff}$ are then repeated with longer integrations times by first overrotating the polarizer 3° degrees counterclockwise to compensate for backlash. Finally, both spectra are subtracted to generate the heterodyne CARS-ROA spectrum.

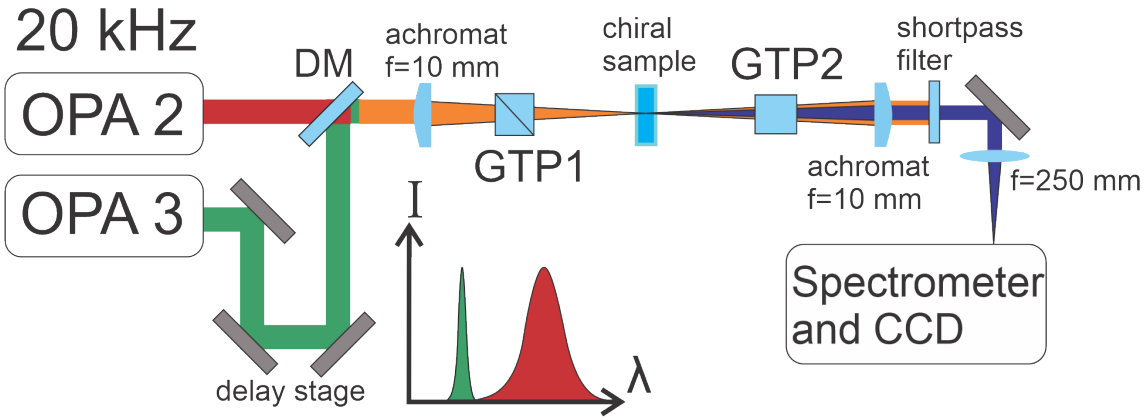

Figure 2.4: The optical layout to detect heterodyne CARS-ROA spectra. The Raman pump (green) and Stokes (red) beams are merged via a dichroic mirror (DM). Both the input beams are polarized in parallel. In the chiral sample, the CARS beam is generated and depicted in blue.

The compounds initially investigated using the heterodyne CARS-ROA technique were the two enantiomers of liquid β-pinene, acquired from Merck KGaA, Germany, in spectroscopic grade. The second group of compounds under investigation consisted of the solids (*R*)- and (*S*)-MOM-BINOL, dissolved in DCM. The synthesis of the MOM-BINOLs was carried out from BINOL by Niemeyer and co-workers (procedure outlined in [86]).

2.4 Kerr-gated UV Resonance Spectroscopy

2.4.1 Tunable Narrowband Picosecond Laser System

The laser pulse source used in the Kerr gate experiment to investigate anthracene is characterized by its tunable narrowband transform-limited pulses. Diverging from the fs-pulse configuration described above, this setup is designed to produce such pulses with high conversion efficiency and without subsequent spectral filtering. Refer to Figure 2.5 for a simplified schematic, akin to the initial depiction in the setup's introduction in [87]. The Pharos pump laser is (nearly) the same as in the fs-setup, emitting picosecond pulses at 1030 nm with a total output power of 6 W and a repetition rate of 10 kHz. However unlike in the short pulse arrangement, the output power is evenly split into a 3 W uncompressed part and a 3 W compressed part, the latter passing through an internal grating compressor. Utilizing an SHBC, the uncompressed Pharos output undergoes frequency doubling and efficient spectral compression to less than 10 cm^{-1}. This frequency-compressed beam serves to generate frequency-tunable, particularly spectrally narrow outputs through an optical parametric amplifier (OPA).

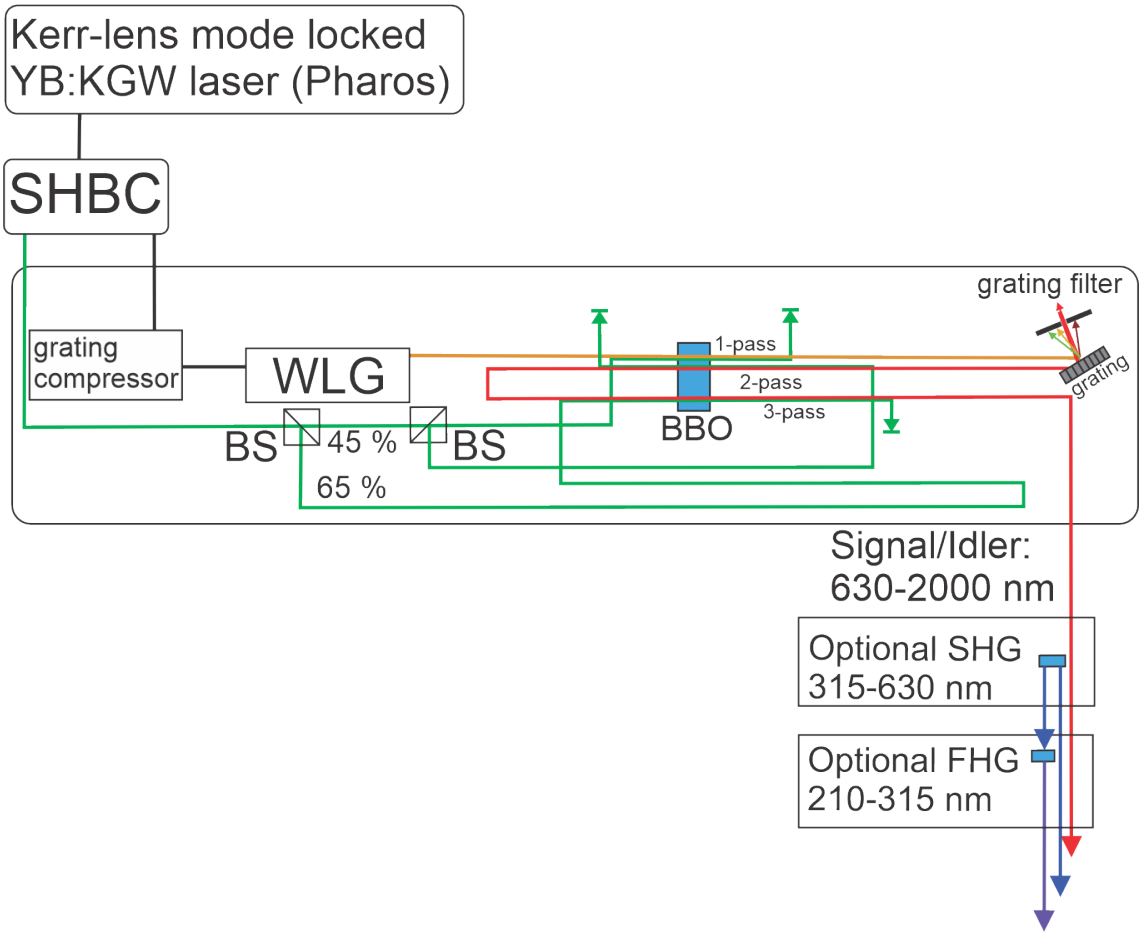

Figure 2.5: Simplified schematic of the narrowband ps-pulse setup capable of generating tunable and spectrally narrow pulses deep in the UV.

In contrast to the OPAs in the short pulse setup, the OPA in this case (Orpheus ps, Light Conversion) is designed differently. The SHBC-generated pump is initially spectrally narrow, but the interaction with the required spectrally broad white light seed leads to spectral broadening of the OPA signal. To regain a spectrally narrow OPA output, a 2f grating filter is employed after the first white-light seeded OPA interaction inside a BBO crystal (second pass). After these two initial stages, the OPA signal is then further amplified by a third amplification stage (third pass) which utilizes the majority (∼65%) of the pump light.

To prevent spectral broadening and ease alignment, a single 10 mm thick BBO crystal is used. Each stage features a single-mirror delay stage (not shown). In accordance with energy conservation, the maximum generatable frequency of the OPA signal or idler is limited to that of the pump frequency. Therefore, in order to access higher energy frequencies particularly in the blue and UV, one or two consecutive stages of second harmonic generation (SHG) are used. By this method, pulses can be generated between 210 to 1000 nm with a spectral bandwidth less than 20 cm^{-1} with a pulse duration of less than 3 ps.

As an example the spectrum at 376.2 nm derived from SHG of the OPA signal at 752.4 nm is shown in Fig. 2.6. The FWHM at 376.2 nm is approximately 0.2 nm (14 cm^{-1}), corresponding to roughly twice the spectral width of the OPA signal, yielding a transform-limited pulse duration of 2.3 ps.

2.4.2 UV Resonance Raman Kerr Gate Setup

To compare resonance Raman spectra at ^1L_a resonance with those done using conventional UVRR excitation near 250 nm, anthracene was dissolved in acetonitrile.[69] Acetonitrile was chosen as a solvent owing to its minimal Raman bands in the fingerprint region, thereby minimizing interference with those originating from anthracene. Anthracene, purchased from Sigma Aldrich, was dissolved to produce 2 L of a 1.3 mM or 15 mM solution. This solution was introduced into a flow-system reservoir. The flow system was necessary to reduce the accumulation of light-induced anthracene-dimer photoproducts. A flow cuvette with dimensions of 10x4 mm was employed for the flow system. The sample within the cuvette undergoes cycling via a peristaltic pump and includes a 2 L reservoir (boiling flask). The Kerr gate setup, illustrated in Figure 2.7, utilized a UV Raman probe beam provided by the narrowband pulse setup (described in the above paragraph).

Lens L1 focuses the Raman excitation beam into the flow cell which is positioned in such a way that the beam passes the cuvette's edge to minimize reabsorption effects. For

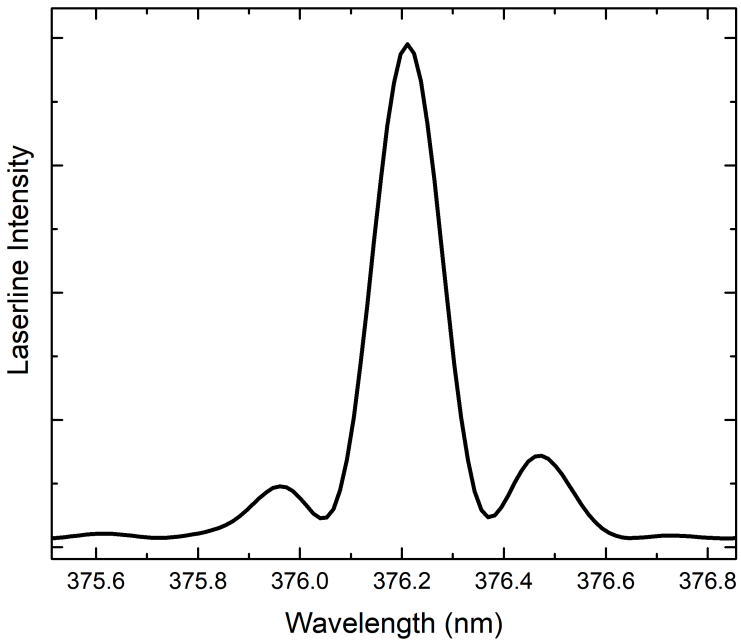

Figure 2.6: Example for a spectral output of the tunable narrowband picosecond laser system at 376.2 nm. There are notably distinctive sidebands resulting from the *sinc* phase matching condition during the frequency-conversion processes by the nonlinear crystals.

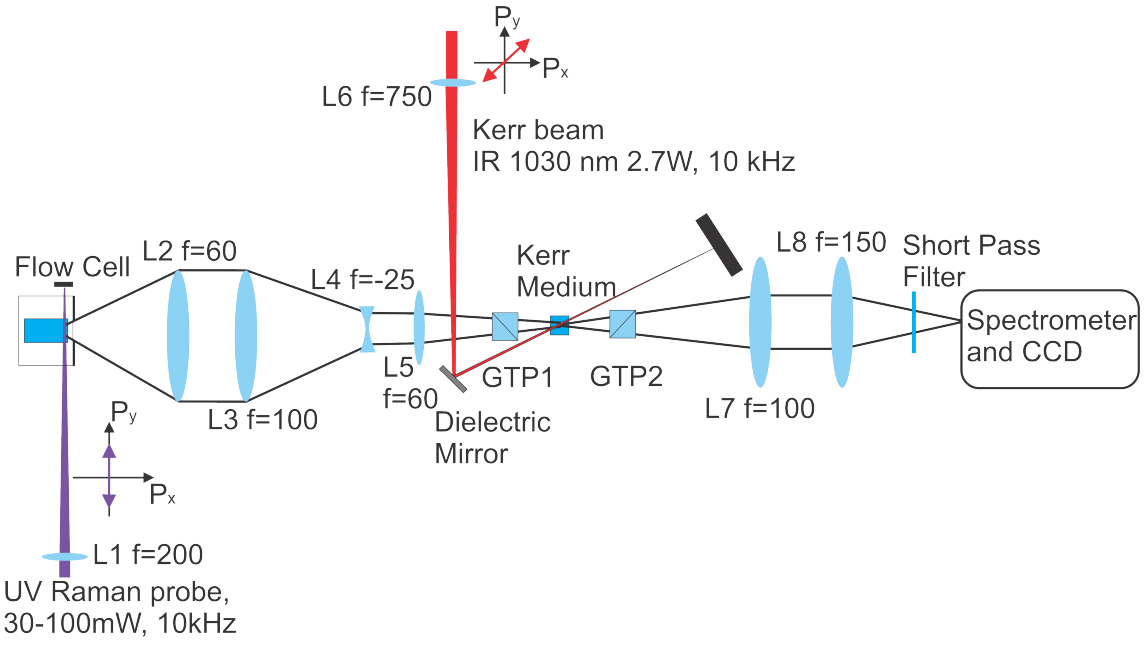

Figure 2.7: The UV Kerr gate setup: The UV Raman excitation beam is shown in purple and the Kerr beam in red. Raman scattered light is guided towards the Kerr medium using a collecting lens (L2), a telescope (L3 and L4), and a focusing lens (L5). This light then traverses two Glan Taylor polarizers, where it intersects with the Kerr beam (at a 45° linear polarization angle). Finally, the light is directed towards the spectrometer and CCD.

collection scattered light emitted from the cuvette was gathered at a 90° angle using a 2-inch lens (L2). A telescope composed of L3 and L4 (1-inch diameter) reduced the light beam by a factor of five, compensating for the use of low aperture 10x10 mm cube Glan-Taylor polarizers (Thorlabs GT10). Additionally, the first Glan-Taylor polarizer GTP1 was positioned behind the focusing lens into the Kerr medium (L5). This arrangement, where the telescope is immediately followed by the focusing lens, aimed to reduce the effect of divergence due to beam-waist reduction.

As the laser traversed up to 4 mm of the sample, the scattered light converges into a line within the Kerr medium (benzene). This scattered light intersected at a crossing angle of ca. 15° with the high-power 1030 nm Kerr gate pump (ca. 2.7 W) focused by L6. Prior to lens L6, the pump light underwent polarization rotation using a half-wave plate, resulting in light that is polarized at a 45° angle compared to the vertically polarized UV Raman excitation. Lens L6 was mounted on an optical rail and placed at approximately 625 mm distance from the Kerr cell, optimizing fluence to a threshold before cavitation bubbles appeared inside the Kerr cell while maximizing the gated sample volume (spot size in Kerr cell ∼1 mm). The dielectric mirror (Thorlabs, BB1-E03) deflecting the focused Kerr gate beam towards the Kerr cell has minimal absorption (reflectance >99%), avoiding damage to the mirror from the high fluence beam. With GTP2 set perpendicular to GTP1, only the scattered light that overlaps with the Kerr beam inside the Kerr cell is in principle passed through GTP2. Furthermore, synchronization between the Kerr beam and scattered light was achieved using a retroreflecting delay stage (not shown).

The light passing through GTP2 traversed a collimating lens and a subsequent focusing lens that directed the light to the slit (slit width ca. 0.2 mm) of a grating spectrometer (SpectraPro.500i, Acton Research Corp.). To prevent interference from the strong Kerr gate beam, a short pass filter, transmitting UV light but rejecting the NIR 1030 nm pump light (Semrock, FF01-405/150-25), was additionally placed in front of the spectrometer. For taking measurements the spectometer features a UV-optimized back-thinned CCD camera (PyLoN 2KBUV, Princeton Instruments).

Operating the Kerr gate requires significant safety precautions, due to the very hazardous invisible Kerr gate pump. Unintended black reflections from transmissive optics frequently surpassed 100 mW. A proactive measure was the use of an IR viewer to identify and block stray light beams that escape the optical table when adding optical elements (see Fig. 2.8). Additionally, IR-blocking safety glasses (Thorlabs LG11) were consistently worn; the high transmission in the visible spectrum makes it easy to wear them continuously.

A MATLAB program was written to facilitate Kerr-gated Raman measurements, integrating control over the spectrometer, Kerr gate delay stage, and tunable narrowband

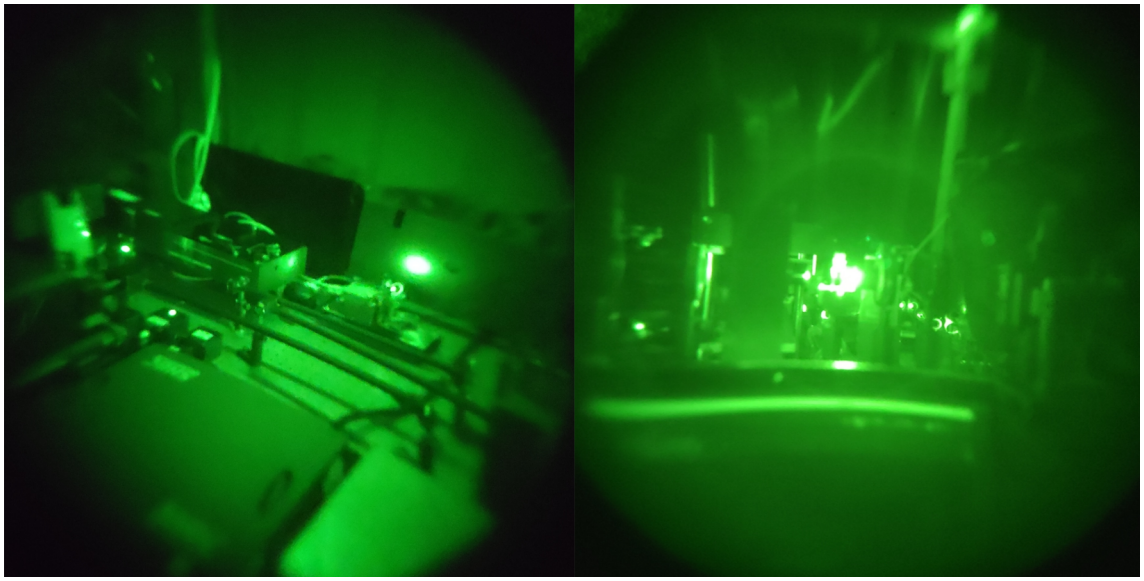

Figure 2.8: Pictures of scattered and back-reflected light from the IR beam were captured using an IR viewer. In the left image, a potentially hazardous back-reflection is depicted, but it is obstructed from exiting the table. The right image displays the reflection from the IR-Kerr beam onto the cuvette housing the Kerr medium.

picosecond laser system. The graphical user interface of this program is depicted in Fig. 2.9. Initially, the program synchronizes the Raman and Rayleigh scattered light with the Kerr pulse by setting the delay stage position. Subsequently, a spectrum is acquired near the excitation laser wavelength to precisely determine the excitation wavelength (λ_{exc}) using the spectrometer, which is crucial for accurate wavenumber determination. Following this step, the spectrometer is configured to the center of the Raman spectrum (at ca. 1400 cm^{-1}), and a Raman spectrum is obtained ($I(0\text{ ps})$). Upon completion, a second measurement (without Raman signal) is conducted with the delay stage set to a forward delay of $\Delta t = 3$ ps ($I(3\text{ ps})$). This measurement will be used as a reference to remove the remaining gated fluorescence in the spectrum at $I(0\text{ ps})$. In some cases, a third measurement is performed, during which a stepper motor is employed to block the Kerr beam to determine the leaked signal through the Kerr gate polarizers (I_{leak}). To immediately assess the Raman signal, the spectrum $\frac{I(0\text{ ps})-I_{leak}}{I(3\text{ ps})-I_{leak}}$ is calculated and displayed. Subsequently, all measurements are saved in a tab-delimited format as separate files.

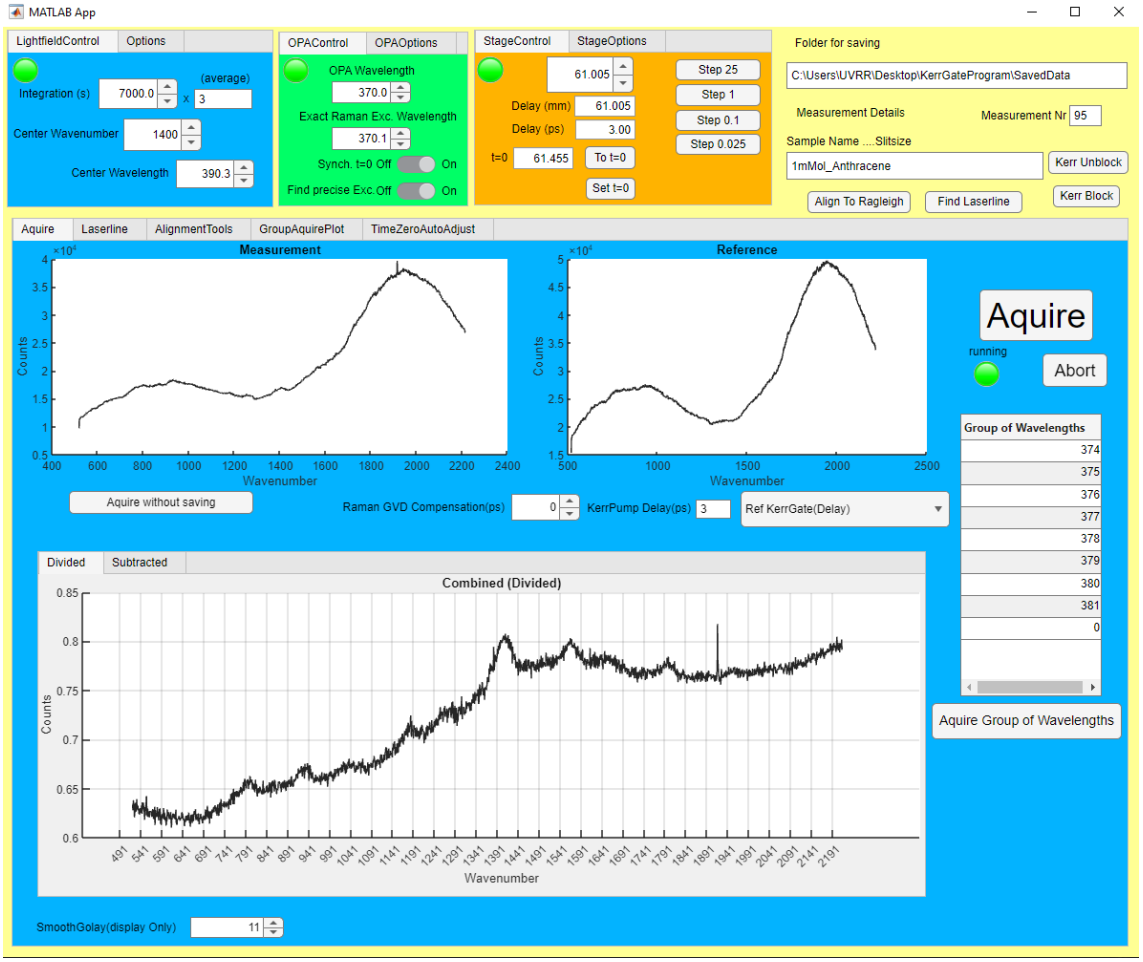

Figure 2.9: Graphical user interface (GUI) for Kerr-gated Raman measurements. The top section displays spectrometer controls in blue, laser controls in green, and delay stage controls in orange. In the bottom left corner, the Raman measurement at $\Delta t = 0$ ps is shown, while on the right, the measurement without Raman signal and only fluorescence at $\Delta t = 3$ ps is displayed. The resulting spectrum $\frac{I(0\text{ ps})-I_{leak}}{I(3\text{ ps})-I_{leak}}$ is calculated and shown at the bottom.

Chapter 3

Results and Discussion

3.1 Photoisomerization of Arylazopyrazoles

Narrowband femtosecond transient absorption (TA) measurements were carried out to explore the potential similarity in dynamics between planar arylazopyrazole (AAP) and azobenzene (AB). Additionally, it was aimed to examine any changes in dynamics resulting from an initial twist induced by ortho-substitution at the phenyl ring (AAP-3 and AAP-4). Most results of the study presented here have been published in reference [1].

As a first step, the optimal pump frequency for TA was determined. For this, the (ground state) absorption spectra of the AAPs are examined (refer to [5, 6] for the initial report of absorption spectra). Figure 3.1 showcases the ground state UV/Vis absorption spectra of AAP-1, AAP-2, AAP-3 and AAP-4 in water.

The displayed spectra include the absorption spectra of the AAPs before (shown in black) and after irradiation with 365 nm light (Z-rich PSS in magenta) and 520 nm light (E-rich PSS in green), respectively. All AAPs have an $n\pi^*$ absorption peak in between 400 and 440 nm. The Z-isomers have a larger oscillator strength for the $n\pi^*$ transition than the E-isomers. Likewise, all AAPs have $\pi\pi^*$ transitions which lie between 296 nm and 347 nm. Except for the twisted AAP-4, the transition of the E isomer is slightly blue shifted because of the extended π-conjugation for planar E-isomers. Additionally, E-isomers have a greater oscillator strength in the $\pi\pi^*$ transition.

For the representative compound AAP-1 the Z-enriched PSS absorption spectrum (magenta) features maxima at 312 nm corresponding to the $\pi\pi^*$ transition and at 440 nm related to the $n\pi^*$ transition. In the E-enriched PSS (green), the maximum of the $\pi\pi^*$ transition shifts from 311 nm to 347 nm and has a roughly 2.8 times greater oscillator strength. In contrast, its $n\pi^*$ transition oscillator strength at 400 nm is much weaker and

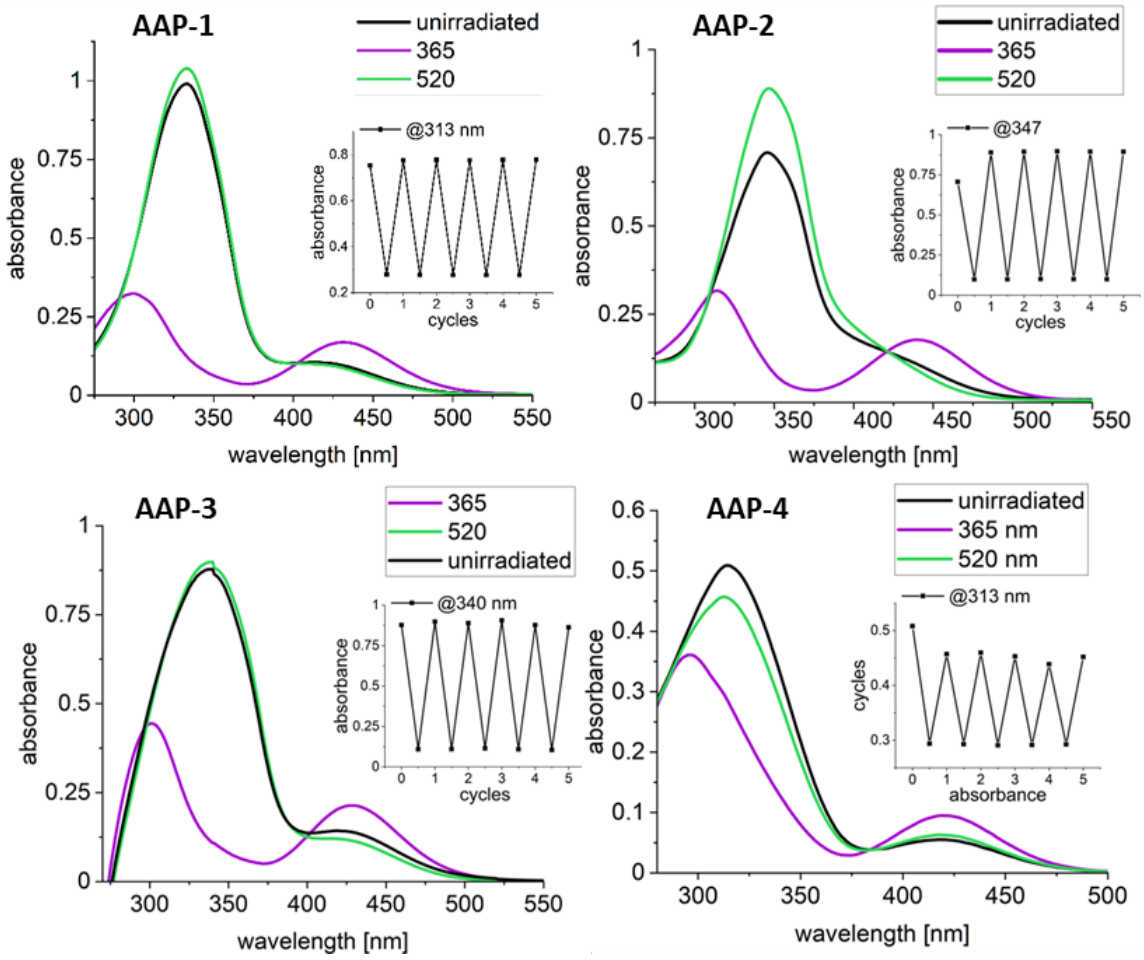

Figure 3.1: UV/Vis absorption spectra of the four AAPs at 50 µM concentration in water and a 12.5 mm absorption path length. The black curve represents unirradiated spectra. Additional spectra shown are after irradiation with 365 nm light (Z-rich) and 520 nm light (E-rich). The inset displays the stability of the AAPs under reversible photoswitching, as indicated by the absorption signal (figure/data produced by K. Ziegler).[1]

only noticeable as a shoulder in the spectrum.

The absorbance differences between the isomers at the $n\pi^*$transition are most marked in AAP-2 due to its electron donating group pulling the $n\pi^*$ transition apart spectrally by 40 nm (blue shift in the E-isomer, red shift in Z-isomer). This explains why AAP-2 has a particularly large backswitching PSS ($Z \rightarrow E$) and was considered one of the best AAP photoswitches for applications.[6] AAP-3 has a similar spectral separation in the $n\pi^*$ transition as AAP-1, however, oscillator strengths are more similar between the E-isomers which reduces its PSS. On the other hand, AAP-4 has practically no spectral separation in the $n\pi^*$ transition, making the difference in oscillator strength solely responsible for its photoswitching ability. All the AAPs are known to have excellent photoswitching reversibility, which is indicated for 6 switching cycles by the insets in each plot.[6] The

metastability of the Z-isomer does not require consideration in this study, since all AAPs exhibit half-lives spanning from days to months.[6]

To experimentally test the hypothesis that twisted E-isomers of AAP-3 (energy minimum at 5 degrees twist) and to a larger extent AAP4 (energy minimum at 28° degree twist) have faster photoisomerization dynamics in comparison to the planar E-isomers AAP-1 and AAP-2, their relaxation lifetimes were measured using transient absorption spectroscopy.

This involved populating the $S_1(n\pi^*)$ state and selectively probing the ESA. The reason for populating the $S_1(n\pi^*)$ excited state instead of the $S_2(\pi\pi^*)$ excited state was to reduce complexity in kinetics and literature findings on the closely associated AB, showing that the main isomerization movement primarily occurs on the $n\pi^*$energy surface in both excitations.[88]

Given the corresponding absorption maxima for the $n\pi^*$ transition in the 400-450 nm range for all four AAP derivatives, 430 nm was chosen as a suitable compromise for the pump wavelength.

It should be pointed out that the $n\pi^*$excitation may seem to favor Z-dynamics since the Z-isomer possesses a greater ground state oscillator strength. From the literature of ABs, it is however expected that the larger E-isomer $n\pi^*$ excited state absorption oscillator strength should compensate for the TA signal magnitude for both isomers in AAPs.[89]

A drawback of opting for narrowband TA is that, unlike in broadband TA, pre-knowledge of the ESA absorption maximum is required to select the appropriate probe wavelength. Selecting the probe wavelength at the ESA maximum enhances the TA signal, thereby improving the signal-to-noise ratio (SNR). As a comparison, for AB, the ESA state in the visible is accessible in a broad range of 500-690 nm, with a resonance maximum at 530 nm for E-AB as well as at 540 nm for Z-AB.[89] Broadband TA measurements on AAPs were conducted for compound AAP-2 that has the highest PSS and displays a comparatively red-shifted broad ESA maximum centered at 575 nm (see Fig. 3.12). As the probe wavelength 650 nm was selected because it provided adequate ESA absorption for a good signal-to-noise ratio (SNR) while simultaneously the wavelength is well off-resonant with the $n\pi^*$ absorption peak. This minimizes other potentially interfering processes including photoproduct absorption (PA), ground state bleach (GSB), and hot ground state absorption (HGSA).[89, 33] Interestingly, time-dependent density-functional theory (TDDFT) calculations by Marcus Böckmann and Nikos Doltsinis showed that the ESA signal observed at this wavelength can be attributed to the $S_1 \rightarrow S_5$ transition (see SI in [1]).

It is important to emphasize that while Ground State Bleaching (GSB) could potentially serve to monitor dynamics in the excited state, the emergence of new products following

pump excitation would result in a significantly higher signal from product absorption. The greater the magnitude of these additional signals, the more difficult the observation of the initial dynamics becomes.

For the initial dynamics two dominant time constants are anticipated for ultrafast photoisomerization of E-isomers ($\tau_1 < 1$ ps and $\tau_2 > 1$ ps), similar to ABs ($\tau_1 \approx 300$ fs, $\tau_2 \approx 2 - 3$ ps).[32, 27, 90] It is widely agreed upon in literature that τ_1 represents the initial rapid movement departing from the Franck-Condon region towards a conical intersection.[33, 32, 90, 91, 92] The assignment of the second decay component in ABs remains a matter of debate. Several studies attribute τ_2 to the movement from the conical intersection back to the ground state potential energy surface.[27, 90, 91, 92] Other studies assign τ_2 to the relaxation from a dark E-isomer intermediate on the $S_1(n\pi^*)$ potential energy surface.[89, 93, 94, 95] In either case, it can be said that τ_2 sets a lower limit for the time constant of completed photoisomerization. The dynamics of Z-isomers under $n\pi^*$ excitation are expected to exhibit a nearly monoexponential decay.[32]

Since the selected AAP variants lack isomerically pure photo-stationary states, the signals, observed when samples are irradiated with UV light (for Z-rich) and green light (for E-rich), represent a linear combination of both E and Z contributions. For this reason, accurate values for the photostationary states of all AAPs are needed. The PSS was measured for all samples using ^{1}H-NMR spectroscopy. The determined values were similar to those of the initial report by Ravoo and co-workers. However, AAP-2 notably exhibited a slightly poorer PSS than the reported $\geq 98\%$ for both forward and backward switching (see table 3.1).[6]

Table 3.1: Photostationary states for all four AAPs in both switching directions with 365 nm ($E \rightarrow Z$) and 520 nm ($Z \rightarrow E$) irradiation.

	$PSS_{E\rightarrow Z}$	$PSS_{Z\rightarrow E}$
AAP-1	92 %	89 %
AAP-2	96 %	95 %
AAP-3	93 %	80 %
AAP-4	72 %	67 %

Using these PSS values and the TA signal A(t) of E- and Z-rich samples allows the extraction of the isomerically pure transient signals through the following system of linear equations:

$$A_{E-Rich}(t) = PSS_E \cdot A_E(t) + (1 - PSS_E) \cdot A_Z(t) \tag{3.1}$$

$$A_{Z-Rich}(t) = PSS_Z \cdot A_Z(t) + (1 - PSS_Z) \cdot A_E(t) \tag{3.2}$$

$$\Rightarrow A_{(E,Z)}(t) = \frac{A_{(E,Z)-Rich}(t) \cdot PSS_{(Z,E)} + (PSS_{(E,Z)} - 1) \cdot A_{(Z,E)-Rich}(t)}{PSS_{(E,Z)} + PSS_{(Z,E)} - 1} \tag{3.3}$$

Before initiating the TA experiments, a series of tests were carried out to confirm the required flow rate within the flow cuvette and to determine the maximum repetition rate that can be utilized to ensure little impact of the pump pulses on the PSS of the sample. If the same volume of the sample is already irradiated by a previous pump pulse, the PSS will be disturbed and Eq. 3.3 can not be used. The repetition rate and the speed of the peristaltic pump are important, as a lower repetition rate grants the flowing sample more time to exit the irradiated region. For instance, at a repetition rate of 20 kHz, the pump and probe pulses strike the sample every 50 µs. Conversely, at 2 kHz, the flowing sample has 500 µs to translate. Assuming a nearly Gaussian laser beam, one can estimate the pumped focal spot size at the sample using known quantities such as the input beam diameter (ca. 4 mm), wavelength (ca. 430 nm), focal length of the lens (100 mm), and beam quality factor of the Pharos laser system (ca. 1.3). This yields a $1/e^2$ spot size of ca. 20 µm, representing the minimum distance the flow must traverse from shot to shot. Hence, for a repetition rate of 20 kHz, the flow rate must be higher than 40 cm/s. Yet, attaining such flow velocity appeared improbable upon reviewing slow-motion smartphone footage capturing bubbles moving within the flow cuvette (bubble speed estimated at 20 cm/s).

In Fig. 3.2, the TA signal of *E*-AAP-1 in water is shown with variations in flow rate and repetition rate. As depicted in the top figure, at 20 kHz, the pump flow rate notably influences the signal, causing an offset when the probe pulse arrives before the pump (t<0). However, even at maximum pumping speed, this signal never actually reaches zero, indicating that preceding pump pulses continue to overlap, affecting both the TA signal and the PSS. The bottom figure illustrates that by subsequently reducing the repetition rate to 2 kHz, the TA signal for t<0 does approach zero. Furthermore, by decreasing the repetition rate to 0.2 kHz, no discernible signal change is observed. Hence, it is found that maintaining a maximum pump rate from the peristaltic pump, coupled with a repetition rate reduced from 20 to 2 kHz, is sufficient to ensure the translation of the previously pumped volume. The higher repetition rate, between 2 kHz and 0.2 kHz, is evidently beneficial since it allows for more pump-probe interactions to be averaged and therefore improves the SNR.

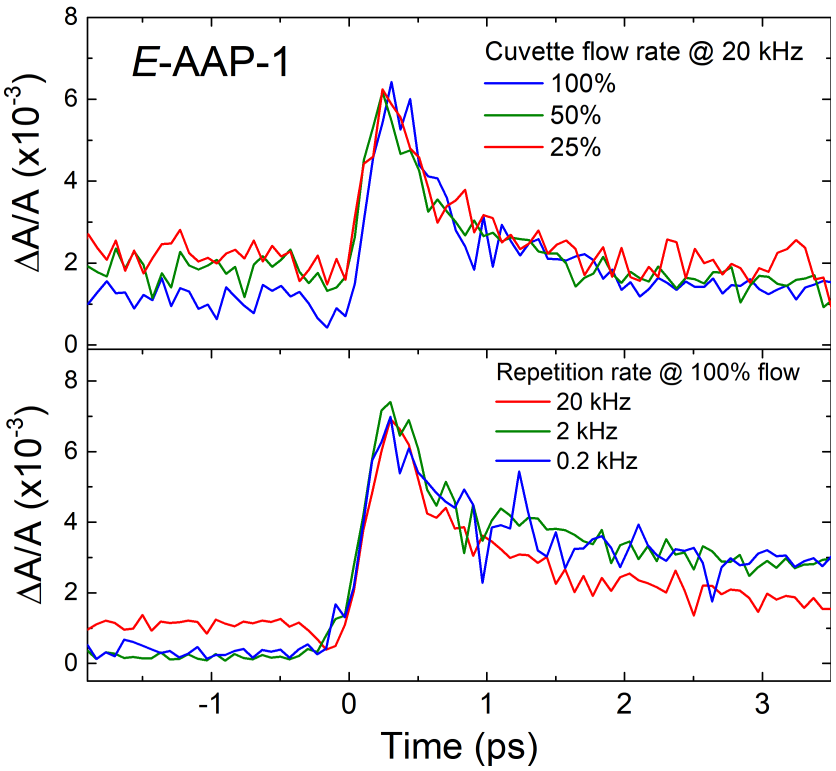

Figure 3.2: Experimenting with optimal flow rate and repetition rate configurations using the transient absorption signal of *E*-AAP-1 (pump wavelength λ_{pump}=430 nm, probe wavelength λ_{probe}=650 nm, and concentration c=5 mM): The upper curve illustrates the signals while adjusting flow-rate settings, achieved by increasing the peristaltic pump speed at a 20 kHz repetition rate. In the lower graph, the pump speed is set at 100%, while the laser repetition rate is altered.

Before measuring the TA signal of AAPs, another crucial step is to measure the signal originating from the water solvent combined with the glass windows of the flow cuvettes (fused silica). Although water and fused silica are in principle transparent for the wavelengths used, the materials are present in high concentrations. The high concentration in combination with the substantial fluences of the pump and probe pulses leads to nonlinear effects known as coherent artifacts. The most important effect is cross-phase modulation (XPM), wherein the pump generates an alternating refractive index in the sample through the optical Kerr effect, leading to alternating shifts in the phase of the probe light. This amounts to the redistribution of frequencies from the probe spectrum.[96] Usually, when the forward edge of the pump pulse coincides with the probe pulse, the probe spectrum experiences a red shift owing to the rising intensity gradient. Conversely, when the trailing part of the pump pulse overlaps, it causes a blue shift. For XPM in principle, the total energy of the photons remains constant, but there will be alterations in the frequency of these photons that the photodiode, as well as any preceding transmissive elements they encounter, are sensitive to. This may lead to both positive and negative signals at the

photodiode, even when no spectral dispersion occurs at the detector. The signal detected from water and the cuvette glass is depicted in Fig. 3.3; this signal was subsequently subtracted from the TA signal of the AAPs.

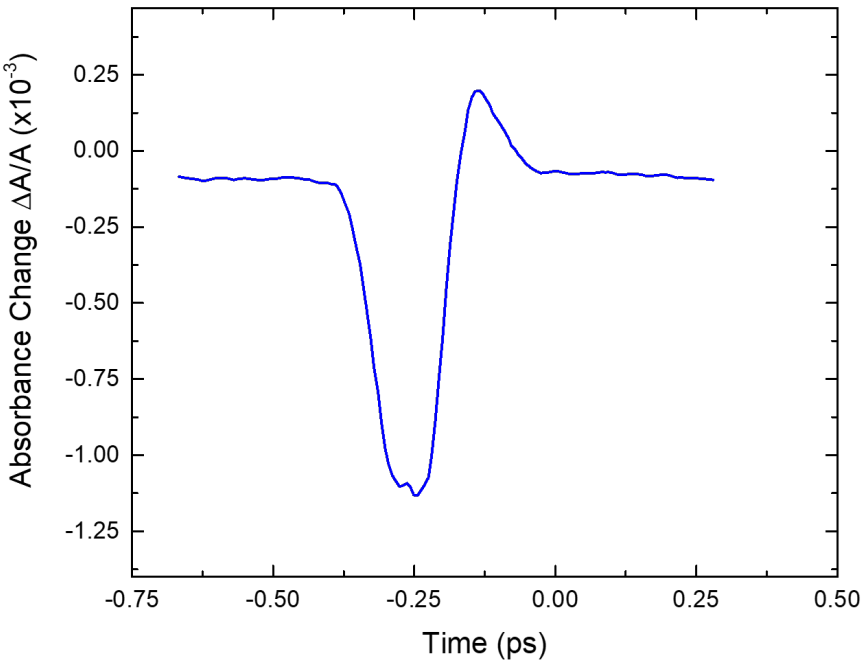

Figure 3.3: The pump-probe signal from water and the flow cuvette glass windows (pump wavelength λ_{pump}=430 nm, probe wavelength λ_{probe}=650 nm) which exhibits a negative cross-phase modulation signal before $\Delta t = 0$.[1]

After this preliminary work, the TA kinetic traces were taken for both E and Z rich mixtures and the PSS corrected signal was determined using equation 3.3. The TA signal for the Z-isomers is plotted in Fig. 3.4 which are for visual comparison, normalized from 0 ps and 1.5 ps.

The signal was then fitted with a monoexponential convolved by a Gaussian function representing the instrumental response function (IRF) of the pulse (see Fig. 3.5).

The extracted Z-AAP time constants are shown in the left side of Table 3.2 and all AAP time constants resemble those of Z-ABs (approx. 100 fs).[89, 32, 27, 90] The twisted Z-AAP-3 and Z-AAP-4 exhibit a seemingly faster switching speed compared to the planar Z-AAP-1 and Z-AAP-2. However, it is important to note that all AAPs except Z-AAP-2 have time constants approaching the instrument response function (IRF) limit, estimated at approximately 70 fs.

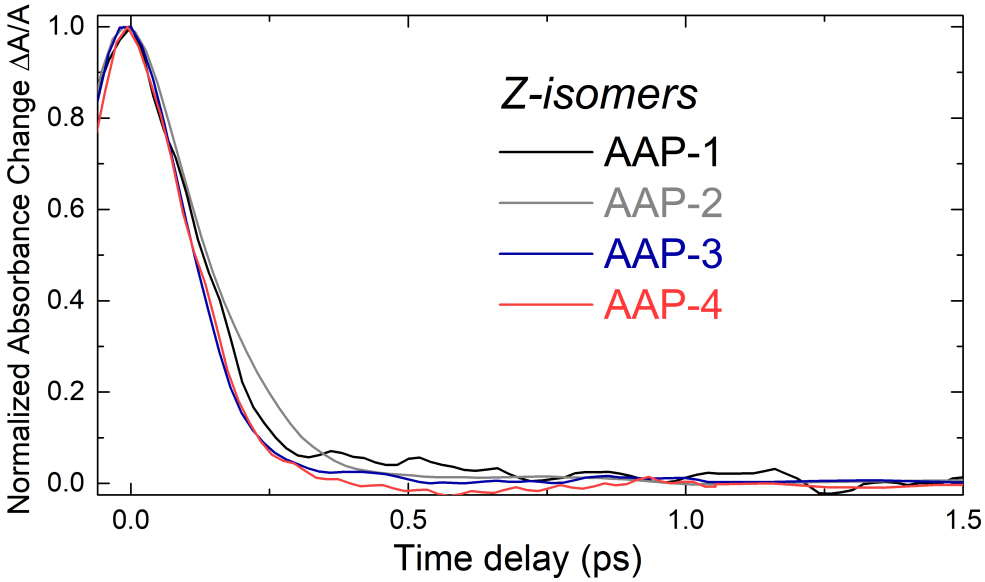

Figure 3.4: Normalized TA spectra for the Z-isomer (with pump wavelength λ_{pump}=430 nm, probe wavelength λ_{probe} = 650 nm, and concentration c=5 mM) for each AAP in water.[1]

Table 3.2: The time constants τ_1 and τ_2 in ps were determined from the monoexponential (Z) and bi-exponential (E) fits, respectively. The associated standard errors were obtained through the fitting procedure (described in the methods section), taking into account the instrument response function (IRF) in the experiment (refer to Fig. 3.5 for Z fits and Fig. 3.6 for E fits).[1]

	Z-Isomer	E-Isomer		
	τ_1 (ps)	τ_1 (ps)	τ_2 (ps)	A_2/A_1
AAP-1	0.1 ± 0.01	0.44 ± 0.02	1.4 ± 0.1	5.9 ± 0.9
AAP-2	0.15 ± 0.01	0.22 ± 0.01	1.4 ± 0.05	13.8 ± 0.2
AAP-3	<0.07 (IRF limited)	0.21 ± 0.01	1.8 ± 0.05	9.2 ± 0.2
AAP-4	<0.07 (IRF limited)	0.17 ± 0.01	1.6 ± 0.1	6.6 ± 0.3

In contrast, akin to prior findings on AB, the AAP E-isomers show slower initial dynamics with a non-negligible > 1 ps contribution. Consequently, an additional exponential decay term is utilized to fit the data for the E-isomer (see blue curves in Fig. 3.6 for slow contribution).

The more pronounced step observed in TA for E-AAPs compared to Z-AAPs is likely due to product absorption (compare gray curves in Fig. 3.5 and 3.6). This can be attributed to the fact that Z-AAPs exhibit greater ground state absorption than E-isomers at the probe wavelength. The increase for this absorption step, defined by its rise time, aligns well with the slow lifetime τ_2. Therefore, it can be expected that AAPs exhibit behavior analogous to ABs, interpreting τ_2 as the time for completed isomerization, the absorption

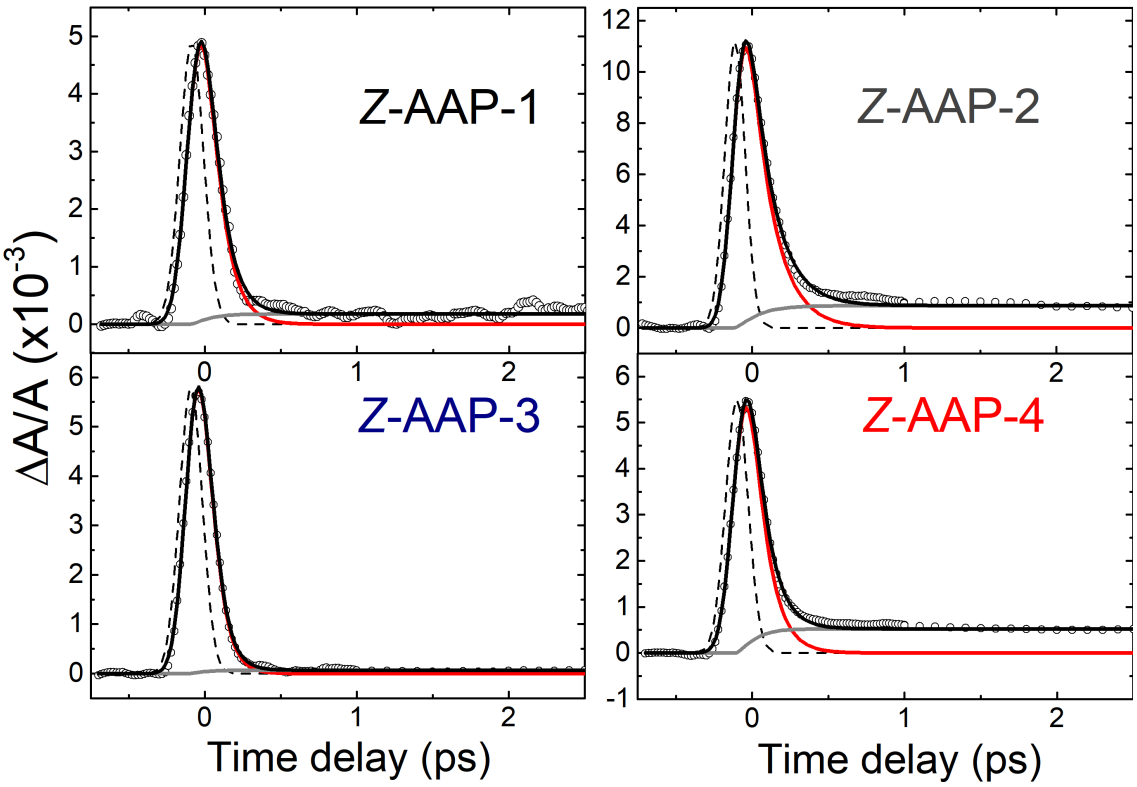

Figure 3.5: Analysis of the TA data for the *Z*-isomer (represented as circles). The complete fit function, which incorporates components of exponential decay (in red and blue) as well as permanent absorption (in gray), is shown in black. Additionally, the instrumental response function (IRF) is depicted by a Gaussian function (dashed line). [1]

step corresponds to the ground state absorption of the newly formed *Z*-isomers. Thus, the slow time constant τ_2 and the rise-time constant of the rising exponential function were restricted to be identical. The low deviation between the fits and the data ($R^2 > 0.99$) suggests that the ultrafast dynamics for all dimethyl-AAPs mimic those of AB which also exhibit a comparable bi-phasic decay under $n\pi^*$-excitation.[32, 27, 90]

Figure 3.7 displays the normalized TA decay curves of the *E*-isomers for every compound together in a single graph. This visualization already makes it clear that AAP-4 (shown in red) is unique in terms of its faster decay.

The right side of Table 3.2 displays the extracted τ_1 lifetimes from the fits (shown in Fig. 3.6) for *E*-AAP-1 (440 fs), *E*-AAP-2 (220 fs), and *E*-AAP-3 (210 fs). These values closely match those recorded for *E*-AB in ethanol (320 fs) as well as in DMSO (340 fs).[32, 27, 90] They also correspond to those observed in the azoheteroarene photoswitch thiophenylazobenzene (400 fs).[97] Conversely, *E*-AAP-4 exhibits a notable reduction in τ_1 (170 fs). This finding supports the initial premise that twisted *E*-AAPs should demonstrate relatively faster initial photoisomerization dynamics. The relative ampli-

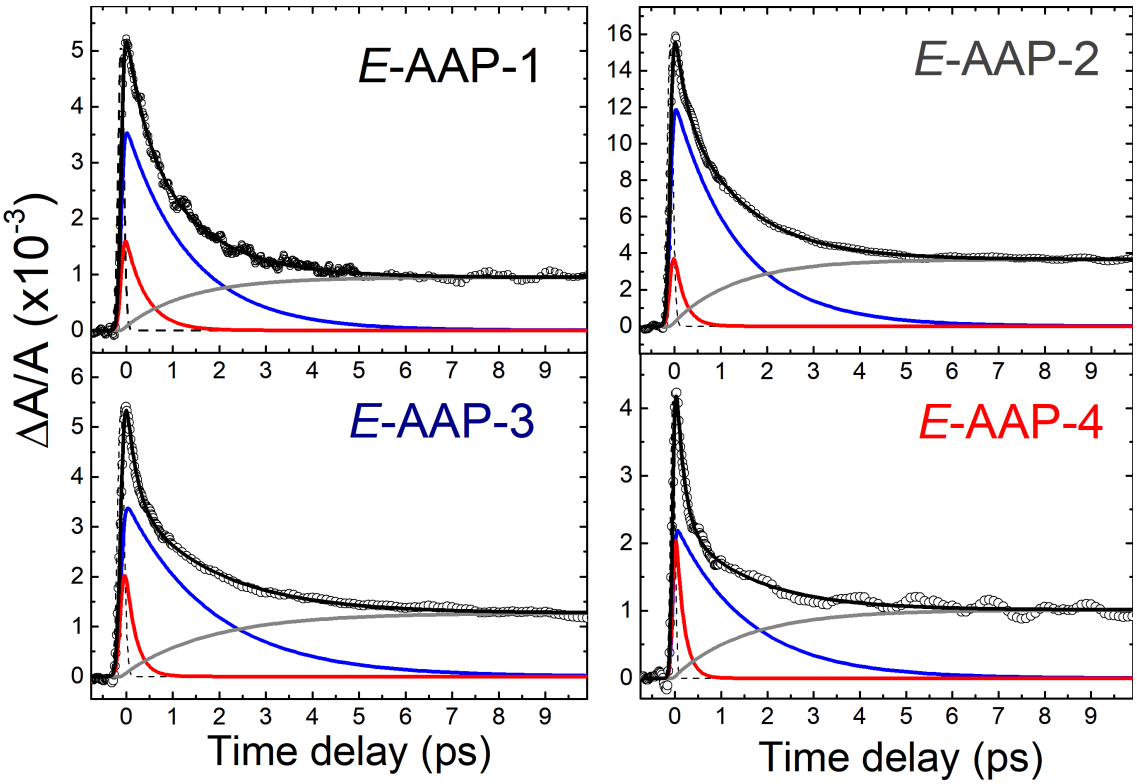

Figure 3.6: TA data analysis for the AAP *E*-isomers done in the format as depicted for *Z*-isomers in Fig. 3.4. However, an additional slow relaxation decay with the lifetime τ_2 (illustrated in blue) is required to accurately fit the *E*-isomer TA data.[1]

tudes (A_2/A_1) for the slower (τ_2) and faster (τ_1) decay lifetimes are displayed in Table 3.2, revealing that *E*-AAP-2 possesses a significantly larger slow decay portion compared to *E*-AAP-1 and *E*-AAP-4. This may indicate a comparatively larger ESA oscillator strength after the initial motion out of the Franck–Condon state.

The τ_2 lifetimes for all four *E*-AAPs range from 1.4 ps to 1.8 ps. These lifetimes, although somewhat reduced ($<$ 2 ps) compared to typical ABs (2-3 ps), are noticeably longer than that of the bridged AB (dihydrodibenzodiazocine) at 0.27 ps. This sharply contrasts with the rapid initial dynamics characterized by τ_1, which varies by approximately a factor of 3 between the planar *E*-AAP-1 (440 fs) and the significantly twisted *E*-AAP-4 (160 fs). The slower lifetime component denoted by τ_2 exhibits similarity across both the planar and the twisted *E*-AAP molecules. For instance, *E*-AAP-1 with $\tau_2 = 1.4$ ps and *E*-AAP-4 with $\tau_2 = 1.6$ ps exhibit only slight variation. This indicates that, despite their contrasts in the rapid initial motion from the Franck-Condon region (τ_1), all *E*-isomers may encounter a comparable impediment for photoisomerization on either the S_1 potential energy surface or at the conical intersection (τ_2).

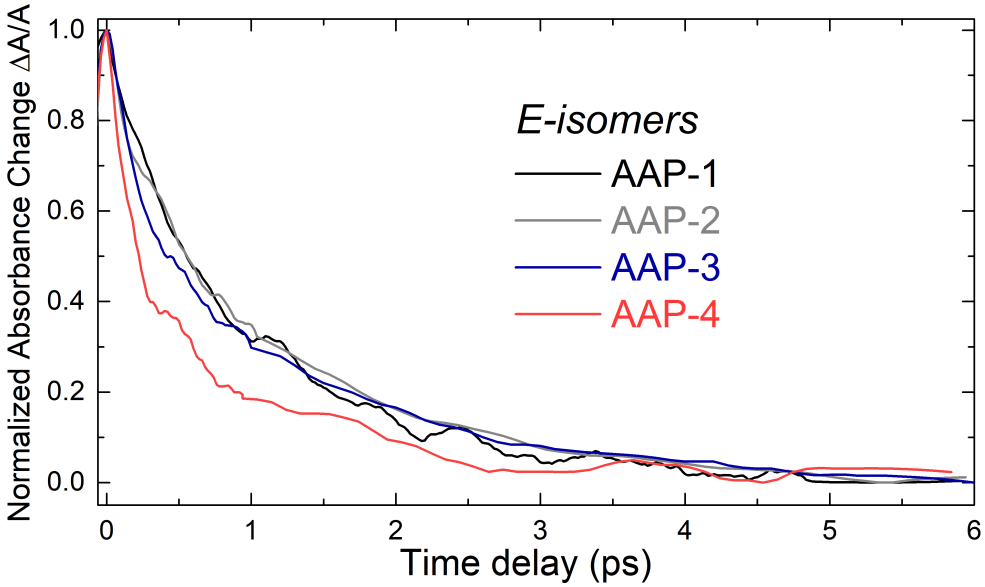

Figure 3.7: Normalized TA spectra for the *E*-isomer (with pump wavelength λ_{pump}=430 nm, probe wavelength λ_{probe}=650 nm, and concentration c=5 mM) of each AAP in water.[1]

Validating the slower time constant poses challenges in computer simulations, primarily owing to the need to incorporate vibrational coupling between the excited and ground state potential surfaces at the conical intersection.[98] On the other hand, simulating the initial movement which is related to τ_1 can be achieved relatively straightforwardly through *ab-initio* molecular dynamics (MD) calculations, a task undertaken by the the Doltsinis group.[99, 41] However, before conducting these simulations, it is important to identify the potential Franck-Condon states each molecule can assume. Each molecule within the ensemble may undergo excitation at slightly different geometry due to thermal energy, allowing a degree of flexibility in the phenyl ring (CCNN) and pyrazole dihedral angle (NNCC). This stands in contrast to the azo bridge dihedral angle (CNNC), which is double-bonded and can be regarded as fixed in the ground state. The minimum potential energy calculated using DFT for all ring rotation angles is depicted in Fig. 3.8.

An examination of the phenyl ring's potential energy landscape (top section) reveals that *E*-AAP-4 exhibits significantly less rigidity, with its minima shallower and shifted by approximately 27° (as expected) compared to the planar *E*-AAP-1 and *E*-AAP-2 having their minima at 0° and 180°. Remarkably, *E*-AAP-3 displays an extremely shallow local minimum at 5°, suggesting the potential for a highly twisted initial geometry upon excitation into the Franck-Condon state. Its global minimum at 180° however is similar to that of the planar AAPs. This similarity helps clarify why *E*-AAP-3 doesn't exhibit a significant difference in the dynamics observed in the TA experiment when compared with the planar *E*-AAP variants. Regarding the pyrazole ring (bottom section), the rotational

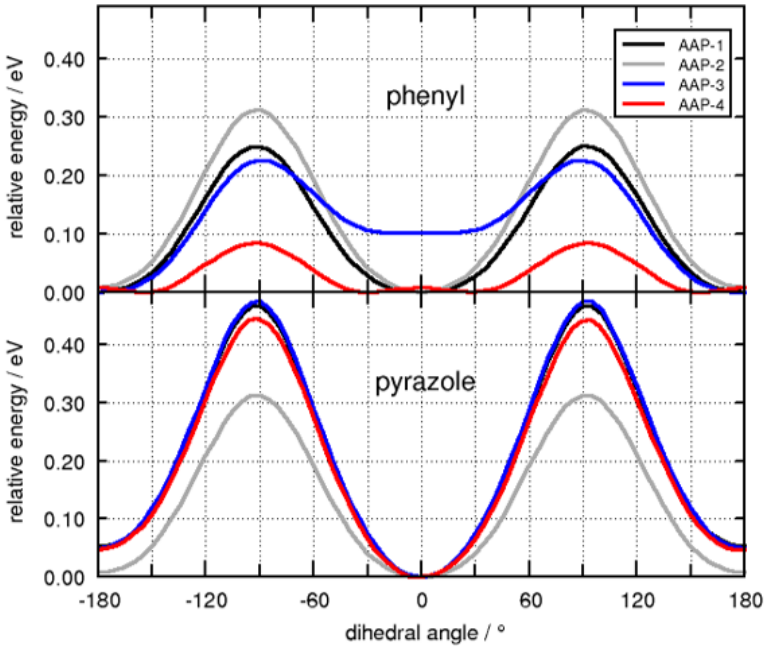

Figure 3.8: Minimum energy potential scans (DFT) of the electronic ground state S_0 computed for the dihedral angle of the phenyl (top) and pyrazole ring (bottom) in all four *E*-AAPs (figure/data produced by M. Böckmann, [1]).

potentials of all *E*-AAPs are comparable. These rotations are anticipated to have less significance in the observed dynamics due to the expected lower interaction between the 5-ring and the azo bridge. *Ab-initio* molecular dynamics calculations to simulate the initial movement from the Franck-Condon state (related to τ_1) were done with a particular focus for *E*-APP-1 and *E*-AAP-4 and results are presented in Fig. 3.9.

In the simulation the initial dihedral angles of the phenyl ring is varied and the movement out of the Franck-Condon state is observed. For the 'natural' planar phenyl angle of 0° of *E*-AAP-1 no dynamics in the main isomerization reaction coordinate (CNNC) angle are observed (black line in Fig. 3.9). The absence of metastability observed for *E*-AAP-1 in transient absorption can be straightforwardly attributed to the ring fluctuations for which the ground state simulations reveal that very few molecules are perfectly planar. Furthermore, it is important to note that the simulation did not consider the zero point energy of the molecule, which could also facilitate an isomerization of the molecule.

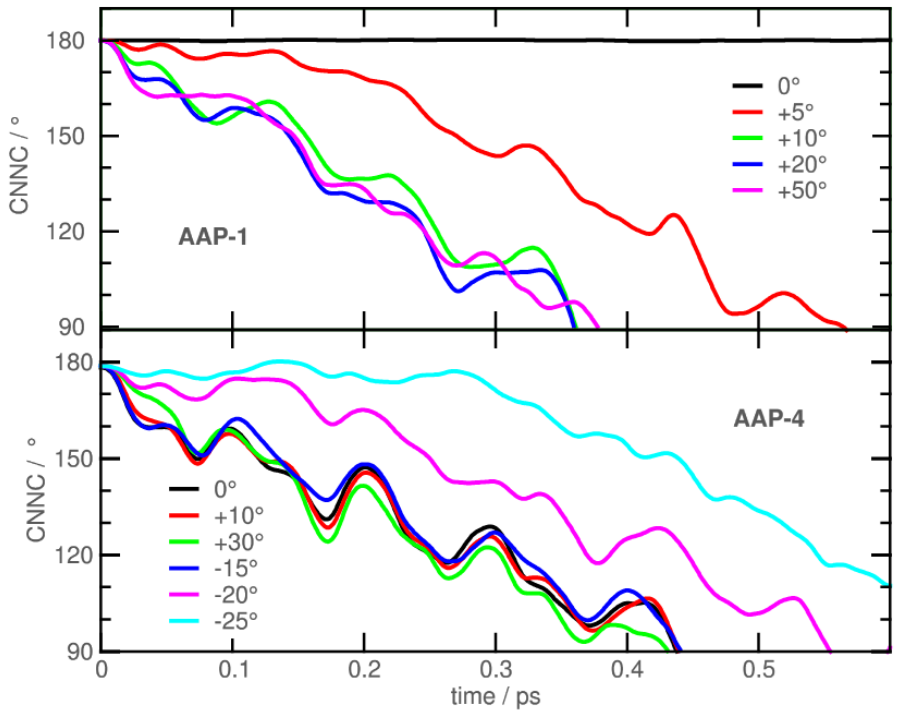

Figure 3.9: MD simulated relaxation for the CNNC dihedral angle in the excited state $S_1(n\pi^*)$ for AAP-1 (top section) and AAP-4 (bottom section) under variation of the initial phenyl ring dihedral angles (figure/data produced by M. Böckmann, [1]).

For simulations where *E*-AAP-1 is forced into a more twisted state, a rapid approach of the CNNC angle towards 90° (conical intersection) is seen (see curves in Fig. 3.9 in red, green, blue, and purple). Similarly shown in the bottom section of Fig. 3.9, the 'naturally' twisted state of *E*-AAP-4 exhibits a rapid movement which is shown by the black curve. By "untwisting" *E*-AAP-4 the simulated isomerization rate can be slowed down towards that of *E*-APP-1 for the negative angles $-20°$ and $-25°$ (compare black to purple and cyan curves). Consequently, these simulations suggest that the initial twist of the phenyl ring in *E*-AAP-4 is what causes the faster τ_1 lifetime found in the TA experiment. A plausible reason for this can be attributed to a stabilizing impact of the conjugation between the phenyl rings π system and the (antibonding) p-orbital of the azo group in planar *E*-isomers.

Finally, results from *ab-initio* MD simulations for every AAP molecule are depicted in Fig. 3.10. The top portion of Fig. 3.10 illustrates simulations for *E*-isomers. *E*-AAP-2 (depicted by the gray curve) is anticipated to exhibit an intermediate initial relaxation lifetime between *E*-AAP-1 (depicted in black, metastable) and *E*-AAP-4 (depicted in red). In the case of *E*-AAP-3, two phenyl ring orientations exist (anti: 0° and syn: 180°). It is expected that the anti-orientation will share the same lifetime as *E*-AAP-2, whereas the syn-orientation will entail a longer relaxation time. These computational

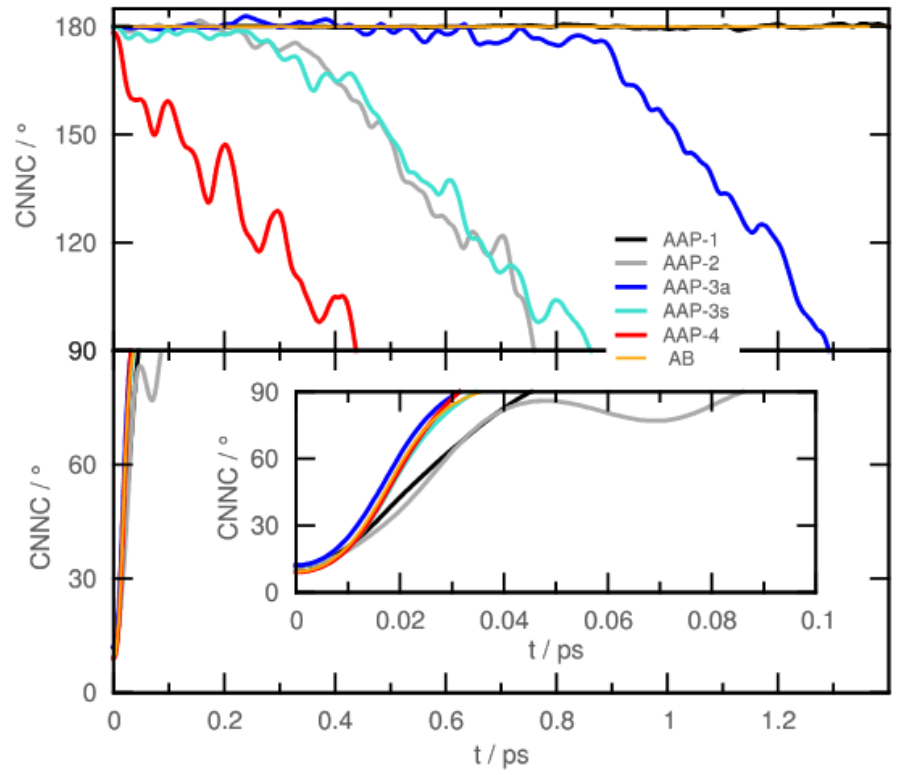

Figure 3.10: MD simulated relaxation for the CNNC dihedral angle in the excited state $S_1(n\pi^*)$ for E-isomers (top) and Z-isomers (bottom) of the investigated AAPs (figure/data produced by M. Böckmann and reprinted from [1] with permission).

findings broadly correspond with the TA experiment; however, for E-AAP-3, there is no significant deviation in lifetime compared to E-AAP-2.

Furthermore, the sequence of Z-isomerization rates displayed in the bottom section of Fig. 3.10 correlates with experimental observations. Z-AAP-3 and Z-AAP-4 exhibit here the most rapid relaxation, while Z-AAP-2 is expected to have the longest Z-isomer lifetime.

Broadband Transient Absorption Measurements

Broadband transient absorption (TA) experiments were conducted to determine the ESA maximum position for AAPs. These experiments were carried out at an increased repetition rate to enhance the signal-to-noise ratio (SNR). This adjustment was necessary as the white light probe power, approximately 2 mW, was distributed across a wide range of frequencies. Additionally, it was anticipated that the NMOS detector, employed for broadband TA, would present some challenges.

Initially, a measurement was conducted on the well-characterized molecular photoswitch azobenzene to validate the functionality of the detection scheme. Unfortunately, the appropriate LED lamps for switching the molecule were unavailable, necessitating the measurement of azobenzene as a mixture of isomers. For this reason, the measurement was carried out at 20 kHz to maximize signal strength. Consequently, a transient signal was observable prior to $t = 0$ (as was depicted for AAPs in Fig. 3.2). The measurement was done with a timestep of only 500 fs since the primary objective was to determine the spectral position of the ESA maximum. The results revealed an ESA maximum at approximately 535 nm, consistent with literature values that report the E-isomer's ESA maximum at 530 nm and the Z-isomer's at 540 nm.[89] Subsequent measurements were then performed on AAPs.

Firstly, the TA signal of both AAP-2 isomers is depicted in Fig. 3.12 obtained at a laser repetition rate of 10 kHz. AAP-2 was selected as the most straightforward molecule to observe the differences between E and Z isomers owing to its elevated PSS. Chirp compensation was needed due to the reduced timestep of ca. 100 fs; this was achieved by incorporating a linear time-wavelength shift. The distinct relaxation times between E and Z isomers are observable for AAP-2 at the ESA maxima for Z-AAP (around 575 nm) and E-AAP (approximately 580 nm). Some oscillations are noticeable in the measurements; this might have been caused by a periodic loss of synchronization between the camera and the chopper.

For the twisted Z-rich AAP-4, a measurement (refer to Fig. 3.13) indicates two major signals, one in the visible and one in the IR. Each signal exhibits a double peak, possibly due to the Z-rich mixture still containing approximately one-third of E-isomers. The visible signal shows a slight red shift compared to both isomers of AAP-2. ESA maxima in the visible range are at 570 nm and 590 nm; two additional ESA peaks in the red are observed at 675 nm and roughly 700 nm.

The existence of a red-shifted ESA in the visible for both E and Z isomers of AAP-4 is consistent with TDDFT calculations conducted by M. Böckmann (see Fig. 3.14). However, the simulations exhibit a generally more blue-shifted ESA below 550 nm. On the other

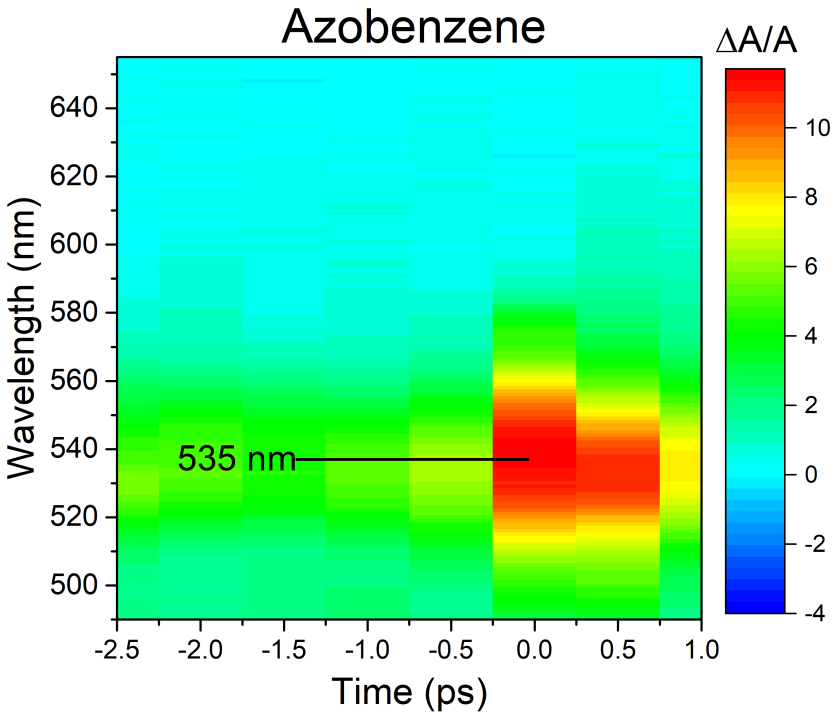

Figure 3.11: Broadband TA spectrum of a mixture of both azobenzene isomers (integration time: ca. 4 hours, timestep 500 fs, spectrometer grating: 150 lines/mm, λ_{pump}=430 nm).

hand, ESA peaks observed in the IR of the TA spectrum for AAP-4 are significantly red-shifted (approximately 100 nm) compared to predictions from calculations.

In summary, despite the poor signal-to-noise ratio, the measurements suggest a red-shifted ESA maximum for both *E*- and *Z*-isomers in AAP-2 and AAP-4. However, further measurements are warranted to validate this observation, as strong fluctuations were observed in the white light probe during the experiments. The broadband measurements were particularly challenging due to significant humidity shifts (up to 60%) and temperature variations (up to 3°C) in the laboratory, resulting in the loss of the white light probe. Encapsulating the white light generation material in an airtight seal, similar to the OPAs, should alleviate this issue. Additionally, the use of a camera capable of shot-to-shot detection and a global shutter is likely to substantially improve the signal-to-noise ratio.[85]

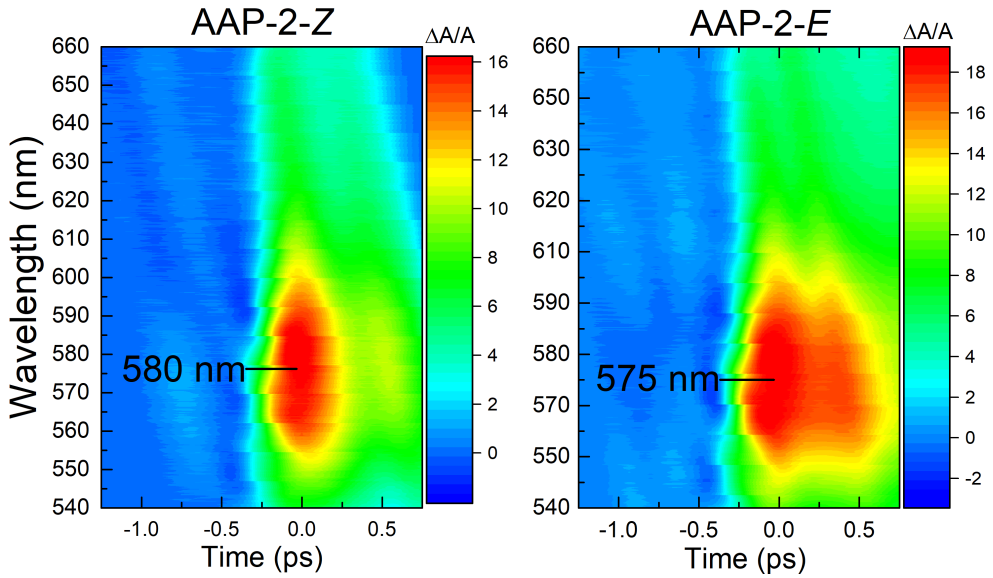

Figure 3.12: The broadband TA spectra for *Z*-AAP-2 on the left and for *E*-AAP-2 on the right (grating: 600 lines/mm) reveal a solitary broad ESA in each recording (integration time: approximately 12 hours, timestep 100 fs, λ_{pump}=430 nm).

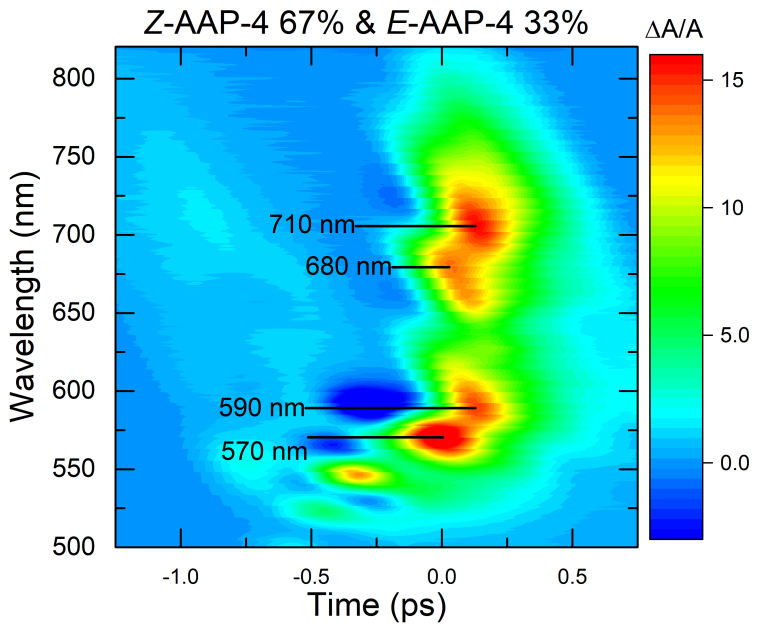

Figure 3.13: Broadband TA spectrum of *Z*-rich AAP-4 (grating: 150 lines/mm, integration time: approximately 10 hours, timestep 200 fs, λ_{pump}=430 nm).

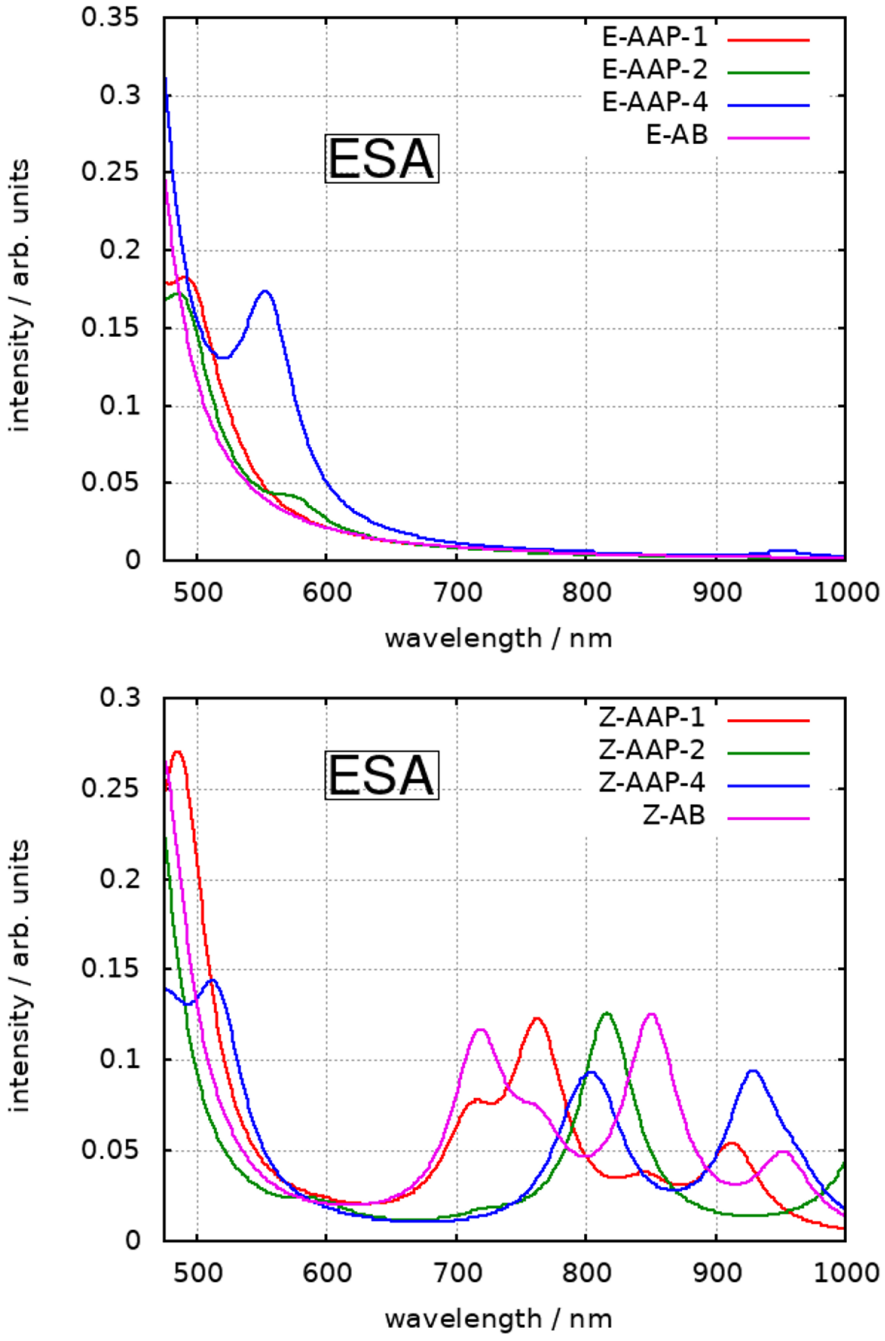

Figure 3.14: TDDFT TA spectra of *E*-AAPs (top) and *Z*-AAPs (bottom) (figure/data produced by M. Böckmann, reprinted from SI in [1]).

3.1.1 Conclusion: Photoisomerization of Arylazopyrazoles

This study on the ultrafast dynamics in photoswitching for AAPs indicates that planar AAPs, exemplified here by AAP-1 and AAP-2, exhibit similar dynamics to conventional ABs upon $n\pi^*$ excitation, showing a bi-exponential decay with rapid (τ_1) and slower (τ_2) components. It was anticipated that AAP *E*-isomers would display accelerated dynamics resembling *Z*-isomers if it possessed an initial twist in the ground state, as previously demonstrated with the bridged AB by the groups of Herges, Hartke and Temps in Kiel.[31]

This is supported by the TA measurements which show a reduction of τ_1 from 220–440 fs for *E*-AAP-1 (440 fs), *E*-AAP-2 (220 fs), and *E*-AAP-3 (210 fs) to 170 fs for *E*-AAP-4. Additional support was provided by *ab-initio* MD calculations, which indicate that the planar *E*-AAP-1 should be metastable in the absence of temperature and zero initial velocity. All experimental observations, including the intermediate lifetimes of *E*-AAP-2 and *E*-AAP-3, are consistent with results from these simulations.

The proposed reason for the less significant acceleration observed when comparing *E*-AAP-4 to the twisted and bridged AB ($\tau_1 < 50$ fs) is the flexibility of the phenyl-ring of *E*-AAP-4 in its ground state at room temperature.[31] Conversely, the slower picosecond dynamics (τ_2) observed in the TA experiment remains unaltered for the twisted *E*-AAP-4, suggesting that the main hindrance of $E \rightarrow Z$ isomerization at the conical intersection persists.

Broadband TA measurements of *E*-AAP-2, *Z*-AAP-2 and *Z*-AAP-4 suggest that the primary ESA maximum in the visible is centered between 550-600 nm, slightly red-shifted compared to AB. Additionally, for the *Z*-isomer of AAP-4, there appears to be an additional ESA band in the red at ca. 700 nm. Nonetheless, further measurements are necessary to validate these findings due to issues with white light stability.

In summary, the findings suggest that additional substituents at the ortho-position of the phenyl ring do not sufficiently influence the dynamics of the *E*-isomer to achieve a significantly faster *E*-isomer dynamics. Alternative strategies, such as employing a rigid bridged AAP analogous to the known bridged AB, may be necessary to achieve this goal. Improving the quantum yields by the accelerated dynamics of new AAP photoswitches could facilitate reaching the photostationary state (PSS) with less light irradiation which is important for applications where irradiation is significantly attenuated. Since AAP-2 exhibits exceptional PSS and slightly faster dynamics than AAP-1, it appears to be a promising candidate for improvement through structural alterations.

Designing a molecule with better isomerization yields could be done with the guidance of *ab-initio* molecular dynamics simulations. This is supported by the fact that TA measurements have demonstrated their ability to accurately predict the sequencing of the

initial dynamics τ_1 across various AAPs. In the future, temperature should also be accounted for by averaging the photoisomerization trajectories across an array of possible Franck-Condon geometries. Furthermore, there is still a need for additional theoretical exploration in predicting τ_2 which will likely entail accounting for vibronic coupling effects. One approach would involve utilizing Time-Dependent Density Functional Theory (TDDFT).

3.2 Resonance Raman Study on the Anthracene ^1L_a state

This chapter begins with preliminary measurements aimed at testing the characteristics of the UV Kerr gate. Following this, the molecule anthracene is examined using the UV Kerr-gated Resonance Raman system in the $^1L_a(0-0)$ state. However, measuring the resonance Raman spectra at the ^1L_a state poses experimental challenges due to strong overlapping fluorescence, necessitating the use of UV Kerr-gated Raman spectroscopy.

Kerr-gate Transmission

The first important step before initiating Raman measurements is to test the performance of the Kerr Gate with different media. For this, the laser probe beam of 376 nm (later used for Raman excitation) was simply 90° reflected at the sample position into the Kerr medium. The total signal in front of the spectrometer slit was measured using lock-in detection (the same instruments which were used for narrowband transient absorption) by placing a chopper into the Raman excitation beam path. Lock-in detection was utilized to improve the signal-to-noise ratio as well as to eliminate background signals from ambient light. Finally, this signal was also divided by the signal with parallel polarizers (I_{max}) to obtain the transmission through the Kerr gate in percentages. Figure 3.15 shows the resulting Kerr gate transmission for a variety of liquids (2 mm thick cuvette, Hellma Optik, 100-QS, 100-2-40) as well as for one solid medium (2.5 mm thick BK7 glass) while changing the Kerr gate delay.

The transmission profiles of various Kerr media show that the known Kerr gate medium, benzene, exhibited the best performance with a 70% probe transmission.[100] Toluene and p-xylene showed slightly lower transmission. Not surprisingly, the only solid medium, BK7 glass, performed poorly (0.35% transmission), lacking the nuclear contributions present in liquid media. In Fig. 3.16, the signals are normalized to facilitate comparison of response times across different media. Glass is expected to have the fastest response time since its effect is purely electronic.[101] Glass, water, and benzyl alcohol, along with DCM and acetonitrile (not shown to avoid cluttering the figure), all exhibit similar FWHM values of approximately 2.2 ps. This indicates that most liquids have response times comparable to or shorter than the Raman pulse duration with the exception of p-xylene and toluene. Based on these measurements, the Raman pulse duration can be estimated to be nearly the same as that for the glass measurement, owing to the significantly shorter Kerr gate pulse (ca. 500 fs): $\sigma_{probe} = \sqrt{\sigma^2_{probe\otimes Kerr} - \sigma^2_{Kerr}} = \sqrt{2.2^2 - 0.5^2}$ ps ≈ 2.1 ps.

Among aromatic molecules, benzene displayed the fastest Kerr gating response with its

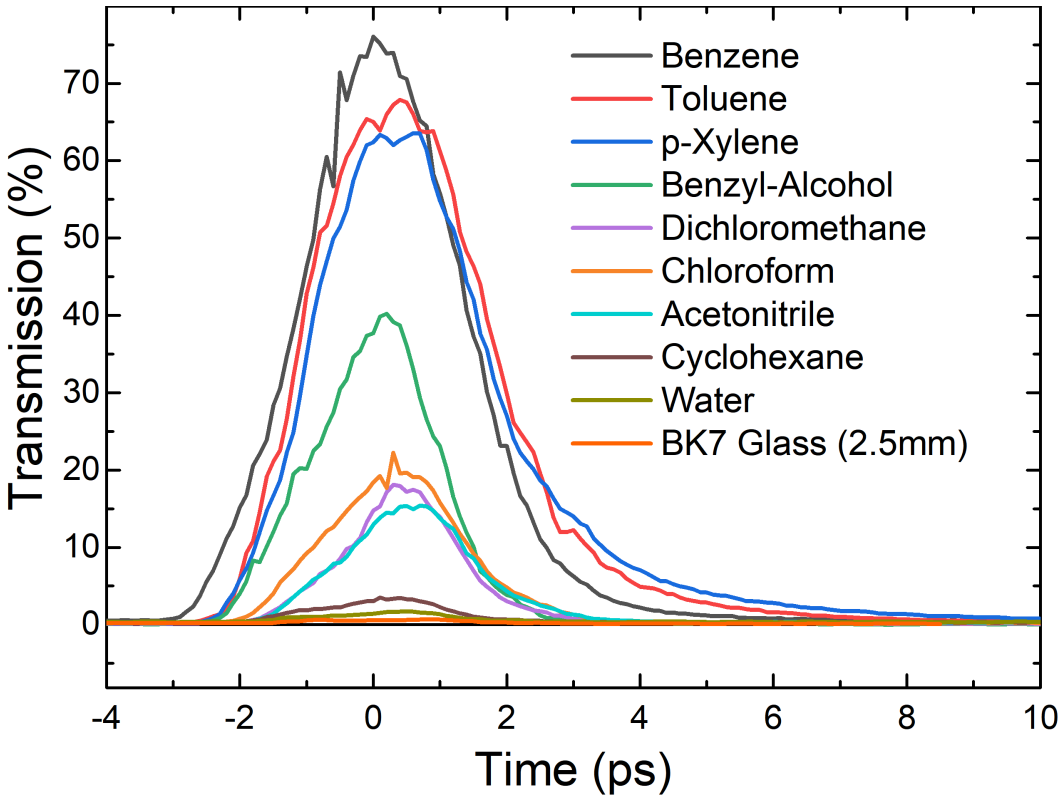

Figure 3.15: Testing the Kerr gate transmission using the UV probe beam (376 nm) with various Kerr media placed into a 2 mm thick cuvette under variation of the Kerr pulse delay.

Kerr gate opening time of ca. 2.6 ps (FWHM), which is faster than toluene (2.9 ps) and p-xylene (3 ps). Such a reduced duration of the Kerr gate opening time should assist in fluorescence suppression. Benzyl alcohol showed the fastest response, however, its Kerr gate transmission was significantly lower.

This ordering of nonlinear response times and magnitudes among the aromatic compounds compares well with data from literature. For example, p-xylene has a larger and slower diffusive reorientational component than benzene and toluene.[58] Consequently, benzene was chosen as the optimal Kerr gate medium for measurements of the UV wavelengths $290 - 400$ nm. Given that benzene absorbs below approximately 290 nm, acetonitrile emerges here as a suitable material for UV Raman Kerr-gated measurements between $200 - 290$ nm. Furthermore, measurements were conducted using benzene with various cuvette thicknesses. The maximum transmissions for 1 mm, 2 mm, and 10 mm are depicted in the Fig. 3.17.

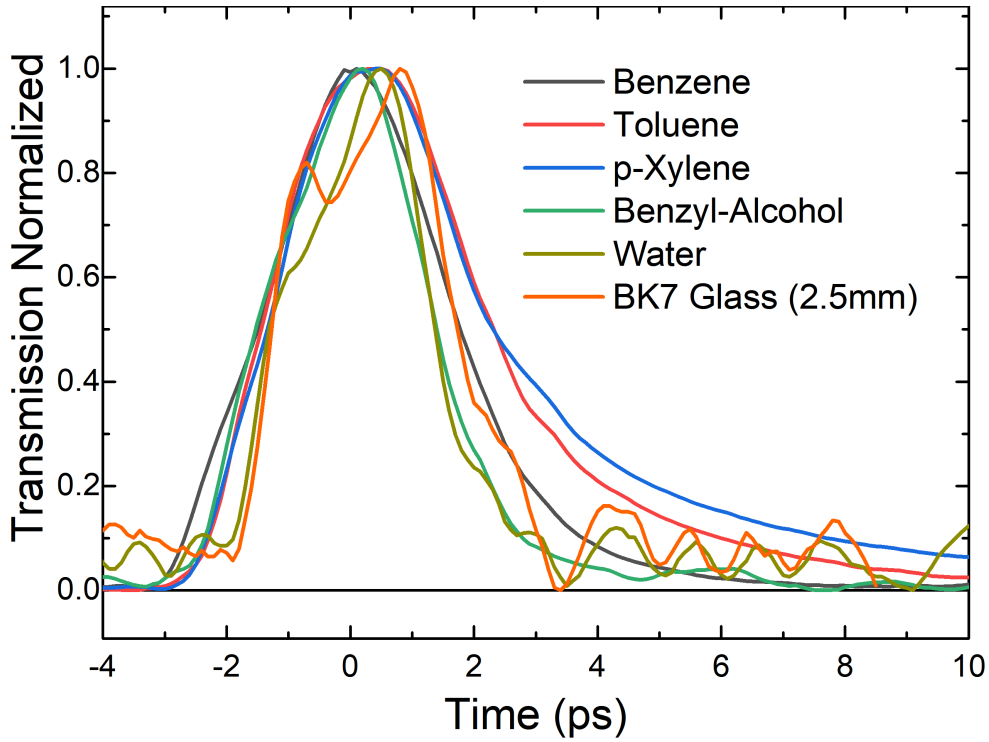

Figure 3.16: Normalized transmission curves for some of the Kerr media shown in Fig. 3.15.

As anticipated, the thicker Kerr media resulted in considerably higher transmissions, owing to the near collinear crossing angle of approximately 15°, resulting in longer effective interaction lengths. Notably, the 10 mm cuvette exhibited transmissions of ca. 90%. Additionally, the increased cuvette length facilitates the alignment process. Hence, the 10 mm cuvette was selected for subsequent experiments.

For Raman measurements, it is unlikely that such high transmissions were actually attained since the scattered light could not be focused as tightly (ca. 0.8 mm $\frac{1}{e^2}$ diameter) as the probe laser beam (ca. 0.2 mm diameter). Another notable difference is that, the scattered light projects a line within the Kerr gate medium, due to the beam traversing the ca. 3 mm thick flow-cuvette sample, as can be seen by a beam profiler image shown in Fig. 3.18.

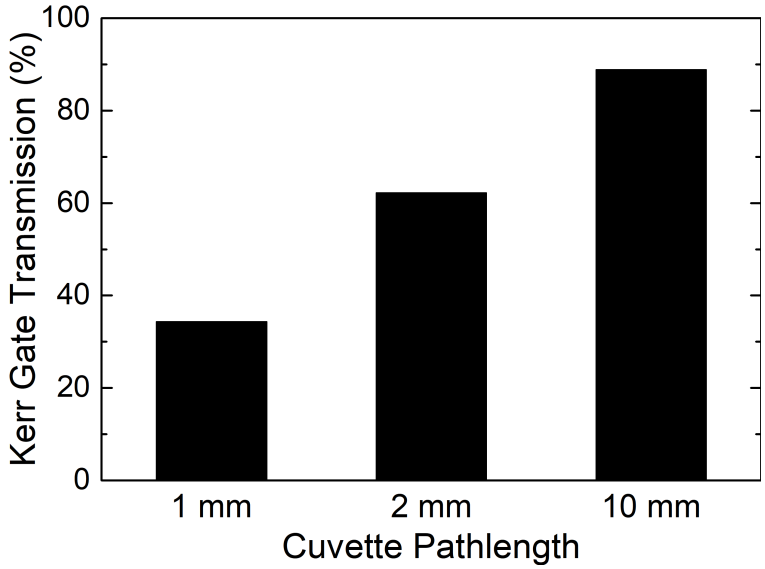

Figure 3.17: Maximum Kerr gate transmission using the Kerr gate medium benzene with cuvette thicknesses 1 mm, 2 mm and 10 mm Hellma Optik (Hellma Optik, 100-QS).

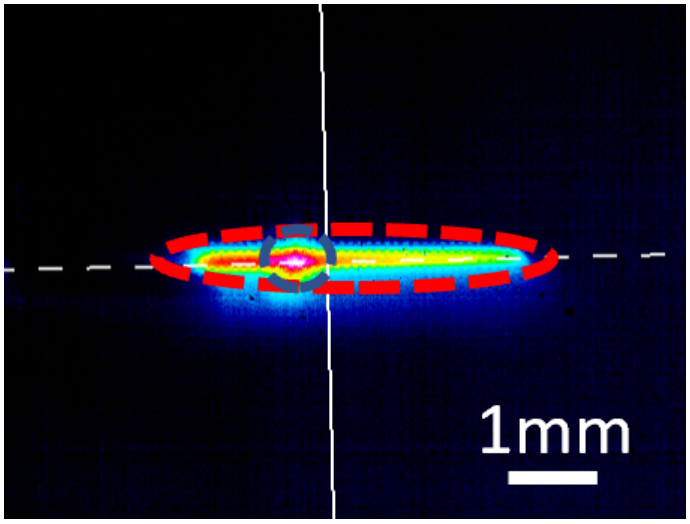

Figure 3.18: Beam profile image at the position of the Kerr medium. The Raman scattered light is indicated by an oval dashed red line measuring 0.8 x 4 mm. This scattered light originates from the left side upon entrance into the Raman sample, with the absorption along the pathlength seen from the diminished signal towards the right. The Kerr pulse, with approximately a 1 mm beam diameter, is marked by a blue dashed circle.

Dimerization

It was important to address the known dimerization phenomenon (photochemical side reaction) for resonance Raman spectroscopy at the ^1L_a state. Figure 3.19 presents the (summed) fluorescence signal for 376 nm excitation using a 2 L reservoir in the flow system containing anthracene (1.3 mM) in acetonitrile over a 17-hour exposure period. The decline in fluorescence signal indicates the occurrence of dimerization reactions and subsequent losses, as the anthracene dimers are not in electronic resonance with the Raman excitation beam. Typically, measurement durations for the 1.3 mM solution were approximately 1-6 h per measurement. The linear decrease in fluorescence suggests that roughly 0.8% of anthracene converts to dimers every hour for a fresh solution. To minimize unnecessary UV light exposure between successive measurements, automation of the measurement process was implemented. At the conclusion of each measurement, all laser shutters are automatically closed. Furthermore, in most measurements, the solution at the reservoir was swapped.

Despite these efforts, the concentration loss of anthracene introduces a systematic error, which unfortunately cannot be entirely mitigated without resorting to very low concentrations that reduce the Raman signal or by increasing the sample volume of the flow system to wasteful amounts.

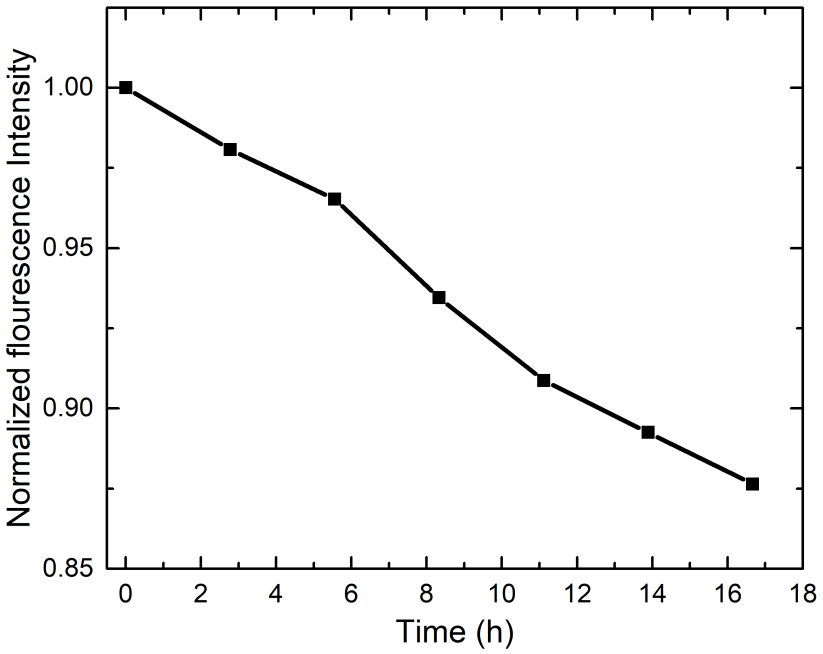

Figure 3.19: Summed and normalized fluorescence signal of anthracene in acetonitrile (c=1.3 mM, $\lambda_{exc} = 376$ nm, $I_{ex} \approx 15\ mW$,) using the flow system (2 L reservoir). The signal over a 17-hour period reveals a decrease in intensity, which is attributed to the dimerization of anthracene.

Absorption Spectrum

Before conducting resonance Raman measurements initially the absorbance spectrum of anthracene dissolved in acetonitrile is examined at the ^1L_a band to determine the approximate laser excitation wavelengths for UVRR. The absorbance spectrum shown in Fig. 3.20 has distinct maxima at 376 nm (0-0), 357 nm (1-0), and 339 nm (2-0) due to vibronic fine structure. In contrast, the ^1B_b state near 250 nm is composed of a single asymmetric peak.[69] Notably, these maxima are approximately 1400 cm^{-1} apart. Consequently, if the anthracene molecule is probed, for instance, in UVRR at 357 nm instead of 376 nm, the Raman scattering is likely to involve a transition to the second quantum of the vibration in the electronic excited state. Since the ^1B_b state possesses an oscillator strength approximately 30 times larger, to achieve similar Raman intensities, the concentration likely needs to be increased roughly by this factor.[102, 69] For instance, Holtum *et al.* utilized a concentration of 0.1 mM, while Efremov *et al.* employed a concentration of 0.19 mM. Therefore, in this study, concentrations exceeding 1 mM were utilized.

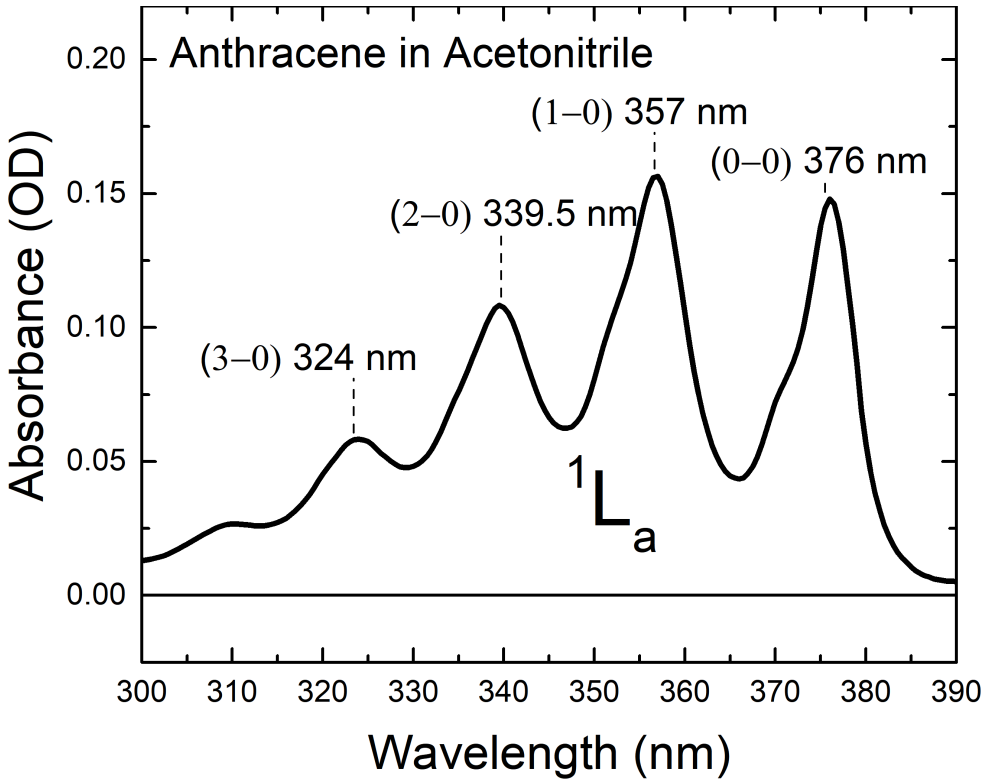

Figure 3.20: UV absorption spectrum of the ^1L_a vibronic states of anthracene (c=1.3 mM) in acetonitrile.

Resonance Raman Measurements

In this thesis, only the resonant Raman signal of the first vibronic state $^1L_a(0-0)$ is investigated. The rationale behind this choice stems from the absence of lower excited states expected to be reached below this wavelength. Consequently, vibrational coupling to other excited states should reduce considerably on the lower wavelength side, simplifying the interpretation. Additionally, the Raman light is less susceptible to reabsorption owing to the red shift of the Raman signal below the absorption band. However, the primary drawback of this choice is that it involves the greatest level of fluorescence background within the Raman signal.

Measurements using 376 nm Raman excitation with a high concentration of 15 mM are shown in Fig. 3.21 to illustrate the typical spectra observed using the Kerr gate. The spectrum, obtained when the Kerr gate pulse is synchronized with the Raman scattered light pulse ($\Delta t = 0$), is represented by the black curve. However, even with Kerr gating, the resultant spectrum is largely masked by a fluorescence contribution, with only a few Raman peaks barely discernible.

Additionally, a signal is recorded with the Kerr gate pump blocked, shown by the green curve, which exhibits a considerable reduction in fluorescence signal. This observation suggests that the majority of the fluorescence is gated with the Raman signal by the Kerr gate pulse (factor of ca. 2.7). The predominate contribution to this fluorescence signal can therefore be attributed to the relatively short fluorescence lifetime of anthracene, which is approximately 6 ns.[103] Estimating the maximum possible fluorescence rejection (without Kerr gate leakage) can be done using the formula proposed by Everall *et al.* as follows: $f_k = (1 - e^{-\frac{\tau_g}{\tau_f}})^{-1} = (1 - e^{-\frac{2.6 \text{ ps}}{6000 \text{ ps}}})^{-1} = 2300$.[65]

Consequently, temporal filtering of the scattered signal cannot effectively suppress this type of fluorescence without resorting to shorter excitation pulses. Adjusting the pulse duration was however not feasible with the existing setup.

Therefore, a unique approach was adopted to retrieve the Raman spectrum from the overwhelming fluorescence. The red curve in Fig. 3.21 depicts the spectrum following a delay slightly longer than one pulse duration ($\Delta t = 3$ ps). In this case, the fluorescence signal displays comparable spectra, albeit slightly higher compared to $\Delta t = 0$ ps however, no Raman peaks are Kerr-gated. The higher signal at $\Delta t = 3$ ps can be attributed to the rise time of fluorescence, which has not yet reached its maximum within the picosecond time scale. This forward delayed signal is utilized as a reference for reconstructing the Raman spectrum by dividing it with the Raman-synchronized signal ($\Delta t = 0$ ps).

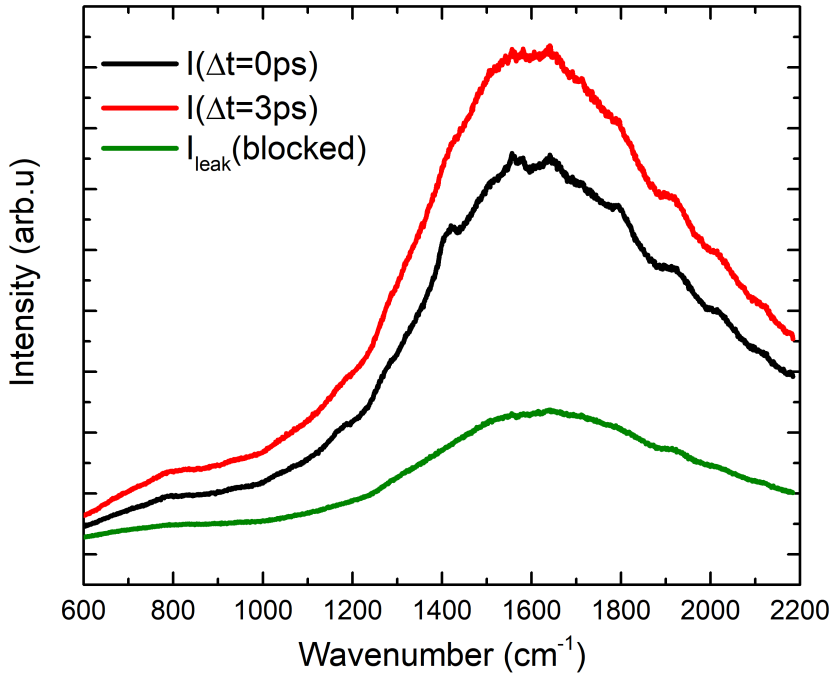

Figure 3.21: The Kerr-gated spectrum, depicted in black, illustrates the signal where the Kerr pulse is synchronized ($\triangle t = 0$) with the Raman signal of the sample (15 mM anthracene in acetonitrile). The red curve represents the spectrum with an additional forward delay of $\triangle t = 3$ ps. Finally, the green spectrum depicts the signal with the Kerr pulse blocked, representing the leaked signal passing through the Kerr-gate polarizers.

Since both spontaneous fluorescence I_F and spontaneous Raman I_{Raman} signals are incoherent, the spectrum observed at $\Delta t = 0$ ps is the sum of these two signals. On the otherhand, the signal at $\Delta t = 3$ ps consists (almost) solely of fluorescence. Consequently, upon dividing the two spectra, the resultant spectrum $S_{ref,div}(\lambda)$ is as follows:

$$S_{ref,div}(\lambda) = \frac{I(0\text{ ps}) - I_{leak}}{I(3\text{ ps}) - I_{leak}} \tag{3.4}$$

$$\sim \frac{(I_{Raman}(\lambda) + I_F(0\text{ ps}, \lambda))}{I_F(3\text{ ps}, \lambda)} \tag{3.5}$$

$$= \frac{I_R(\lambda)}{I_F(3\text{ ps}, \lambda)} + \frac{I_F(0\text{ ps}, \lambda)}{I_F(3\text{ ps}, \lambda)} \tag{3.6}$$

$$\Rightarrow I_{Raman}(\lambda) \sim \left(S_{ref,div}(\lambda) - \frac{I_F(0\text{ ps}, \lambda)}{I_F(3\text{ ps}, \lambda)} \right) \cdot I_F(3\text{ ps}, \lambda). \tag{3.7}$$

The use of this relation will be demonstrated using the measurement of anthracene in acetonitrile (15 mM) at $\lambda_{exc} = 376$ nm. Initially, it is shown that the fluorescence signals at $\Delta t = 0$ ps and $\Delta t = 3$ ps roughly match in their spectral intensity profile. For this, the spectrum $I(3\text{ ps}) - I_{leak}$ is scaled by a factor determined from a wavenumber devoid of any

Raman peak (approximately 1500 cm^{-1}) to equalize it with the spectrum $I(0\ ps) - I_{leak}$ (see Fig. 3.22). Upon applying this scaling factor, the spectra largely overlap.

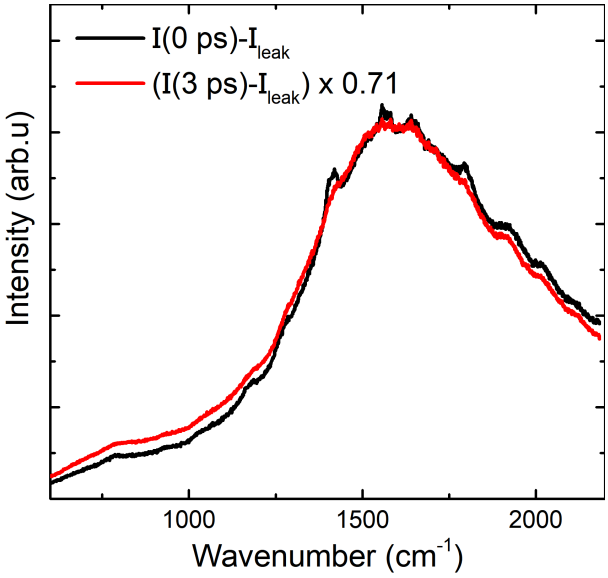

Figure 3.22: The left figure illustrates the subtraction of the polarizer leakage signal from the two delayed Kerr-gate signals. On the right, the signals are nearly overlapped after scaling the signal with a Kerr pulse delay of 3 ps (factor 0.71).

Following this, the Raman signal is extracted based on Eq. 3.7. Figure 3.23 presents the divided spectrum of $I(0\ ps) - I_{leak}$ and $I(3\ ps) - I_{leak}$, with a 20-point Savitzky-Golay (2nd order polynomial) smoothing applied. Each CCD pixel corresponds roughly to 1 cm^{-1}. The spectrometer slit had to be kept relatively wide (ca. 0.2 mm) in order to obtain sufficient signal which was reduced from the transmission losses of the Kerr gate. Therefore, most peaks observed in this study exhibited an FWHM of $> 20\ cm^{-1}$ and the spectral resolution was therefore not affected by the smoothing operation.

Notably, a gradient persists in the spectrum, possibly arising from GVD synchronization effects or, alternatively, it could be attributed to slight changes in the time-dependent fluorescence spectrum occurring in the first picoseconds (picosecond time-resolved fluorescence represents another important application of a Kerr gate).[104] However, the majority of the remaining signal now consists of the Raman peaks. Subsequently, the gradient, i.e., the baseline, is manually subtracted using a spline function between the Raman peaks representing the ratio $\frac{I_F(0\ ps,\lambda)}{I_F(3\ ps,\lambda)}$ in Eq. 3.7 (shown in black on the right side of Fig. 3.23). This spectrum depicted in black on the left side of Fig. 3.23 is then scaled by $I_F(3\ ps)$, which adjusts the Raman intensities (blue spectrum).

This spectrum of anthracene in acetonitrile (15 mM) at $\lambda_{exc} = 376$ nm is shown again in Fig. 3.24 and will be discussed initially since the singal is larger in comparison to the

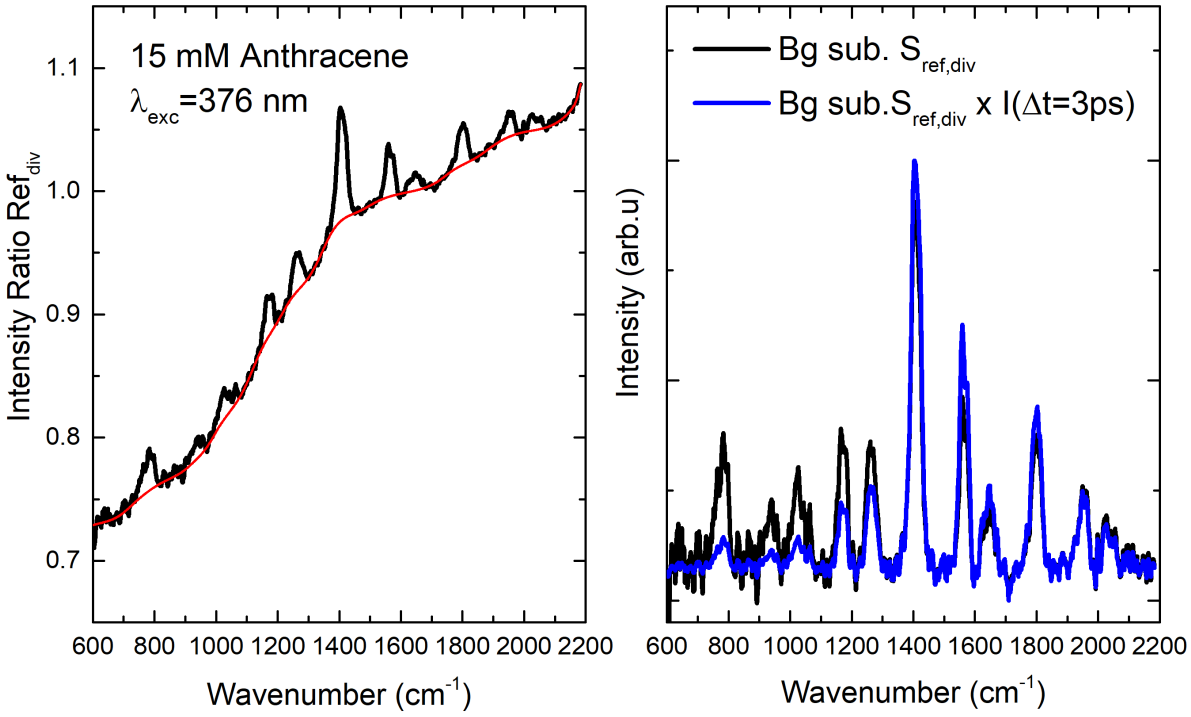

Figure 3.23: On the left side, the two measurements $I(0\text{ ps})$ and $I(3\text{ ps})$ are divided and subjected to manual background subtraction (indicated by the subtracted spline function displayed as a red dashed line). On the right side, the manually background-subtracted spectrum is depicted in black. This spectrum is then (re)multiplied by $I(3\text{ ps})$ to obtain the final Raman spectrum, as shown in blue.

more dilute measurements shown later. Most of the prominent bands visible in this fingerprint region are recognized as totally symmetric modes, such as 1165 cm^{-1}, 1260 cm^{-1}, 1405 cm^{-1}, and 1560 cm^{-1}. In prior research, Holtum *et al.* identified these modes at 1162 cm^{-1}, 1259 cm^{-1}, 1405 cm^{-1}, and 1561 cm^{-1} while Efremov *et al.* observed these Raman peaks at 1146 cm^{-1}, 1237 cm^{-1}, 1406 cm^{-1}, and 1552 cm^{-1}.[102, 69]

The interpretation of the Raman peak detected near 785 cm^{-1} poses a challenge. It is most probable that this Raman peak corresponds to the one observed for anthracene around 755 cm^{-1}, a typically intense totally symmetric ring-breathing mode.[102, 69] However, notably, its relative intensity compared to the prominent mode at 1405 cm^{-1} would be significantly diminished compared to spectra observed at the ^1B_b resonance. Additionally, the Raman peak at 785 cm^{-1} appears to have an asymmetric lineshape tending towards higher wavenumbers exactly opposite to the peak found at 755 cm^{-1} for the ^1B_b resonance (refer to Fig. 3 in [69]).

The resonance Raman study on anthracene in methanol by Efremov *et al.* presents an alternative explanation for the observed wavenumber shift.[102] They observed a small secondary peak at 786 cm^{-1} for ^1B_b excitation at 244 nm; this peak was assigned to the

first overtone of the anthracene ring-breathing mode at 387 cm^{-1}. Yet, if the observed mode here was this overtone, a puzzling aspect would arise as to why the usually much more prominent fundamental at 755 cm^{-1} is completely absent in the spectrum.

Additional peaks appear in the typically silent region of non-resonant Raman spectra at 1805 cm^{-1}, 1960 cm^{-1} and 2030 cm^{-1}, indicating that these peaks may belong to overtones or combination modes. The mode at 1805 cm^{-1} closely resembles the spectral position at 1789 cm^{-1}, which was assigned as a combination mode of a_g+b_{1g} symmetry by Holtum *et al.*.[69] Notably, this peak exhibits significant intensity in this spectrum with ^1L_a excitation compared to measurements conducted with excitation at ^1B_b.[102, 69] The origins of the other two modes in the silent region, 1960 cm^{-1} and 2030 cm^{-1}, remain unclear. The presence of the intense combination peak at 1805 cm^{-1} suggests that Herzberg-Teller vibronic coupling via the C-term could play a significant role.

For wavelength tuning, it is very useful to have a non-resonant solvent peak as an internal standard in the spectrum for intensity normalization to compare the magnitudes at different excitation wavelengths. To be able to clearly observe such a peak, measurements at a lower concentration of 1.3 mM were subsequently conducted. Furthermore, at the lower concentration, due to the squared concentration dependence of dimerization reactions, significantly fewer molecules will dimerize at this lower concentration. However, this is partially counteracted by the reduced signal, which necessitates longer measurement durations, thereby increasing exposure to UV radiation. Fortunately, the blue-shifted absorption spectrum of the generated photodimers indicates that their Raman signal is not resonantly enhanced. Hence, their influence on the Raman spectra should solely reduce the intensity of the anthracene Raman signal relative to the solvent signal.[105]

A comparison for a repeated measurement with 376 nm excitation at a concentration of 1.3 mM is presented in Fig. 3.25.

As expected, the spectrum at the reduced concentration of 1.3 mM is nearly identical to that of the 15 mM solution. However, due to the decrease in the relative signal of anthracene compared to the solvent, the solvent peak at 920 cm^{-1} becomes much more pronounced. Additionally, the asymmetric solvent peak at approximately 1380 cm^{-1} from acetonitrile now overlaps with the largest anthracene peak at 1405 cm^{-1}, resulting in a shoulder. A non-resonant measurement using the 1.3 mM anthracene sample at 410 nm, which shows only the solvent peaks, indicates that this contribution is relatively minor compared to the intensity of the anthracene Raman peak at 1405 cm^{-1} (see red curve in Fig. 3.25). The combination mode at 1805 cm^{-1} shows somewhat of a reduction in magnitude possibly due to a difference in Kerr pulse synchronization. Furthermore, the additional peaks observed near 2000 cm^{-1} are almost unobservable.

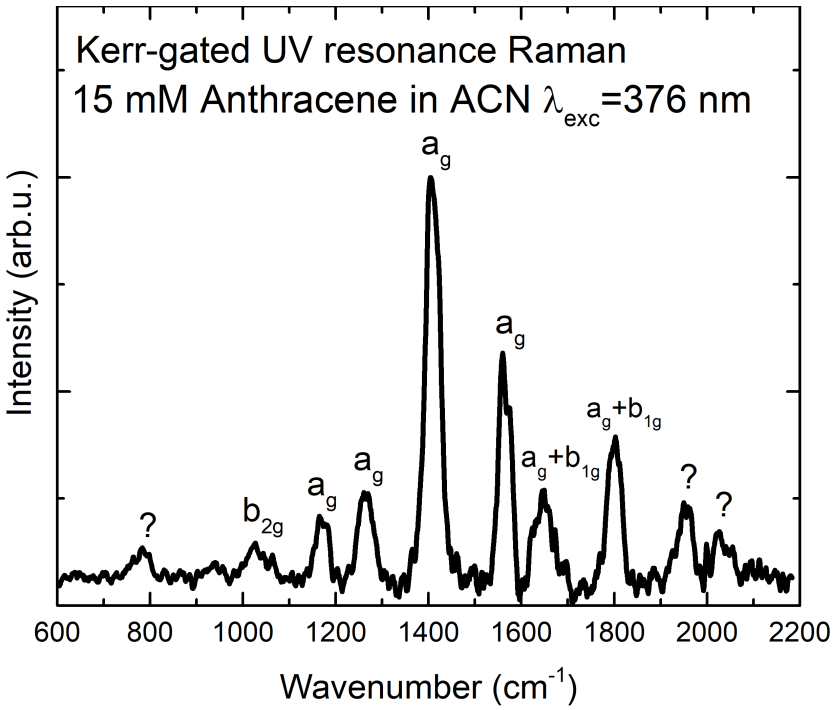

Figure 3.24: A Kerr-gated UV resonance Raman spectrum of anthracene in acetonitrile (15 mM) for a Raman excitation at $^1L_a(0-0)$ (376 nm) (integration time: 200 s). The theoretically predicted symmetries are shown as reported by Holtum *et al.* [69]. The peak positions observed within 5 cm^{-1} are: 785 cm^{-1}, 1025 cm^{-1}, 1165 cm^{-1}, 1260 cm^{-1}, 1405 cm^{-1}, 1560 cm^{-1}, 1650 cm^{-1}, 1805 cm^{-1}, 1960 cm^{-1} and 2030 cm^{-1}.

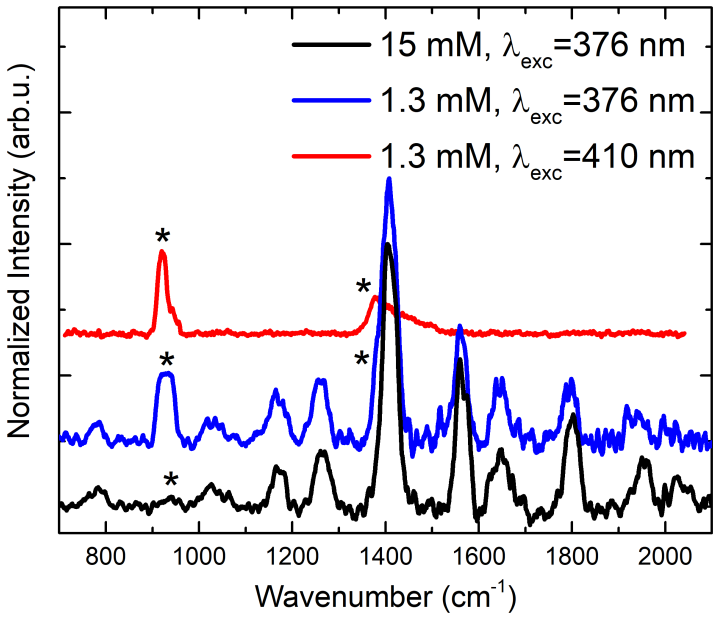

Figure 3.25: Comparison between the Kerr-gated UV resonance Raman spectra with 15 mM (integration time: 200 s) and 1.3 mM (integration time: 6000 s) anthracene concentrations in acetonitrile for laser excitation at 376 nm. Additionally, the non-resonant Raman spectrum with 410 nm excitation is shown in red, which only displays the acetonitrile solvent peaks (marked with a star).

Next, the Raman excitation profiles for the observed modes between $700-1800$ cm^{-1} were taken at the $^1L_a(0-0)$ transition with a tuning range of $366-386$ nm using the more diluted concentration of 1.3 mM. This allows using the clearly visible acetonitrile solvent peak observed at 920 cm^{-1}, which is unaffected by resonance enhancement and can thus be used for normalizing the Raman intensities. This normalization should also remove the ω^4 frequency dependency of Raman scattering to obtain values that are proportional to the transition polarizability. In these measurements, the sample solution was replaced for each measurement to retain similar anthracene concentrations and reduce the impact of photodimerization.

These subsequent measurements, are depicted in Fig. 3.26 and will undergo quantitative analysis. However, in some cases for these measurements with lower concentration acquisition times needed to be very long to obtain sufficient SNR (up to 7 hours per measurement). As a result, the measurement I_{leak} was omitted. Instead, this value was set to the dark counts of the CCD (ca. 600 counts), and only two measurements ($I(0$ ps) and $I(3$ ps)) were collected. Integration times varied between 6000 s (1 h and 40 min) up to 24000 s (6 h and 40 min) depending on the available signal which may have impacted the concentrations for each measurement due to additional photodimerization.

The Raman excitation profiles were deduced by extracting the intensity (peak height) of each anthracene Raman peak utilizing a Gaussian fit and normalizing these to the maximum measured intensity in the tuning series. In addition for the Raman excitation profile of the peak at 1405 cm^{-1}, the solvent signal from the overlapping acetonitrile peak at the same wavenumber position was subtracted, employing the non-resonant measurement at 410 nm. The resulting profiles are depicted alongside a normalized absorption spectrum (dashed) in Fig. 3.27 for analysis.

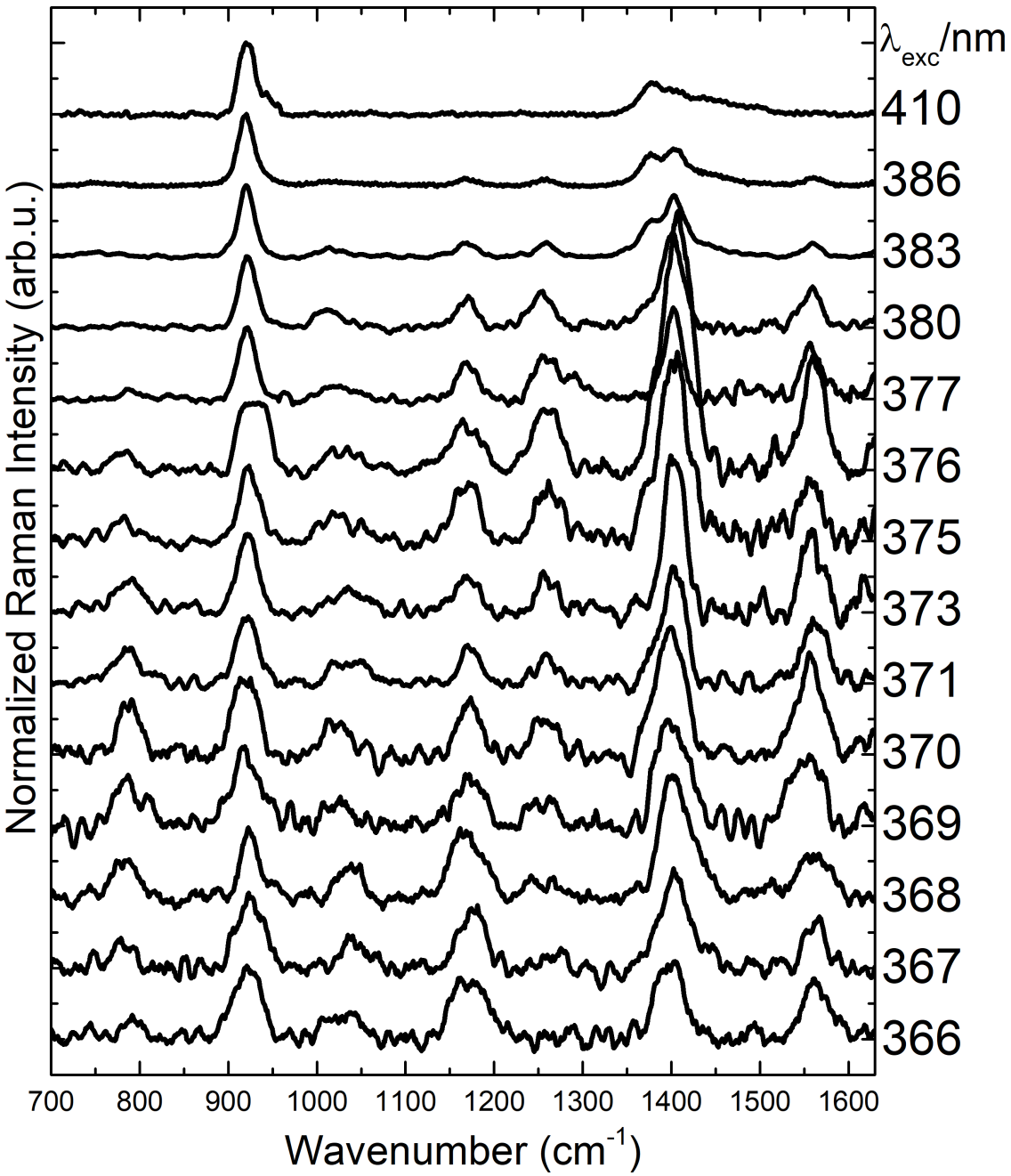

Figure 3.26: Resonance Raman spectra of anthracene (1.3 mM in acetonitrile) recorded at the resonance $^1L_a(0-0)$ between $366-386$ nm, the corresponding excitation wavelength in nanometers is shown on the right side next to each spectrum. The non-resonant spectrum with 410 nm Raman excitation is additionally included at the very top. Measurements were conducted with 6000-24000 s (100 - 400 min) integration time. Prior to each measurement, the sample solution was replaced.

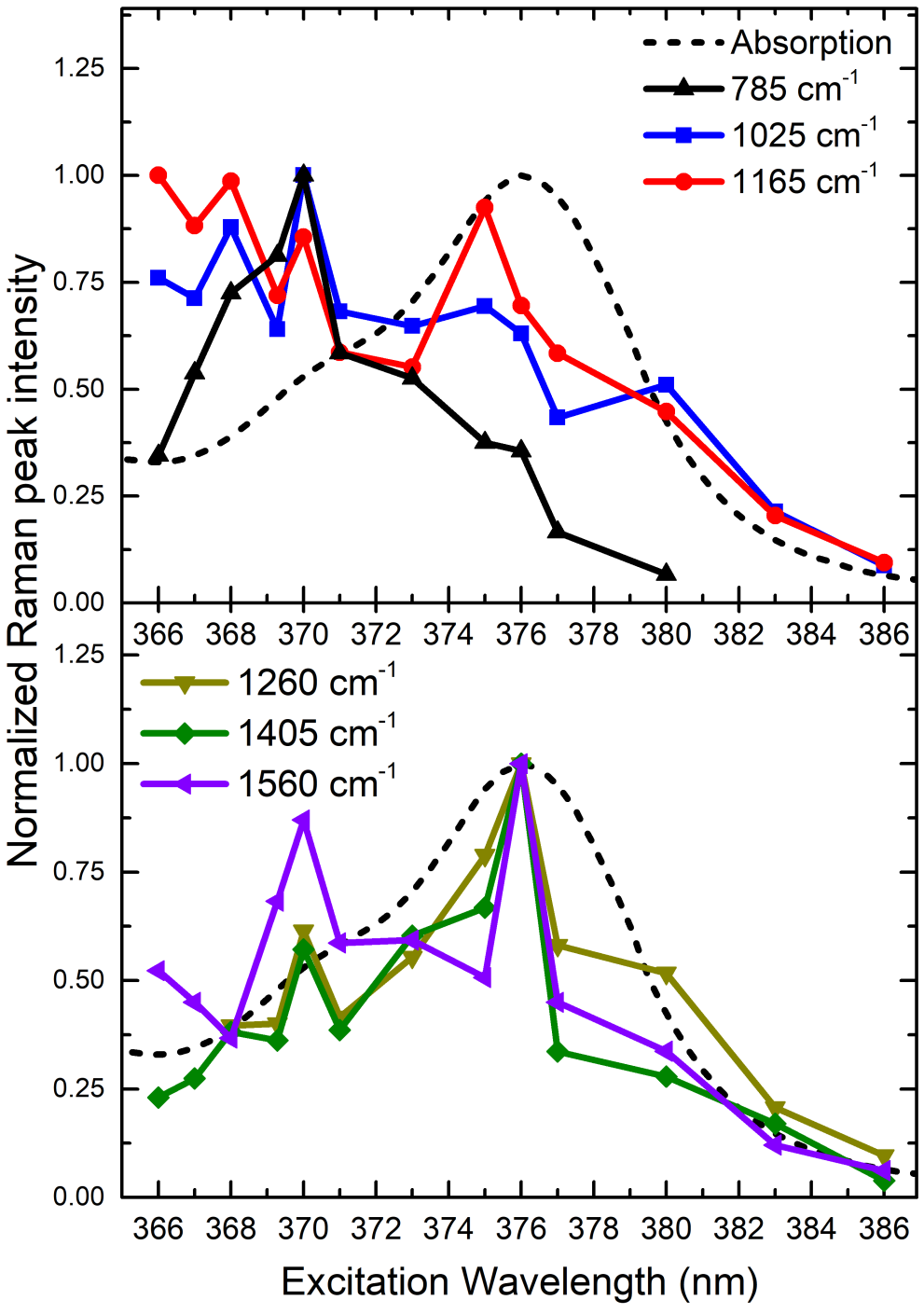

Figure 3.27: Raman excitation profiles of six modes of anthracene at the $^1L_a(0-0)$ band. The profiles were derived by normalizing the peak heights from the Raman spectra depicted in the tuning series in Fig. 3.26. The profiles are shown alongside the normalized absorption spectrum of anthracene in acetonitrile (dashed black).

Firstly, the two peaks corresponding to totally symmetric a_g Raman modes, at 1260 cm^{-1} (yellow in the bottom part of figure) and 1405 cm^{-1} (green), exhibit Raman excitation profiles roughly correlated to the absorption spectrum. The correlation to the absorption spectrum particularly seen after the intensity peak at 376 nm is possibly due to A-term scattering on the ^1L_a band. Additionally, most profiles except for the peak at 1165 cm^{-1} (red) demonstrate an additional intensity peak around 370 nm, corresponding to a minor shoulder in the absorption spectrum. This observation is most notable for the Raman peak at 785 cm^{-1} (black), which solely exhibits this intensity peak. Furthermore, the Raman peak at 1025 cm^{-1} (blue) belonging to a non-totally symmetric mode b_{2g}, appears to increase with shorter wavelength excitation without any significant intensity peaks. The fluctuating profile of this peak can be attributed to its relatively low magnitude, resulting in a low signal-to-noise ratio. Given that this Raman peak belongs to a non-totally symmetric vibration, it is likely unable to acquire intensity through A-term or C-term scattering which may be responsible for the intensity peaks in other profiles since these terms only include the electronic transition dipole moment of a single electronic state as a pre-factor. The mode corresponding to this peak, as well as the peak originating from the totally symmetric modes at 1165 cm^{-1}, likely derive intensity from higher excited states below the shortest wavelength utilized in the tuning series (366 nm).

The peak in Raman intensity below the absorption maximum at 370 nm, particularly for the Raman peak at 785 cm^{-1}, which completely disappears below 380 nm, implies the presence of an additional excited state at 370 nm that is not clearly visible in the absorption spectrum. One plausible explanation is that this state corresponds to the forbidden ^1L_b state known to exist in anthracene. Here, there would need to be a selection rule at play, necessary to explain the disparity between the profile of the Raman peak at 1405 cm^{-1}, which only peaks at 376 nm and that for the Raman peak at 785 cm^{-1} which only peaks at 370 nm.

Another potential explanation is that the 785 cm^{-1} Raman peak could be attributed to a different molecule, perhaps the anthracene dimer. However, based on the Raman excitation profiles of other Raman peaks, it appears that all of anthracene's totally symmetric modes particularly the 1560 cm^{-1} Raman peak, are enhanced at 370 nm, which makes this interpretation less probable.

A-term scattering by itself may be insufficient to fully explain the excitation intensity profile of the 785 cm^{-1} peak since there appear to be at least two contributions one that is broad at wavelengths above 371 nm and one that is sharp below. A possible interpretation that explains the broad contribution seen below 370 nm is that there are additional vibronic B-term transitions between the ^1L_a and ^1L_b bands.

The signal increase of the 785 cm^{-1} peak may be even more significant if reabsorption of the Raman-scattered light inside the sample were to be taken into account. For instance, under 366 nm excitation, the Raman peak at 785 cm^{-1} is clearly affected by reabsorption from the anthracene sample due to its Raman signal wavelength at 376 nm which should reduce its intensity. The same, however, should apply similarly to the adjacent internal reference acetonitrile peak at 920 cm^{-1}; for this reason, the Raman excitation profile of the 785 cm^{-1} peak should be reflected well. However, other modes at higher wavenumbers may become overestimated for shorter wavelengths. For instance, the slight elevation of the Raman peak at 1560 cm^{-1} under excitation below 368 nm could be attributed to reabsorption.

To analyze the impact of reabsorption, fluorescence measurements were conducted for a greatly diluted concentration of 0.1 mM. According to the Beer-Lambert law, by reducing the concentration by a factor of ca. 10, transmittance through the sample increases by $e^{10-1} \approx 8000$, thus for this significantly diluted concentration reabsorption of fluorescence can be disregarded.

Figure 3.28 illustrates a comparison of fluorescence signals between the diluted anthracene sample and the reference I(3 ps) (1.3 mM) at two wavelengths (366 nm and 380 nm). It's noteworthy that the diluted sample spectra were acquired by only slightly adjusting the analyzer polarizer of the Kerr gate off perpendicular (opening the Kerr gate) to facilitate a good comparison with the fluorescence observed in the Kerr-gated Raman measurements. As expected at 380 nm, the fluorescence spectra exhibit substantial overlap, indicating that reabsorption has negligible impact on the relative magnitudes of the resonance Raman spectra. Conversely, at 366 nm, a slight difference between the spectra is observed. However, the spectra remain comparable, likely since excitation was conducted at the very edge of the cuvette toward the collection lens, thereby minimizing the re-absorption path length.

Finally, to investigate the possibility that the Raman peaks at 1260 cm^{-1},1405 cm^{-1}, 1560 cm^{-1} and possibly also 1165 cm^{-1} representing totally symmetric modes, exhibit significant resonance Raman scattering of Franck-Condon type (A-term) under ^1L_a excitation, a polarization-resolved Raman measurement was conducted at 381 nm. The choice of employing 381 nm as excitation wavelength is motivated by the lower likelihood of vibronic coupling with higher excited states when compared to shorter wavelength excitation.

Obtaining the depolarization ratio should only require the use of a half-wave plate (B-Halle 300-470 nm achr. L), to rotate the excitation beam polarization into the perpendicular position. However, my search across the literature yielded no instances of this combination

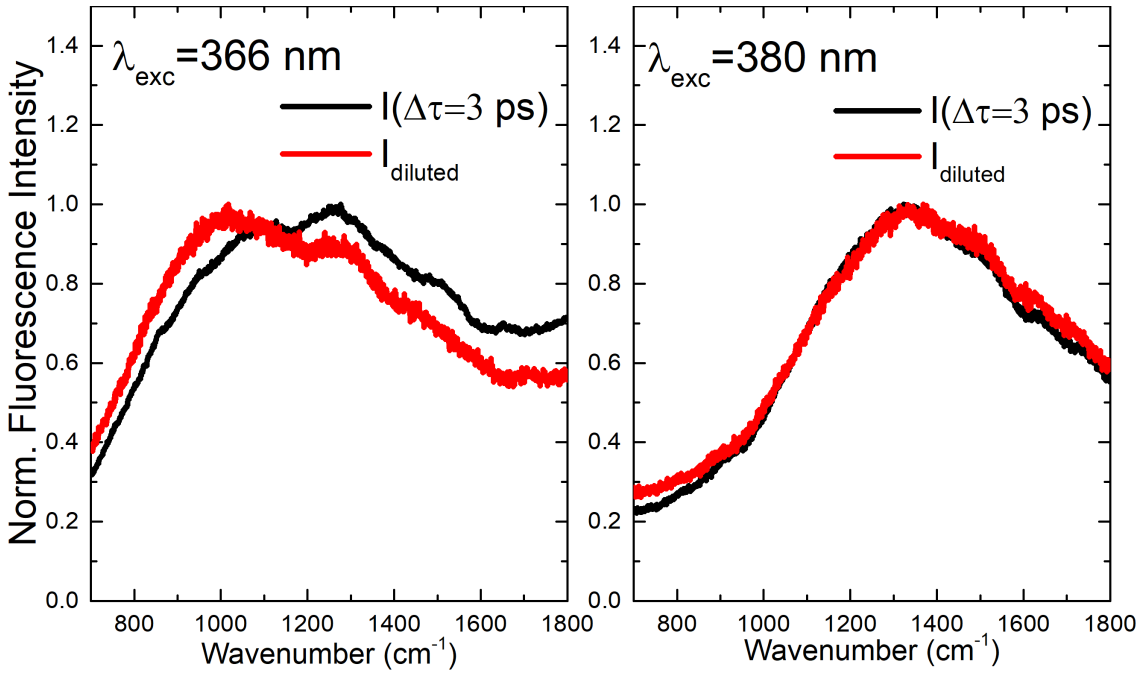

Figure 3.28: Comparison of normalized fluorescence spectra between a diluted anthracene sample (red) and the reference utilized for extracting the resonant Raman signal $I(3\text{ ps})$ under two excitations: 366 nm (left) and 380 nm (right).

being utilized. Therefore, an initial test measurement was conducted, as illustrated in Fig. 3.29, using cyclohexane to validate the capability of performing polarization-resolved measurements utilizing a Kerr gate.

The measurement reveals the three known depolarized modes at 1025 cm^{-1}, 1270 cm^{-1} and 1460 cm^{-1}, exhibiting depolarization ratios close to the expected value of 0.75.[106] Furthermore, the extinction of the single polarized mode at 802 cm^{-1} is also observable for perpendicular polarization of the Raman excitation.

The polarization-resolved resonance Raman measurements of anthracene, at an excitation wavelength of 381 nm for both parallel and perpendicular polarizations, are shown in Fig. 3.30.

The calculated depolarization ratios, derived from the Raman peak heights from Gaussian fits, are indicated above each peak. As anticipated, the acetonitrile polarized band at 920 cm^{-1} is nearly absent under perpendicular excitation.[107]

For A-term scattering in anthracene, a depolarization value of $\rho = 1/3 \approx 0.33$ is expected since the electronic resonance for the ^1L_a state only occurs over a single axis.[52, 108] Interestingly, all Raman peaks corresponding to vibrational modes with a_g symmetry approximately exhibit this value, notably 1165 cm^{-1} (ρ =0.3), 1260 cm^{-1} (ρ =0.35), 1405 cm^{-1} (ρ =0.34) and 1560 cm^{-1} (ρ =0.27).

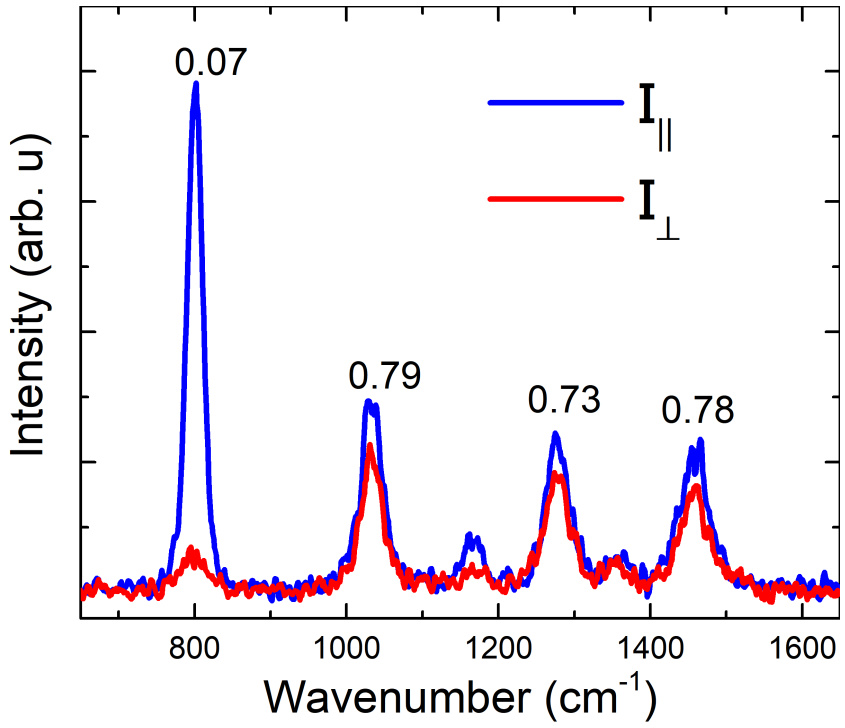

Figure 3.29: Depolarization measurements carried out on cyclohexane to evaluate the efficacy of employing the Kerr gate in depolarization measurements. The Raman signal under parallel polarized excitation ($\lambda_{exc} = 381$ nm) is depicted by the blue curve, while the signal under perpendicular excitation is represented by the red curve.

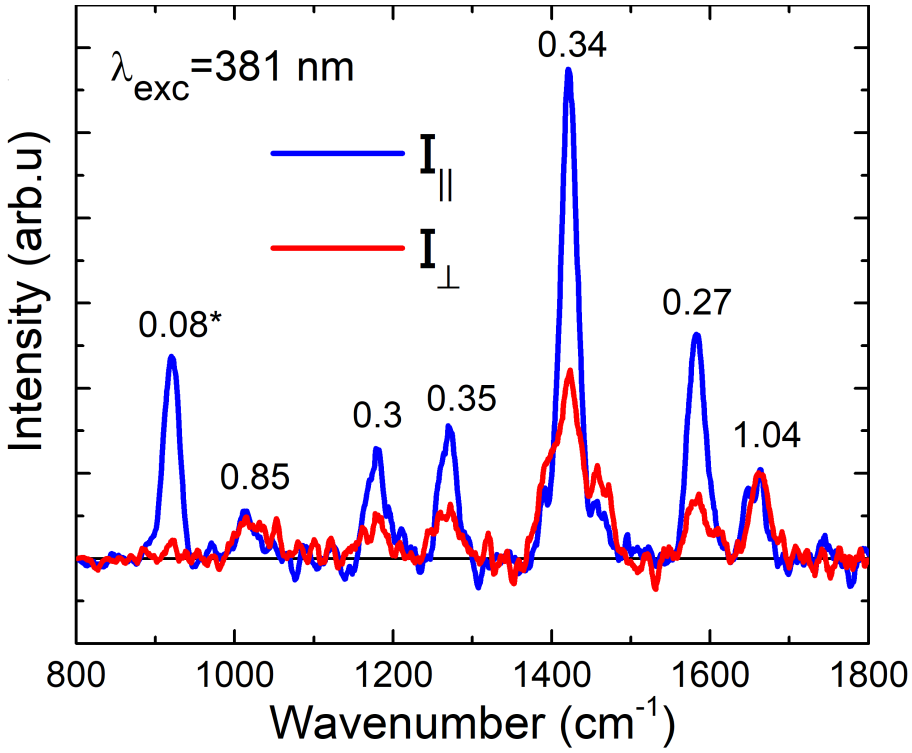

Figure 3.30: Kerr gate resonance Raman spectra of anthracene in acetonitrile (1.3 mM) with $\lambda_{exc} = 381$ nm obtained using excitations with either parallel (blue) or perpendicular (red) polarization, to determine Raman depolarization ratios.

Two modes that clearly deviate from this criterion are those at 1025 cm^{-1} and 1650 cm^{-1}, displaying depolarization ratios close to unity (0.85 and 1.04). The former being a b_{2g} mode and the latter an $a_g + b_{1g}$ combination mode, are therefore expected not to exhibit A-term scattering. Their depolarization ratios exceeding 0.75 are not atypical in resonance Raman scattering with vibronic coupling and signify antisymmetric tensor properties.[52]

These polarization-resolved UVRR measurements also underscore the necessity to include the depolarization ratio in theory when comparing Kerr-gated Raman data to simulated Raman magnitudes. These magnitudes can be derived either through summing over vibrational levels as was described in the theoretical section or by employing the typically more effective time-domain approach using TDDFT.[109]

3.2.1 Conclusion: Resonance Raman Study of the Anthracene ^1L_a state

The application of the Kerr gate fluorescence suppression technique has enabled the observation of resonance Raman scattering in the first vibronic transition of the ^1L_a state of anthracene (in acetonitrile) with excitations ranging between $366 - 386$ nm. For at least two Raman peaks representing totally symmetric a_g modes at 1260 cm^{-1} and 1405 cm^{-1} the Raman magnitudes are maximized at the anthracene $^1L_a(0-0)$ absorption maximum (376 nm) which might indicate Franck-Condon (A-term) resonance Raman scattering with the ^1L_a state. However other modes feature an additional maximum at 370 nm.

Most notably a Raman excitation profile largely uncorrelated from the absorption spectrum is seen for a peak observed at approximately 785 cm^{-1}. The intensity of this Raman peak sharply increases at 370 nm, well below the anthracene absorption maximum at 376 nm. This peak may correspond to a totally-symmetric a_g ring breathing mode of anthracene previously reported at 760 cm^{-1}.[102, 69] The spectral resolution in these measurements was possibly compromised due to the extensive fluorescence removal necessary, potentially causing a shift in wavenumber positions. Alternatively to explain the wavenumber shift this Raman peak may actually correspond to the first overtone of another anthracene ring-breathing mode previously seen at 786 cm^{-1}.[102]

One possibility is that this Raman peak gains intensity only through interactions with the negligibly absorbing state ^1L_b while Franck-Condon transitions to the ^1L_a band are forbidden. This interaction could proceed directly through A-term transitions over ^1L_b or alternatively via the C-term over ^1L_a , both of which would not include the electronic transition dipole moment of the ^1L_a band as a pre-factor.

In gas-phase molecular spectroscopy, the ^1L_b band of anthracene is anticipated to be approximately 4.5 nm blue-shifted compared to ^1L_a.[110] This distance in wavelength is comparable to the 6 nm-shifted Raman excitation profile of the 785 cm^{-1} Raman peak in this study. The observation that the vibrational mode corresponding to the 785 cm^{-1} Raman peak has a strong interaction with the ^1L_b state would be in line with supersonic jet-cooled fluorescence measurements on anthracene, which showed that the ring-breathing mode detected at 748 cm^{-1} in anthracene, in addition to all other a_g detected modes with lower wavenumbers (232 cm^{-1} and 540 cm^{-1}), possess an extended radiative lifetime in fluorescence.[111] This was interpreted by Zilberg *et al.* as an indication of coupling to a long-lived more forbidden state.

A possible explanation for a potential selection rule effect between different vibrational modes interacting with distinct electronic states can be found in a prior computational in-

vestigation conducted by Chen *et al.*.[112] They assessed the difference of energy between the equilibrium ground state geometry upon initial excitation and that of the equilibrium excited state geometry, denoted as $\lambda = E_n(Q_0^{eq}) - E_n(Q_n^{eq})$, for each normal mode in naphthalene. This energy difference, known as reorganization energy, is linked to the vibronic coupling strength. The study revealed that a ring-breathing mode at 792 cm^{-1} is unique whereby reorganizational energy predominates for the^1L_b state, in contrast, most other normal modes, particularly the C-C stretching modes, display large reorganization energies for the ^1L_a state. Though a similar normal mode decomposition was not performed for anthracene, it's noteworthy that these calculated reorganization energies exhibit a pattern that could explain the Raman excitation profiles observed in this study. In this explanation, linking variations in observed Raman intensity to vibronic coupling strength discrepancies for vibrational modes, it appears that the spikes in the Raman excitation profiles are more plausibly attributed to C-term Raman scattering contributions rather than A-term contributions which should be independent to vibronic coupling. Given the known significance of the C-term, especially in relation to the first overtone of Raman modes for excitation with forbidden states, this appears reasonable.[51]

For the exact $^1L_a(0-0)$ resonance condition at 376 nm excitation, the combination mode $a_g + b_{1g}$ recorded at 1805 cm^{-1} was observed. Additionally, two unknown Raman peaks, possibly representing further combination modes or overtones, were observed at 1960 cm^{-1} and 2030 cm^{-1}.

An increase in Raman intensity for shorter wavelengths is observed for the Raman peak at 1025 cm^{-1}, representing a mode of b_{2g} symmetry (C-H bending).[69] The intensity of this peak is likely derived from B-term transitions involving vibronic coupling with even higher excited state(s) than ^1L_b. This could occur over the strongly allowed but energetically much more distant ^1B_b (B_{1u}) state.

In the wavenumber range between $800 - 1800$ cm^{-1} the resonance Raman depolarization investigation with excitation at the longer wavelength side of the $^1L_a(0-0)$ resonance (381 nm) showed that all a_g assigned Raman peaks seen for 381 nm excitation namely, 1165 cm^{-1}, 1260 cm^{-1}, 1405 cm^{-1} and 1560 cm^{-1} have depolarization ratios close to the expected value of 1/3 for Franck-Condon resonance Raman scattering. On the other hand, the Raman peaks at 1025 cm^{-1} and 1650 cm^{-1} exhibited depolarization values near unity.

3.3 Heterodyne CARS-ROA of Pinene and MOM-BINOL

The first goal in the heterodyne CARS-ROA experiments was to validate our setup, which differs in several aspects from the one shown by Hamaguchi and co-workers [80, 81], the CARS-ROA experiments with both β-pinene enantiomers were initially replicated.

A major deviation in our set-up was the significantly shorter femtosecond Stokes pulse duration, contrasted with the picosecond white light pulse utilized by Hamaguchi and co-workers. These shorter pulses lead to higher peak powers, despite lower average powers being employed. In the subsequent experiments, average powers fluctuated but typically remained between 1-3 mW for the pump and 5-10 mW for the Stokes pulse. This yields a maximum fluence of approximately 0.25 $\frac{J}{cm^2}$ and peak power density of $\sim 5 \cdot 10^3$ $\frac{GW}{cm^2}$ at the sample. Conversely, Hamaguchi and co-workers employed a combined pump and Stokes power of 120 W, with a 25 kHz repetition rate and a 400 ps pulse duration, which leads to a higher fluence of ca. $2\frac{J}{cm^2}$ yet a substantially lower peak power of ~ 5 $\frac{GW}{cm^2}$. Generally, higher peak intensities in the Stokes pulse are advantageous for measuring CARS since the signal increases linearly with intensity; however, it is important to consider the potential involvement of additional interfering nonlinear effects. Another difference is that the NOPA-generated Stokes pulse in our setup is much less spectrally uniform than that of white light (see Fig. 3.31). Therefore, the CARS-ROA data should ideally be divided with a four-wave-mixing reference without Raman resonances (such as water). This division allows a better comparison of the magnitudes of Raman peaks with that of linear ROA spectra.

After conducting several initial tests with β-pinene, the heterodyne-detected CARS-ROA technique was then applied to the chiral compound MOM-BINOL, which is the precursor of a chiral organocatalyst, dissolved in a DCM solution. Many key results of this study on CARS-ROA have been published in a recent manuscript from our group.[15]

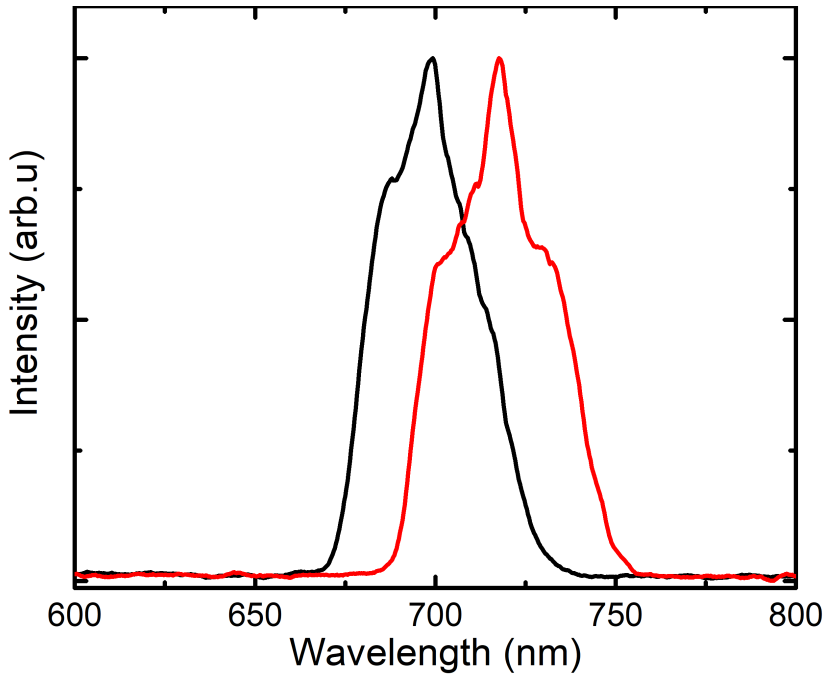

Figure 3.31: The NOPA-generated Stokes pulse spectra for $\lambda_{Stokes} = 700$ nm (black) and $\lambda_{Stokes} = 720$ nm (red). The FWHM is 35 nm and 39 nm, respectively; this corresponds to a CARS wavenumber range of 725 cm^{-1} and 750 cm^{-1} with $\lambda_{pump} = 670$ nm.

3.3.1 Enantiomers of β-pinene

The two pinene enantiomers are examined with the Stokes pulse tuned to ca. 710 nm, allowing for the detection of the three largest known forward-scattering CARS peaks at 640 cm^{-1}, 716 cm^{-1} and 765 cm^{-1}.[80] Figure 3.32 displays the two CARS measurements with the analyzer positions at $\theta_1 = \pm 0.35$, including the difference spectrum, i.e., the heterodyne-CARS-ROA spectrum. Notably, the acquisition time for each of the two subtracted spectra was only 5 seconds. As anticipated, the difference spectrum exhibits a bisignate ROA signal. It is also evident that most of the CARS-NRB is being canceled out.

The top section of Fig. 3.33 shows the raw CARS-ROA spectra of both enantiomers under nearly the same measurement conditions. Unfortunately, the magnitudes for each peak of the enantiomers differ significantly, however, the signs are opposite. In particular for (+)-β-pinene the non-resonant background signals did not cancel out completely, however, since this background does not contain any sharp features it could be simply manually background subtracted using a spline function. The background likely originates from ORD as was previously reported by Hamaguchi *et al.*.[81] The corrected spectra are shown in the bottom section of Fig. 3.33.

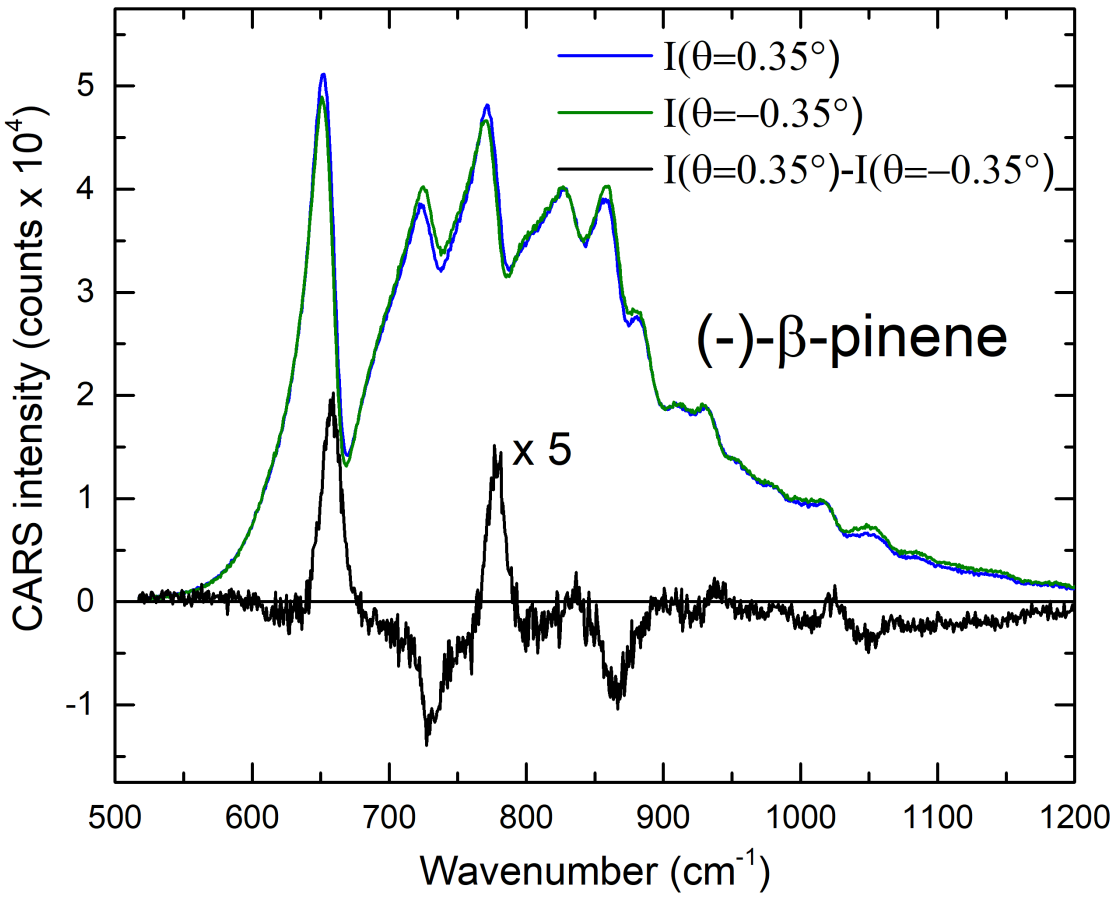

Figure 3.32: CARS spectra (blue and green) of pure liquid (-)-β-pinene. The CARS-ROA difference spectrum is depicted in black ($\theta_1 = 0.35°$, $\lambda_{pump} = 670$ nm, $\lambda_{Stokes} = 710$ nm).

While the measurement procedure for obtaining the above CARS-ROA spectra of pinene was in principle straightforward, in many measurement attempts the alternating signs of the pinene ROA signal were attenuated or even reversed in sign. Sometimes the correct ROA signature would no longer be visible in a measurement taken only a few minutes afterwards.

Subsequently, it was tested if the experiment was sensitive to the focusing condition, for example, by interference from four-wave-mixing of the cuvette glass walls. However, in measurements where the focus was set to the forward or backward part of the sample in the 2 mm cuvette, no overall change in lineshape was observed in the CARS-ROA spectrum (see Fig. 3.34).

In the end, the most likely suspect for the inconsistencies were spatial variations in the cuvette-wall material. The fused silica cuvettes from Hellma Optik (100-QS, 100-2-40) with the beam centered in the lower center portion of the cuvette appeared to perform the most consistently. One effect that may disrupt the measurements is strain birefringence.

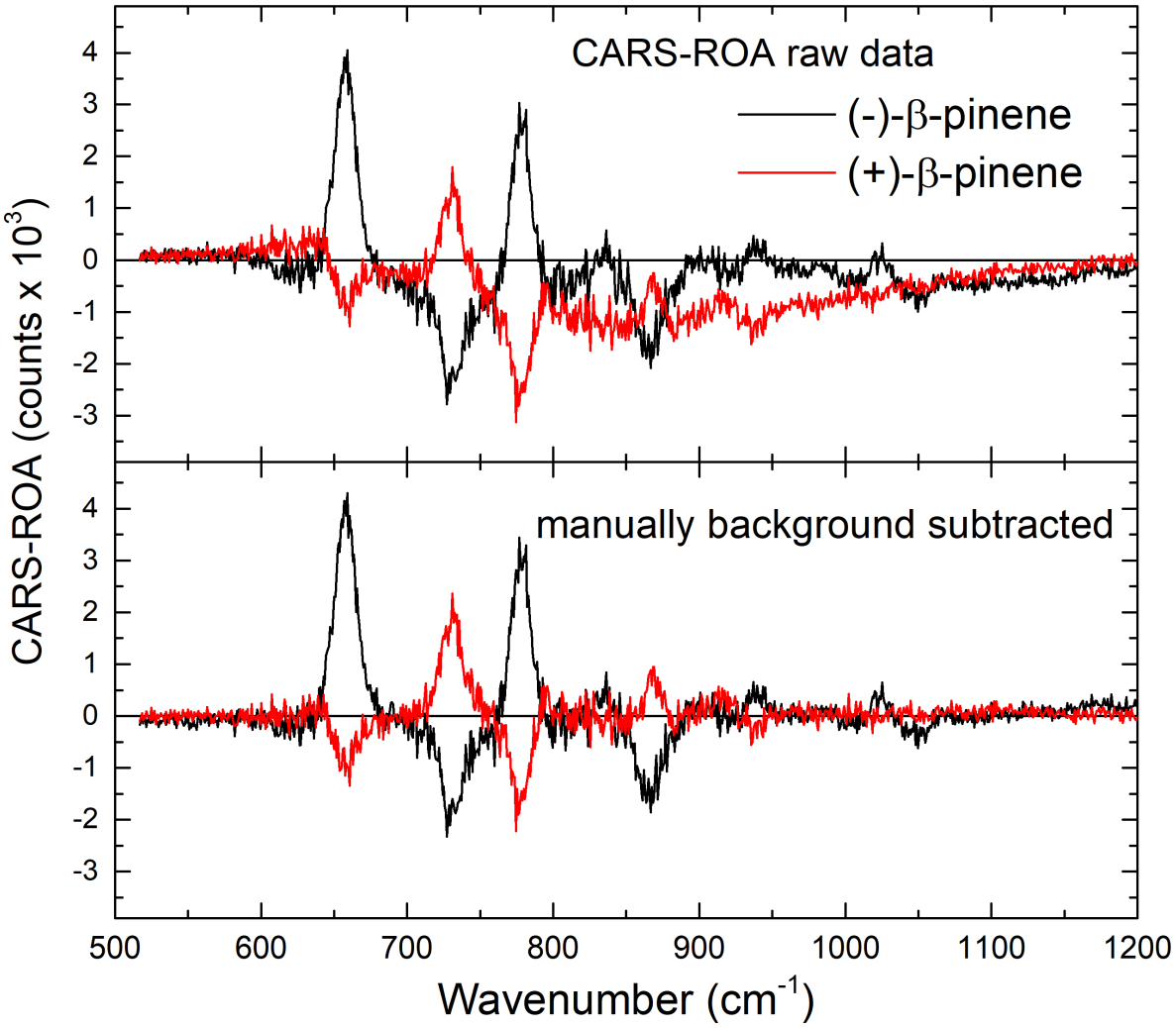

Figure 3.33: The CARS-ROA spectrum of both (-)-β-pinene (black) and (+)-β-pinene (red). Top section: "Raw" pinene CARS-ROA spectra showing a small hilly background. The bottom section shows the same spectra after manual background subtraction.[15]

Strain birefringence by its spatial variation could rotate the pump and Stokes beams and scramble their polarization.[113] It may also be that the wall material has other internal variations which could lead to problems. One potential solution to avoid this potential effect is to use cuvettes with exceptionally thin walls ($<$ 1 mm).

Next, the effect of the analyzer angles on the signal was examined. Figure 3.35 shows the successful measurements of β-pinene (-) with sets of three angles closer and farther from the polarizer extinction angle. The CARS-ROA signal increases greatly for the larger angle of $\theta = \pm 0.6°$.

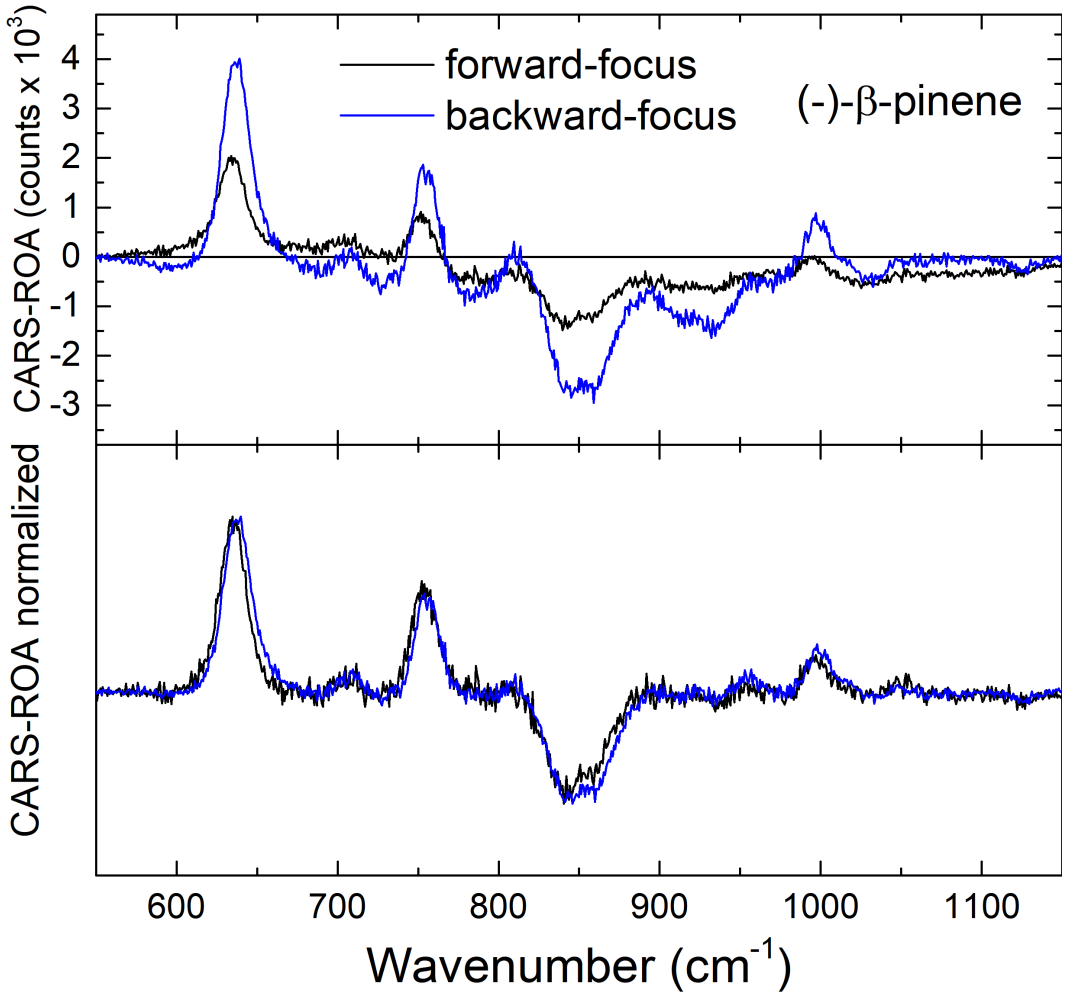

Figure 3.34: CARS-ROA spectrum of (-)-β-pinene for two focus positions inside the sample volume (in "forward focus" the focus was set closer towards the analyzer inside the cuvette). The upper spectra depict the raw CARS-ROA spectra and the lower spectra have undergone additional background subtraction and normalization. The lower spectra show that no change in the lineshape can be observed. Note that in this case the magnitude of the 716 cm^{-1} peak which should have a negative ROA sign is only attenuated.

Since $sin(2\theta) \simeq 2\theta$ under the small-angle approximation, a linear increase in signal is anticipated. This seems to hold true (see right side of Fig. 3.35), except for the 640 cm^{-1} peak at $\theta = \pm 0.6°$, which appears to be an outlier as it is notably broadened.

It also appears that the ROA peaks shift somewhat toward higher wavenumbers for the largest angle set; this effect may be due to a spatial shift of the anti-Stokes beam on the spectrometer slit from refractive displacement by the analyzer polarizer. The range of θ values at which the achiral signal overwhelms the chiral signal was not investigated. Identifying the maximum angle sets is a straightforward route to increase the signal.

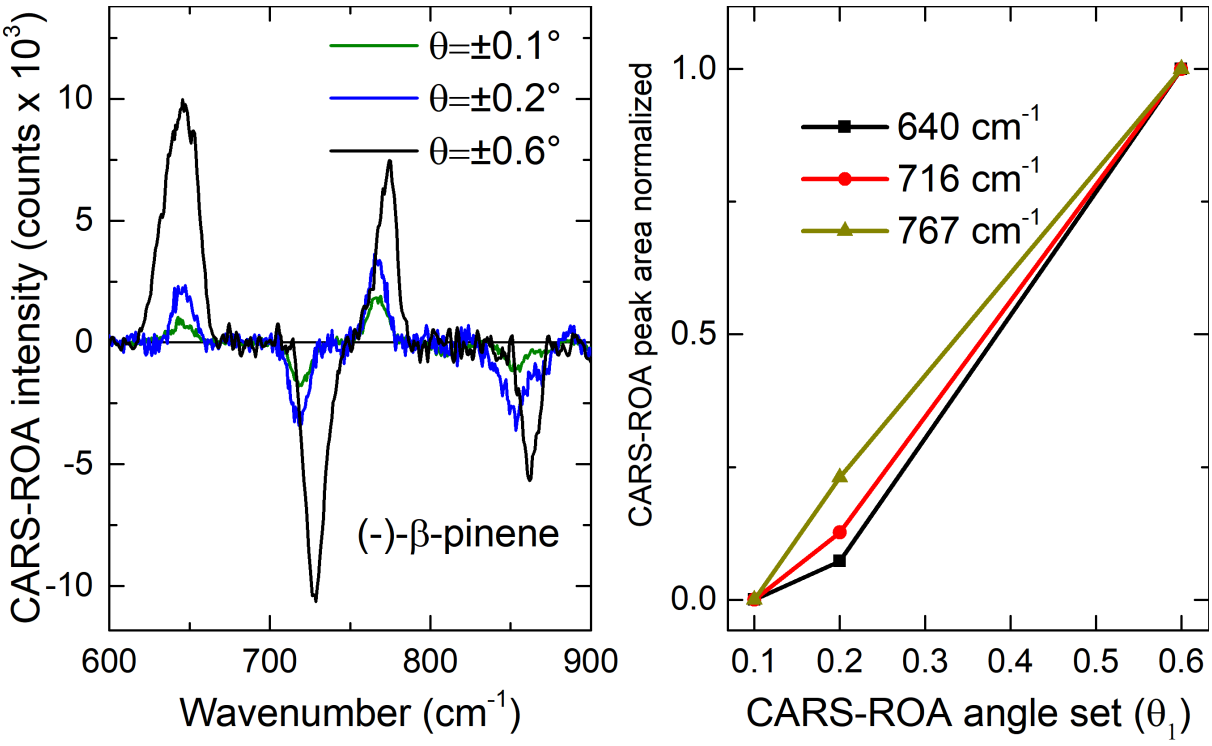

Figure 3.35: CARS-ROA spectra of β-pinene(-) for different analyzer angle sets.

Critical for numerous applications is the capability to detect the ROA signal in instances where the sample is diluted in an achiral solvent or when multiple chiral samples are involved. Therefore additional measurements were carried out in which (-)-β-pinene was mixed with acetone, ethanol and diethylether to yield a very high concentration of 3.2 M (50% v/v). An intuitive assumption is that the achiral solvent has minimal influence on the spectrum, primarily diminishing the signal as the concentration of the chiral component decreases. However, in this heterodyne CARS-ROA experiment, the detected signal is always a combination of chiral and achiral CARS contributions. Therefore, the achiral solvent itself also acts as a local oscillator. Hence, the solvent signal can enhance the chiral signal, but potentially could also cause artifacts in heterodyne CARS-ROA when diluted. The diluted spectra that were measured are displayed in Fig. 3.36. The concentrations converted to mole fractions are 32% for acetone, 27% for ethanol and 40% for diethylether. The spectra of pinene in acetone and ethanol both exhibit monosignate pinene peaks with the opposite sign of that of pure (-)-β-pinene. For acetone and ethanol, the solvent Raman peaks at 770 cm^{-1} cm and 880 cm^{-1} become prominently visible in the CARS-ROA spectrum.

The spectrum with diethyl ether more closely resembles the original ROA of pure pinene since the 640 cm^{-1} and 765 cm^{-1} peaks have the correct sign and the 716 cm^{-1} peak is significantly attenuated. This could be attributed to the slightly larger mole fraction for the chiral compound or the absence of significant Raman peaks of diethyl ether within the measured wavenumber range.

Another aspect of the measurements was that the CARS-ROA signal of pinene solutions showed a similar or higher magnitude in comparison to measurements of pure pinene. This could indicate, as previously mentioned, that a portion of the signal likely arises from a new interfering heterodyne term between the two components. However, additional measurements are required to eliminate possible experimental variabilities. Furthermore, it would have been quite intriguing to observe whether the monosignate peaks, especially those for pinene diluted in ethanol, would be reversed in (+)-β-pinene.

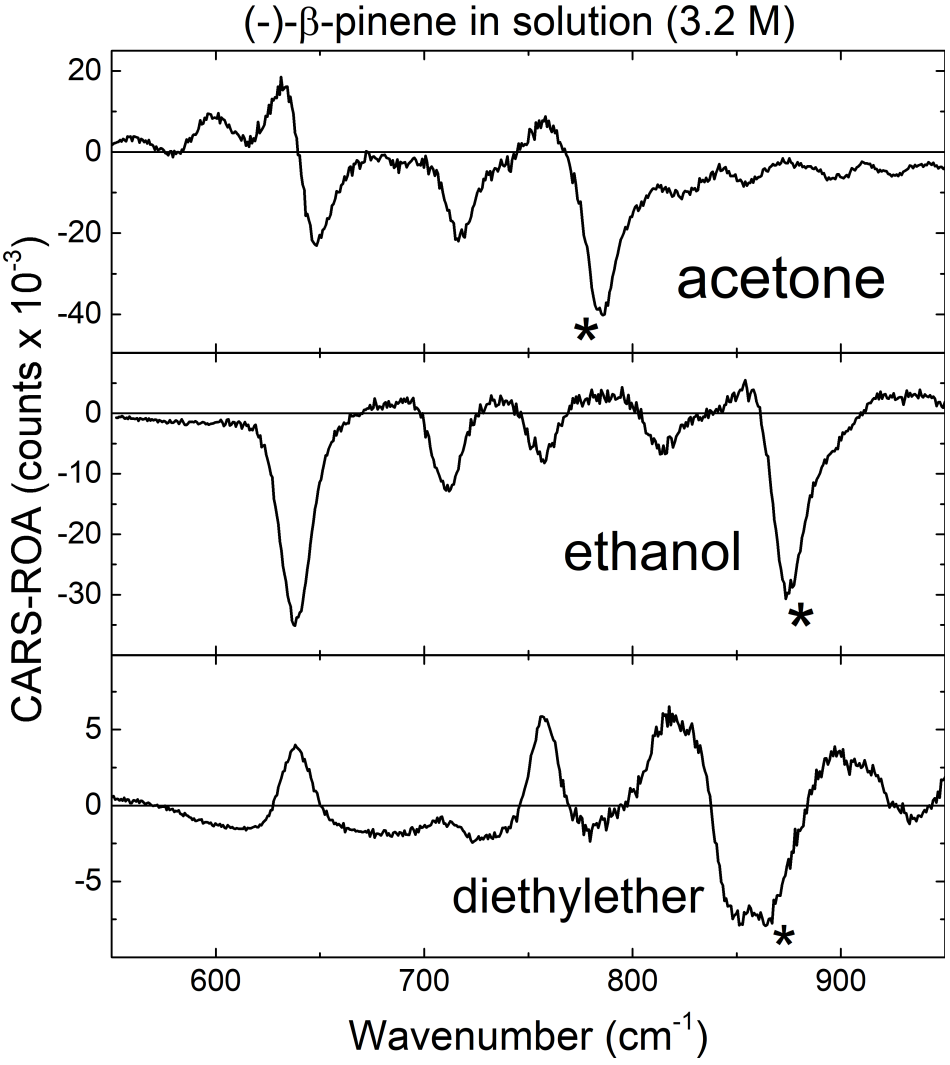

Figure 3.36: CARS-ROA spectra of (-)-β-pinene diluted in acetone (top), ethanol (middle) and diethylether (bottom). The star indicates solvent peaks.

3.3.2 Enantiomers of MOM-BINOL

CARS-ROA may be applied to observe chiral reactions. As a model compound we selected the precursors of a chiral organocatalyst. Methoxymethyl-1,1´-Bi-2-naphthol (MOM-BINOL) is derived from BINOL, a very cost-effective chiral compound, and exhibits axial chirality. Its enantiomers are designated as R and S, wherein the orientation of its two linked naphthalene groups are twisted in opposite directions (see Fig. 3.37).

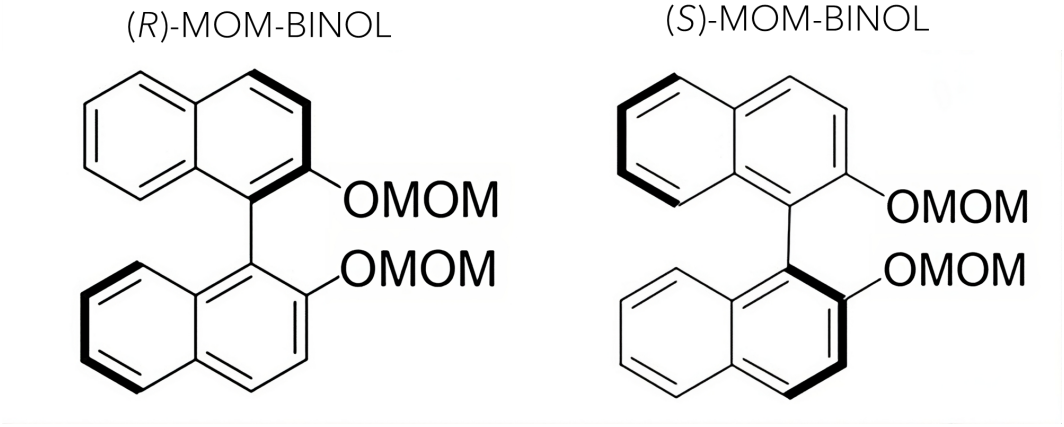

Figure 3.37: The structures of the two enantiomers of MOM-BINOL exhibiting axial chirality.[15]

To minimize the solvent's complicating effects, as discussed in the preceding section, a highly concentrated solution using the solvent DCM was prepared (1.5 g of MOM-BINOL in 2 ml DCM, equivalent to 2 M).

Figure 3.38 displays the measured (background-subtracted) CARS-ROA spectra of both R and S enantiomers of MOM-BINOL in the fingerprint region in blue and green. Both enantiomers exhibit monosignate peaks of which the signs mirror each other for five Raman peaks (710 cm^{-1}, 1020 cm^{-1}, 1150 cm^{-1}, 1240 cm^{-1} and 1380 cm^{-1}). Monosignate peaks of similar positions can also be observed in conventional ROA measurements, wherein the three corresponding Raman peak positions are detected at 1017 cm^{-1}, 1147 cm^{-1}, and 1374 cm^{-1}.[15] The observed peaks also seem to align with the expected positions, although the resolution of the spectra was insufficient to provide an accuracy greater than ± 5 cm^{-1}. For one outlier at 860 cm^{-1} where the peaks do not mirror each other in sign, it is likely that the measurement for (R)-MOM-BINOL was incorrect for this wavenumber range. Furthermore peaks at 710 cm^{-1}, 1120 cm^{-1} and 1380 cm^{-1} are somewhat wavenumber-shifted between the enantiomers; this behavior further diminishes the spectral accuracy of the experiment.

As an important supplement, the CARS-ROA spectrum of the achiral DCM solvent spectrum is shown in black. This solvent spectrum does not show significant peaks except for a minor contribution at 1030 cm^{-1}; notably, DCM already lacks Raman modes of significant oscillator strength in the measured fingerprint range. For this reason, the DCM spectrum is mostly composed of four-wave-mixing and is therefore further used as a reference to remove the slightly asymmetric Gaussian shape of the Stokes spectrum in order to normalize the peak magnitudes.

The right side of Fig. 3.39 shows the same spectra of MOM-BINOL divided by the DCM FWM signal. For the division, a 201 pts Savitzky-Golay smoothing filter was applied on the DCM CARS spectrum (black curve on the left side) in order to smooth out the minute Raman resonances (red curve on the left side). The divided spectra show that the oscillator strength of the 710 cm^{-1} and 1380 cm^{-1} peaks dominate the ROA spectra of MOM-BINOL, the latter of which belongs to the naphthalene ring stretching mode.[15]

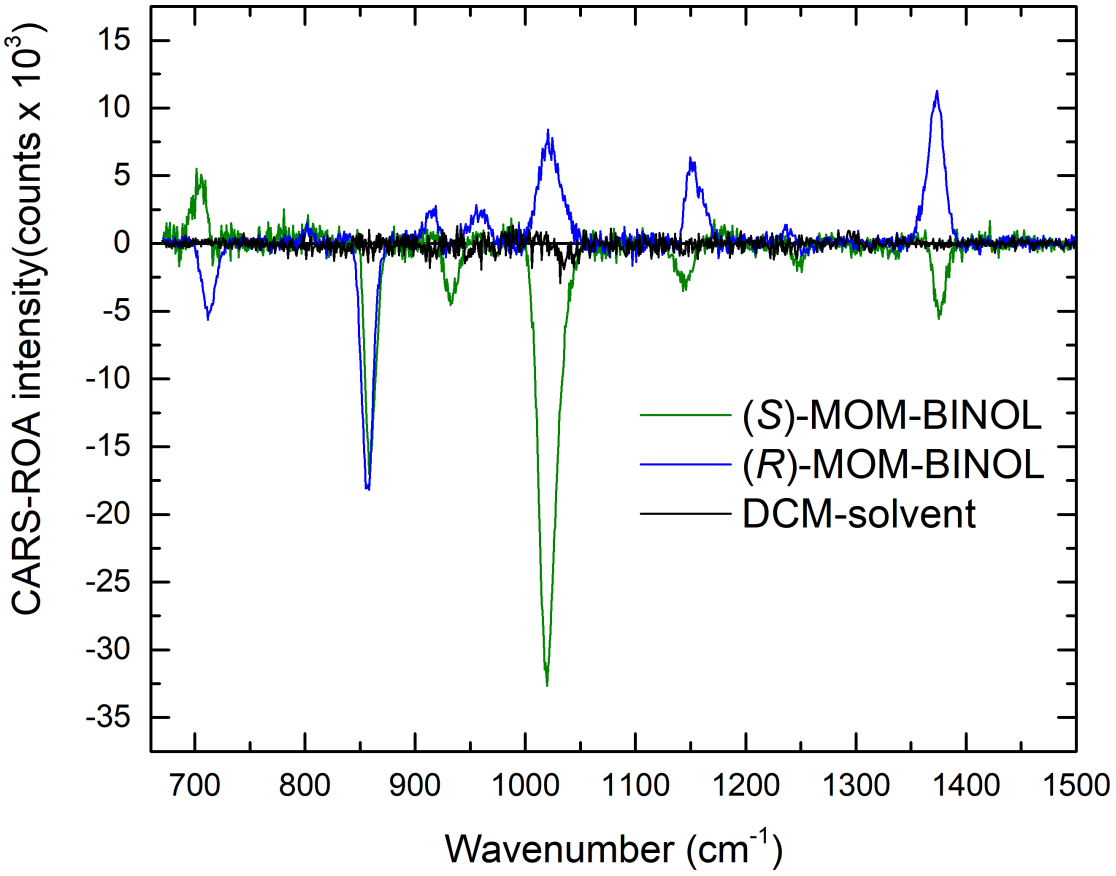

Figure 3.38: CARS-ROA spectra of MOM-BINOL in DCM (2 M, total acquisition time 100 s and $\theta_1 = \pm 0.65°$, cuvette thickness 1 mm). The observed Raman peak positions are approximately 710 cm^{-1}, 1020 cm^{-1}, 1150 cm^{-1}, 1240 cm^{-1}.

Subsequently, the (*R*)-MOM-BINOL measurements were reiterated at lower concentrations, namely 1 M, 0.5 M, and 0.25 M in DCM, aiming to assess whether the CARS-ROA spectrum undergoes notable distortion as observed in the diluted spectra of (-)-β-pinene (see left side of Fig. 3.40). For these concentrations, it can be observed that the spectra for 1 M and 0.5 M are mostly comparable to the previous measurement carried out at 2 M. The reason behind the peak at approximately 1150 cm^{-1} in the 1 M spectrum, showing a sign reversal, is probably the same as that observed at 860 cm^{-1} for the 2 M measurement, given that this signal shows the expected sign for the concentrations of 1 M and 0.5 M. These Raman peak-specific sign reversals demonstrate the sensitivity of the CARS-ROA technique, a phenomenon also observed in the pinene measurements. Moreover, the 1 M measurement displays an unusually dispersed lineshape on the lower wavenumber side of the peak.

On the right side of Fig. 3.40, the Raman peaks were integrated, and each value was normalized by the maximum value at 1 M. Here the origin serves as a predetermined data point, as there must be no signal at zero concentration. The dashed line represents the expected signal if the CARS-ROA concentration dependence was linear; most integrated signals, in particular for 0.25 M, fall near this line. However, it can be seen that the decrease in magnitude with concentration is not uniform across all peaks. Due to this high variation a slightly nonlinear dependence of the CARS-ROA signal with concentration cannot be ruled out. A nonlinearity in CARS-ROA is expected from the N^2 dependence of the achiral CARS local oscillator from the chiral compound to which the CARS-ROA signal is linear. The measurements could indicate that the loss of the CARS LO field may be partially counterbalanced by an additional local oscillator ($\sim N^2\chi_{1111}$) from the increased solvent. Additional measurements are warranted due to the significant signal fluctuations observed as well as the use of only three concentrations in the dilution series.

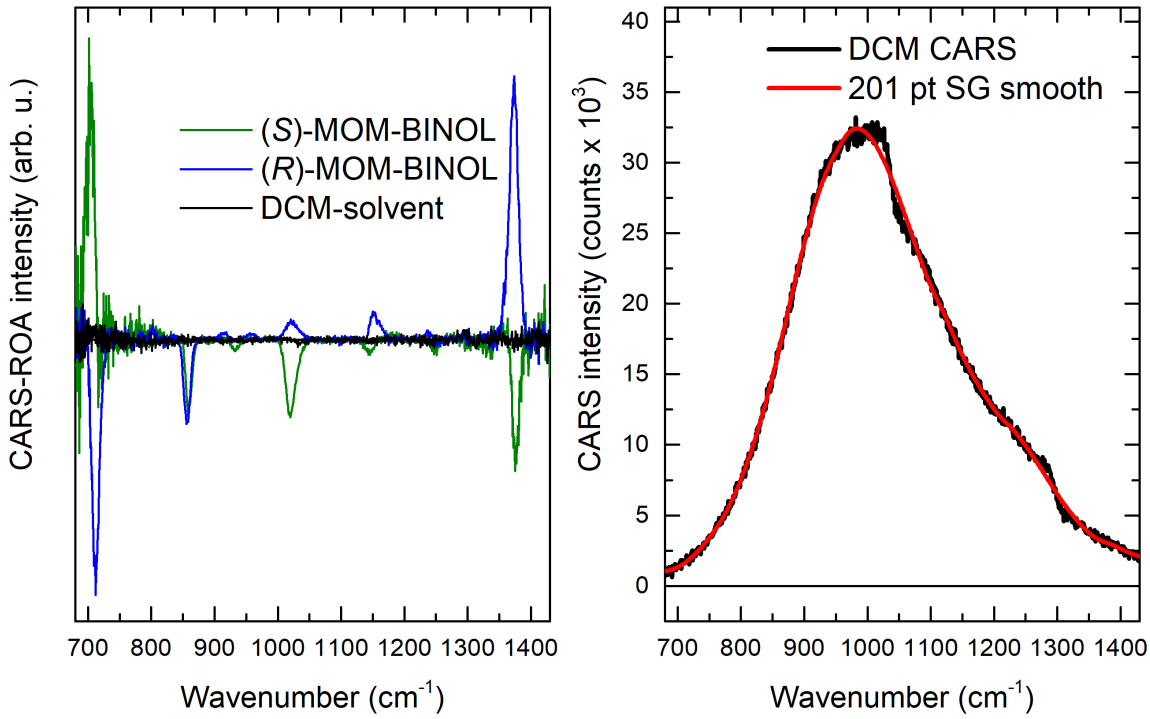

Figure 3.39: CARS-ROA spectra of MOM-BINOL in DCM (2 M, total acquisition time 100 s and $\theta_1 = \pm 0.6°$, cuvette thickness 1 mm)

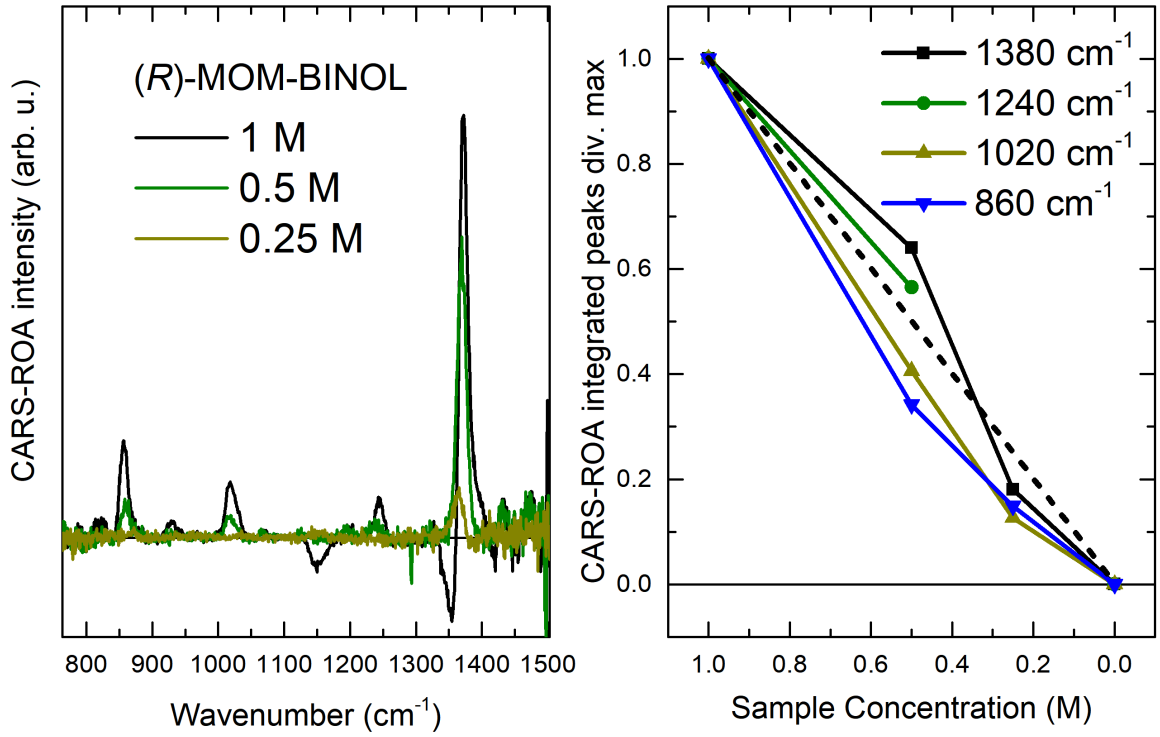

Figure 3.40: Left graph: CARS-ROA spectra of (*R*)-MOM-BINOL (background subtracted and divided by DCM reference) in DCM measured at three reduced concentrations of 1 M, 0.5 M, and 0.25 M (total acquisition time 400 s and $\theta_1 \approx \pm 0.6°$, cuvette thickness 1 mm). Right graph: Integrated peaks from spectra vs. chiral sample concentration. The dotted line represents a linear signal dependency.

3.3.3 Conclusion Heterodyne-CARS-ROA

The replication of CARS-ROA spectra for enantiomers of a chiral liquid (β-pinene) demonstrates the feasibility of measuring CARS-ROA using femtosecond Stokes pulses. While white light excels in capturing a much larger wavenumber range in a single measurement, a NOPA-based setup can be straightforwardly extended into the UV range by frequency doubling. UV-CARS-ROA has the potential for a much better contrast ratio between chiral and achiral signals due to the ω^5 dependence of the chiral signal compared to the ω^4 dependence of achiral CARS. At higher frequencies most molecules become chromophores and therefore, the resonance effect may further improve this contrast ratio.

It is not known to what extent ECD would contribute to a hypothetical CARS-RROA signal as this effect is a major concern for the interpretation of spontaneous RROA spectra.[114, 115] The resonance enhancement could further improve the detection of small concentrations in samples. Another goal, initially mentioned by Hamaguchi *et al.*, is time-resolved CARS-ROA in a pump-probe scheme, which currently seems unlikely due to the low concentration of excited molecules, and an already low signal-to-noise ratio for ground state measurements, without significant signal enhancement from the resonance effect.

Regrettably, the experimental realization of resonance CARS-ROA will likely prove challenging. This is due to the substantial increase in ORD near resonances. It has already been observed that ORD significantly impacts the measurements of nonresonant CARS-ROA, making it likely that an even greater impact would be seen in resonance CARS-ROA. Theoretical exploration of resonance CARS-ROA can also be anticipated to be challenging, given its a nonlinear effect that involves higher multipole moments.

Heterodyne CARS-ROA was furthermore found to be a very sensitive experiment. For many spectra, peculiar behaviors were observed, where the signal could reverse its sign for only a single Raman peak. One possible explanation for this wavelength-specific behavior is that the collinear CARS beam is composed of rings with progressively higher wavenumbers. As a result, each photon assigned to a specific wavenumber travels a distinct trajectory towards the spectrometer. Consequently, the measurement may be especially sensitive to any dust accumulated on the optics along the collection path. In addition to keeping optics clean, another precaution is to minimize the distance between the analyzer and the spectrometer.

However, based on experience, the cuvette glass wall surfaces are the most likely suspect to have a significant impact on the spectra, possibly by inducing additional birefringence which might permit the transmission of achiral signals.

Regarding dilution, the measurements of diluted pinene showed that solvent peaks can potentially show up in the CARS-ROA spectrum; this could be caused by a pre-resonance chiral transfer effect between solvent and solute.[114] Further measurements are required to validate this observation, as potential issues with the sample cell mentioned earlier may have affected the results. Conversely, the measurements of MOM-BINOL suggest that diluted samples can be measured in heterodyne CARS-ROA without significant change to line shape. The dilution measurements suggest a possibly linear instead of nonlinear dependence of concentration on the signal as would typically be expected from a CARS signal. This could be because the additional local oscillator (LO) from the solvent compensates for the loss of the chiral CARS-generated LO in diluted samples. Such a linear relationship in concentration is highly important for applications because it also enables measurements at low concentrations.

One seemingly insurmountable downside for CARS-ROA lies in its proportionality to the forward scattering CID of spontaneous ROA.[17] An important development for ROA spectrometers was the transition away from right-angle or forward scattering towards backward-scattering collection, primarily due to its inherently ca. 8-fold larger ROA intensity.[116] Backward scattering ROA is especially superior to forward scattering if the molecule consists predominantly of axially symmetric bonds. In such instances, the forward scattering CID can be entirely absent.

CARS-ROA on the other hand still presents multiple potential advantages with further development. For instance, CARS-ROA requires only linearly polarized light, yields higher signals, is fluorescence-free and can capture the complete chiral field due to the coherent beam carrying the signal.

Chapter 4

Outlook

Modern pulsed laser systems present many interesting opportunities for exploring the interplay between vibrational and electronic states. The three experimental techniques utilized in this thesis – transient absorption, resonance Raman, and chiral nonlinear Raman – can each offer interesting insights in this regard.

In the case of the transient absorption study of AAP ultrafast dynamics, the impact of vibrations on the relaxation dynamics was expected to have lesser importance, in particular at the onset of photoisomerization reactions. However, for non-rigid molecules, vibrations, such as the ground state vibrations of the arylazopyrazole phenyl ring, can still exert significant influence on electronic forces, which can make itself apparent in its ultrafast dynamics. It could therefore prove interesting to observe how the ultrafast dynamics of arylazopyrazole photoswitches change with decreasing temperature.

Resonance Raman spectroscopy with variable laser excitation wavelengths enables the measurement of Raman excitation profiles, which are sensitive to vibronic interactions, thereby potentially providing greater insights into molecular electronic states compared to conventional absorption spectroscopy. Unfortunately, fluorescence interference often complicates the measurement of Raman excitation profiles. To mitigate this, a Kerr gate can be employed. Yet, even with this method, this study of anthracene necessitated a unique approach: extracting the Raman signal by contrasting it with a fluorescence signal that does not contain the Raman signal. In many cases, such an approach might be deemed excessively time-consuming or result in a signal-to-noise ratio that is too low. Therefore, spontaneous anti-Stokes Raman scattering or CARS could emerge as more viable options for acquiring Raman excitation profiles on the lowest excited state, especially in situations where gated fluorescence is overwhelming, as evidenced in this instance. Alternatively, employing shorter Raman excitation pulses in tandem with a Kerr gate medium which has a faster nuclear response than benzene could mitigate Kerr-

gated fluorescence.

Understanding vibrational coupling interactions may hold particular future significance in the domain of Raman optical activity where the resonance Raman effect can enhance the typically faint chiral signal. However, employing a Kerr gate for fluorescence suppression in spontaneous ROA, as exemplified with anthracene, would probably be impossible due to the necessity of detecting circularly polarized light. Therefore, CARS-ROA, inherently devoid of fluorescence, presents an appealing alternative to leverage the resonance effect in ROA.

Bibliography

[1] Reichenauer, T.; Böckmann, M.; Ziegler, K.; Kumar, V.; Ravoo, B. J.; Dolsinis, N.; Schlücker, S. *Phys. Chem. Chem. Phys.* **2024**, *26*, 10832–10840.

[2] Hofmann, K. P.; Lamb, T. D. *Prog. Retin. Eye Res.* **2023**, *93*, 101116.

[3] Hüll, K.; Morstein, J.; Trauner, D. *Chem. Rev.* **2018**, *118*, 10710–10747.

[4] Weston, C. E.; Richardson, R. D.; Haycock, P. R.; White, A. J. P.; Fuchter, M. J. *J. Am. Chem. Soc.* **2014**, *136*, 11878–11881.

[5] Stricker, L.; Fritz, E.-C.; Peterlechner, M.; Doltsinis, N. L.; Ravoo, B. J. *J. Am. Chem. Soc.* **2016**, *138*, 4547–4554.

[6] Stricker, L.; Böckmann, M.; Kirse, T. M.; Doltsinis, N. L.; Ravoo, B. J. *Chem. Eur. J.* **2018**, *24*, 8639–8647.

[7] Siewertsen, R.; Neumann, H.; Buchheim-Stehn, B.; Herges, R.; Näther, C.; Renth, F.; Temps, F. *J. Am. Chem. Soc.* **2009**, *131*, 15594–15595.

[8] Emmerling, F.; Lettenberger, M.; Laubereau, A. *J. Phys. Chem.* **1996**, *100*, 19251–19256.

[9] Platt, J. R. *J. Chem. Phys.* **1949**, *17*, 484–495.

[10] Blackmond, D. G. *Cold Spring Harb. perspect. biol.* **2010**, *2*, a002147.

[11] Meyer-Ilse, J.; Akimov, D.; Dietzek, B. *Laser Photonics Rev.* **2013**, *7*, 495–505.

[12] Schalley, C. A. *Analytical methods in supramolecular chemistry*; Wiley-VCH: Weinheim, 2007.

[13] Barron, L. D.; Hecht, L.; McColl, I. H.; Blanch, E. W. *Mol. Phys.* **2004**, *102*, 731–744.

[14] Kumar, V.; Schlücker, S. *Molecular and Laser Spectroscopy*; Elsevier, 2022; pp 101–139.

[15] Kumar, V.; Reichenauer, T.; Supovec, L.; Jansen, D.; Brodt, N.; Zając, G.; Domagała, A.; Barańska, M.; Niemeyer, J.; Schlücker, S. *J. Raman Spectrosc.* **2023**, *54*, 1011–1020.

[16] Bjarnason, J. Ö.; Andersen, H. C.; Hudson, B. S. *J. Chem. Phys.* **1980**, *72*, 4132–4140.

[17] Oudar, J.-L.; Minot, C.; Garetz, B. A. *J. Chem. Phys.* **1982**, *76*, 2227–2237.

[18] Knowles, K. E.; Koch, M. D.; Shelton, J. L. *J. Mater. Chem. C* **2018**, *6*, 11853–11867.

[19] Schmitt, M.; Dietzek, B.; Hermann, G.; Popp, J. *Laser Photonics Rev.* **2007**, *1*, 57–78.

[20] Mukamel, S. *Principles of Nonlinear Optical Spectroscopy*; Oxford series in optical and imaging sciences; Oxford University Press: New York, 1995; Vol. 6.

[21] Mančal, T. *Non-linear Optical Spectroscopy: Lecture 7: Pump-probe spectroscopy (part 1), www.mancal.cz/teaching/non-linear-optical-spectroscopy-videos*, 30.03. 2022.

[22] Szymański, W.; Beierle, J. M.; Kistemaker, H. A. V.; Velema, W. A.; Feringa, B. L. *Chem. Rev.* **2013**, *113*, 6114–6178.

[23] S. W. Hell *Far-field optical nanoscopy*; Single Molecule Spectroscopy in Chemistry, Physics and Biology; Springer Berlin Heidelberg, 2010.

[24] Levine, B. G.; Martínez, T. J. *Annu. Rev. Phys. Chem.* **2007**, *58*, 613–634.

[25] Devaquet, A. *Pure Appl. Chem.* **1975**, *41*, 455–473.

[26] Baroncini, M.; Groppi, J.; Corra, S.; Silvi, S.; Credi, A. *Adv. Opt. Mater.* **2019**, *7*, 1900392–1900408.

[27] Lednev, I. K.; Ye, T.-Q.; Hester, R. E.; Moore, J. N. *J. Phys. Chem.* **1996**, *100*, 13338–13341.

[28] Maurer, R. J.; Reuter, K. *J. Chem. Phys.* **2011**, *135*, 224303–224313.

[29] Stranius, K.; Börjesson, K. *Sci. Rep.* **2017**, *7*, 41145–41152.

[30] Beharry, A. A. Characterization of Azobenzene-based Photo-switches and their Evaluation for in vivo Applications. Dissertation, University of Toronto, Canada, 2012.

[31] Siewertsen, R.; Schönborn, J. B.; Hartke, B.; Renth, F.; Temps, F. *Phys. Chem. Chem. Phys.* **2011**, *13*, 1054–1063.

[32] Nägele, T.; Hoche, R.; Zinth, W.; Wachtveitl, J. *Chem. Phys. Lett.* **1997**, *272*, 489–495.

[33] Bahrenburg, J.; Röttger, K.; Siewertsen, R.; Renth, F.; Temps, F. *Photochem. Photobiol. Sci.* **2012**, *11*, 1210–1219.

[34] Gerkman, M. A.; Gibson, R. S. L.; Calbo, J.; Shi, Y.; Fuchter, M. J.; Han, G. G. D. *J. Am. Chem. Soc.* **2020**, *142*, 8688–8695.

[35] Ghebreyessus, K.; Uba, I.; Geddis, D.; Hömmerich, U. *J. Solid State Chem.* **2021**, *303*, 122519.

[36] Hanopolskyi, A. I.; De, S.; Białek, M. J.; Diskin-Posner, Y.; Avram, L.; Feller, M.; Klajn, R. *Beilstein J. Org. Chem.* **2019**, *15*, 2398–2407.

[37] Morikawa, M.-a.; Mizuno, M.; Harada, N.; Kimizuka, N. *Chem. Lett.* **2023**, *52*, 727–731.

[38] Simke, J.; Bösking, T.; Ravoo, B. J. *Org. Lett.* **2021**, *23*, 7635–7639.

[39] Ludwanowski, S.; Ari, M.; Parison, K.; Kalthoum, S.; Straub, P.; Pompe, N.; Weber, S.; Walter, M.; Walther, A. *Chem. Eur. J.* **2020**, *26*, 13203–13212.

[40] Wang, Y.-T.; Liu, X.-Y.; Cui, G.; Fang, W.-H.; Thiel, W. *Angew. Chem.* **2016**, *128*, 14215–14219.

[41] Böckmann, M.; Doltsinis, N. L.; Marx, D. *Angew. Chem.* **2010**, *122*, 3454–3456.

[42] Böckmann, M.; Doltsinis, N. L.; Marx, D. *J. Chem. Phys.* **2012**, *137*, 22A505.

[43] Keyes, T. E.; Forster, R. J. *Handbook of Electrochemistry*; Elsevier, 2007; pp 591–635.

[44] Oladepo, S. A.; Xiong, K.; Hong, Z.; Asher, S. A.; Handen, J.; Lednev, I. K. *Chem. Rev.* **2012**, *112*, 2604–2628.

[45] Albrecht, A. C. *J. Chem. Phys.* **1961**, *34*, 1476–1484.

[46] Asher, S. A.; Johnson, C. R. *Science* **1984**, *225*, 311–313.

[47] Kasha, M. *Discuss. Faraday Soc.* **1950**, *9*, 14.

[48] Holtum, T.; Reichenauer, T.; Kumar, V.; Schlücker, S. *J. Raman Spectrosc.* **2023**, *54*, 288–295.

[49] Wei, L.; Min, W. *J. Phys. Chem. Lett.* **2018**, *9*, 4294–4301.

[50] Placzek, G.; Lawrence Livermore Laboratory *The Rayleigh and Raman Scattering*; Translation series; Lawrence Radiation Laboratory, 1959.

[51] Czernuszewicz, R. S.; Zaczek, M. B. In *Encyclopedia of Inorganic and Bioinorganic Chemistry*; Scott, R. A., Ed.; Wiley, 2012.

[52] *The Raman Effect: A Unified Treatment of the Theory of Raman Scattering by Molecules*; Wiley, 2002.

[53] Clark, R. J. H.; Stewart, B. In *Inorganic Chemistry and Spectroscopy*; Dunitz, J. D., Goodenough, J. B., Hemmerich, P., Ibers, J. A., Jørgensen, C. K., Neilands, J. B., Reinen, D., Williams, R. J. P., Clark, H. J. H., Stewart, B., Simon, A., Daul, C., Schläpfer, C. W., von Zelewsky, A., Eds.; Structure and Bonding; Springer Berlin Heidelberg: Berlin, Heidelberg, 1979; Vol. 36; pp 1–80.

[54] Maker, P. D.; Terhune, R. W. *Phys. Rev.* **1965**, *137*, A801–A818.

[55] Hellwarth, R. W.; Owyoung, A.; George, N. *Phys. Rev. A* **1971**, *4*, 2342–2347.

[56] Harrison, N. J.; Jennings, B. R. *JPCRD* **1992**, *21*, 157–163.

[57] Roberto Righini *Science* **1993**, *262*, 1386–1390.

[58] Zhao, P.; Reichert, M.; Benis, S.; Hagan, D. J.; van Stryland, E. W. *Optica* **2018**, *5*, 583.

[59] Kedenburg, S.; Steinmann, A.; Hegenbarth, R.; Steinle, T.; Giessen, H. *Appl. Phys. B* **2014**, *117*, 803–816.

[60] Albrecht, H.-S.; Heist, P.; Kleinschmidt, J.; van Lap, D.; Schröder, T. *Appl. Phys. B* **1992**, *55*, 362–364.

[61] Blake, J. C.; Nieto-Pescador, J.; Li, Z.; Gundlach, L. *Opt. Lett.* **2016**, *41*, 2462–2465.

[62] P. Matousek, M. Towrie, A. Stanley, and A. W. Parker *Appl. Spectrosc.* **1999**, *53*, 1485–1489.

[63] Matousek, P.; Towrie, M.; Ma, C.; Kwok, W. M.; Phillips, D.; Toner, W. T.; Parker, A. W. *J. Raman Spectrosc.* **2001**, *32*, 983–988.

[64] Matousek, P.; Towrie, M.; Parker, A. W. *J. Raman Spectrosc.* **2002**, *33*, 238–242.

[65] Everall, N.; Hahn, T.; Matousek, P.; Parker, A. W.; Towrie, M. *Appl. Spectrosc.* **2001**, *55*, 1701–1708.

[66] Friedrich, D. M.; Mathies, R.; Albrecht, A. C. *J. Mol. Spectrosc.* **1974**, *51*, 166–188.

[67] Ohta, N.; Ito, M. *Chem. Phys.* **1977**, *20*, 71–81.

[68] Marconi, G.; Salvi, P. R. *J. Phys. Colloques* **1985**, *46*, C7–441–C7–445.

[69] Holtum, T.; Bloino, J.; Pappas, C.; Kumar, V.; Barone, V.; Schlücker, S. *J. Raman Spectrosc.* **2021**, *52*, 2292–2300.

[70] Benkyi, I.; Tapavicza, E.; Fliegl, H.; Sundholm, D. *Phys. Chem. Chem. Phys.* **2019**, *21*, 21094–21103.

[71] Ramaley, L.; Campbell, J. L. *Instrum Sci. Technol.* **2000**, *28*, 189–204.

[72] Xie, H.; He, M.-j.; Deng, X.-Y.; Du, L.; Fan, C.-J.; Yang, K.-K.; Wang, Y.-Z. *ACS Appl. Mater. Interfaces.* **2016**, *8*, 9431–9439.

[73] Breton, G. W.; Vang, X. *J. Chem. Educ.* **1998**, *75*, 81.

[74] Kristinaityte, K.; Urbańczyk, M.; Mames, A.; Pietrzak, M.; Ratajczyk, T. *Molecules* **2021**, *26*.

[75] Boyd, R. W. *Nonlinear optics*, fourth edition ed.; Academic Press an imprint of Elsevier: London United Kingdom and San Diego CA, 2020.

[76] Patel, I. I.; Steuwe, C.; Reichelt, S.; Mahajan, S. *J. Opt.* **2013**, *15*, 094006.

[77] Müller, M.; Zumbusch, A. *Chemphyschem* **2007**, *8*, 2156–2170.

[78] Bjorklund, G. *IEEE J. Quantum Electron.* **1975**, *11*, 287–296.

[79] Papac, M. J.; Posner, J. D.; Dunn-Rankin, D. *Appl. Spectrosc.* **2003**, *57*, 93–99.

[80] Hiramatsu, K.; Okuno, M.; Kano, H.; Leproux, P.; Couderc, V.; Hamaguchi, H.-o. *Phys. Rev. Lett.* **2012**, *109*, 083901.

[81] Hiramatsu, K.; Leproux, P.; Couderc, V.; Nagata, T.; Kano, H. *Opt. Lett.* **2015**, *40*, 4170–4173.

[82] Manzoni, C.; Cerullo, G. *J. Opt.* **2016**, *18*, 103501.

[83] Mao, P.; Wang, Z.; Dang, W.; Weng, Y. *Rev. Sci. Instrum.* **2015**, *86*, 123113.

[84] Seitz, P.; Theuwissen, A. J. P. *Single-Photon Imaging*; Springer Berlin Heidelberg: Berlin, Heidelberg, 2011; Vol. 160.

[85] Kanal, F.; Keiber, S.; Eck, R.; Brixner, T. *Opt. Express* **2014**, *22*, 16965–16975.

[86] Wu, T. R.; Shen, L.; Chong, J. M. *Org. Lett.* **2004**, *6*, 2701–2704.

[87] Kumar, V.; Holtum, T.; Sebena, D.; Giese, M.; Voskuhl, J.; Schlücker, S. *Spectrochimica acta. Part A, Molecular and biomolecular spectroscopy* **2021**, *250*, 1386–1425.

[88] Satzger, H.; Root, C.; Braun, M. *J. Phys. Chem. A* **2004**, *108*, 6265–6271.

[89] Quick, M.; Dobryakov, A. L.; Gerecke, M.; Richter, C.; Berndt, F.; Ioffe, I. N.; Granovsky, A. A.; Mahrwald, R.; Ernsting, N. P.; Kovalenko, S. A. *J. Phys. Chem. B* **2014**, *118*, 8756–8771.

[90] Satzger, H.; Spörlein, S.; Root, C.; Wachtveitl, J.; Zinth, W.; Gilch, P. *Chem. Phys. Lett.* **2003**, *372*, 216–223.

[91] Fujino Tatsuya, Arzhantsev Sergei Yu., and Tahara Tahei *BCSJ* **2002**, 1031–1040.

[92] Hoffman, D. P.; Mathies, R. A. *Phys. Chem. Chem. Phys.* **2012**, *14*, 6298–6306.

[93] Wang, L.; Xu, W.; Yi, C.; Wang, X. *J. Mol. Graph. Model.* **2009**, *27*, 792–796.

[94] Otolski, C. J.; Raj, A. M.; Ramamurthy, V.; Elles, C. G. *Chem. Sci.* **2020**, *11*, 9513–9523.

[95] Krawczyk, K. M.; Field, R. L.; Liu, L. C.; Dong, M.; Woolley, G. A.; Miller, R. D. *Can. J. Chem.* **2019**, *97*, 488–495.

[96] Ekvall, K.; van der Meulen, P.; Dhollande, C.; Berg, L.-E.; Pommeret, S.; Naskrecki, R.; Mialocq, J.-C. *J. Appl. Phys.* **2000**, *87*, 2340–2352.

[97] Slavov, C.; Yang, C.; Heindl, A. H.; Wegner, H. A.; Dreuw, A.; Wachtveitl, J. *Angew. Chem. Int. Ed. Engl.* **2020**, *59*, 380–387.

[98] Lacombe, L.; Maitra, N. T. *Npj Comput. Mater.* **2023**, *9*.

[99] Doltsinis, N. L.; Marx, D. *Phys. Rev. Lett.* **2002**, *88*, 166402–1–166402–4.

[100] Appavoo, K.; Sfeir, M. Y. *Rev. Sci. Instrum.* **2014**, *85*, 055114.

[101] Yu, Z.; Gundlach, L.; Piotrowiak, P. *Opt. Lett.* **2011**, *36*, 2904–2906.

[102] Efremov, E. V.; Ariese, F.; Mank, A. J. G.; Gooijer, C. *Anal. Chem.* **2006**, *78*, 3152–3157.

[103] Blatt, E.; Treloar, F. E.; Ghiggino, K. P.; Gilbert, R. G. *J. Phys. Chem.* **1981**, *85*, 2810–2816.

[104] Laptenok, S. P.; Nuernberger, P.; Lukacs, A.; Vos, M. H. *Methods Mol. Biol.* **2014**, *1076*, 321–336.

[105] Kastrati, A.; Oswald, F.; Scalabre, A.; Fromm, K. M. *Photochem* **2023**, *3*, 227–273.

[106] Lorenzo, C. F.; Alcántara, R.; Martin, J. *J. Raman Spectrosc.* **1989**, *20*, 291–296.

[107] Tuschel, D. *Spectroscopy* **2014**, *29*, 14.

[108] Strommen, D. P. *J. Chem. Educ.* **1992**, *69*, 803–807.

[109] Mattiat, J.; Luber, S. *J. Chem. Phys.* **2018**, *149*, 174108.

[110] Zilberg, S.; Samuni, U.; Fraenkel, R.; Haas, Y. *Chem. Phys.* **1994**, *186*, 303–316.

[111] Amirav, A.; Horwitz, C.; Jortner, J. *J. Chem. Phys.* **1988**, *88*, 3092–3110.

[112] Chen, W.-C.; Cheng, Y.-C. *J. Phys. Chem. A* **2020**, *124*, 7644–7657.

[113] Berova, N. *Comprehensive chiroptical spectroscopy*; Wiley: Hoboken NJ, 2012.

[114] Machalska, E.; Zajac, G.; Baranska, M.; Kaczorek, D.; Kawęcki, R.; Lipiński, P. F. J.; Rode, J. E.; Dobrowolski, J. C. *Chem. Sci.* **2020**, *12*, 911–916.

[115] Yang, Q.; Bloino, J.; Šestáková, H.; Šebestík, J.; Kessler, J.; Hudecová, J.; Kapitán, J.; Bouř, P. *Angew. Chem., Int. Ed.* **2023**, *62*, e202312521.

[116] Hecht, L.; Barron, L. D.; Hug, W. *Chem. Phys. Lett.* **1989**, *158*, 341–344.

Acknowledgments

Firstly, I would like to express my sincere appreciation to Professor Sebastian Schlücker for accepting me as a doctoral student and for his guidance across various subjects. I also want to extend my gratitude to Dr. Vikas Kumar for introducing me to nonlinear optics, providing moral support, as well as engaging in enjoyable discussions.

Furthermore, I am grateful to the DFG-funded CRC 1242 for funding my PhD research and providing me with the opportunity to delve into this fascinating field. A special acknowledgment goes to Marcus Böckmann from the Doltsinis group for his invaluable assistance, particularly in elucidating the complexities of arylazopyrazole photoswitches and for his pivotal role in facilitating our publication.

Additionally, I wish to express my appreciation for the great support received from Katharina Ziegler of the Ravoo group, and to Professor Bart Jan Ravoo for enabling our collaboration. Lastly, I am thankful for the enriching experiences shared with all members of the research group.